LAKEHEAD UNIVERSITY

A Tunable Multi-Stable Piezoelectric Vibration Energy Harvester

By

Haining Li

A THESIS

SUBMITTED TO THE FACULTY OF GRADUATE STUDIES

IN PARTIAL FULFILLMENT OF THE REQUIREMENT FOR THE

DEGREE OF MASTER OF SCIENCE

IN

MECHANICAL ENGINEERING

Thunder Bay, Ontario, Canada

January 2021

ABSTRACT

The vibration energy harvester is intended to convert ambient environmental energy into electrical energy. It has great potential to be an alternative to the conventional battery in low-power electric devices. A traditional vibrating energy harvester consists of a linear oscillator that operates in a narrow frequency band. Nonlinear energy harvesters provide a promising solution to widen the operating bandwidth. Based on the system stability states, the nonlinear vibration energy harvesters can be classified as mono-stable and multi-stable. In this study, a tunable multi-stable piezoelectric energy harvester is proposed. The apparatus can be manually tuned to achieve three states, namely tri-stable, bi-stable, and mono-stable. It has a compact structure compared to the existing designs.

Firstly, the apparatus's design is presented. The analytical model for the restoring force due to the magnetic interaction is developed by using the magnetic dipole approach. Then the model is validated experimentally. Using the measured data, the model optimization is conducted by applying the genetic algorithm. Based on the optimized model, the stability state regions verse the tuning parameters are identified. Secondly, the electromechanical model of the developed apparatus is developed. By linearizing the model, the optimum resistance value of the linear system under harmonic excitation and corlored noise excitation is studied, respectively. Thirdly, the output performance of the bi-stable energy harvester under colored noise excitation is investigated numerically and experimentally. Fourthly, the output performance of the tri-stable energy harvester is studied numerically and experimentally as well. The results show that the frequency analysis method is insufficient to determine the optimum resistance when the tri-stable energy harvester is engaged in the high orbit inter-well oscillation. In addition, when the multi-stable energy harvester system is at resonance, the output performance will be largely improved by the separation between each well.

ACKNOWLEDGMENT

First and foremost, my deepest gratitude would go to my supervisor, Dr. Kefu Liu, who led me into this magnificent engineering world. Thanks to his constant help and gives me the courage to get through all the challenges I met in research and life. For the last year, He walked me through all the stages of the writing of this thesis. Without his patient and illuminating instruction, this thesis could not have reached its present form.

Secondly, I would like to express my gratitude to the people I work with. Youzuo Jin who taught me so many things in coding and experimenting. Zihao Chen who always gives me a hint when my research is stagnating. And Yan Wang who helps me to improve my English skill.

Finally, I would like to thank my parents for their selfless love and great confidence in me all through these years. And I am greatly indebted to Ms. Ning Jiang, a very kind and wise woman who gives me a lot of help and advice. I also owe my sincere gratitude to my life partner Zhenxuan Jia who gave me her consideration and helping me work out my problems during a difficult time.

Table of Contents

ABSTRACT.....i
ACKNOWLEDGMENT.....ii
Table of Contents iii
List of Figures.....vi
List of Tables..... xiii
List of Acronyms.....xiv
Chapter 1 Introduction 1
1.1 Motivation of the Research 1
1.2 Literature Review.....2
1.2.1 Vibration Energy Harvesters 2
1.2.2 Cantilevered Piezoelectric Energy Harvester 4
1.2.3 Modelling Methods of the Cantilevered Piezoelectric Energy Harvester ...7
1.3 Research Objectives.....7
1.4 Thesis Outline 8
Chapter 2 Apparatus and Modeling 9
2.1 Configuration of the Apparatus.....9
2.2 Validation of the Model for the Restoring Force 16
2.2.1 Identification of the Restoring Force of the Beam. 16
2.2.2 The Total Restoring Force Surfaces 18
2.2.3 Comparison of the Results.....22
2.3 Optimization of the Dipole Model.....25
2.3.1 Genetic Algorithm 25
2.3.2 Implementation and Results 27
2.4 Stability State Region 31
2.5 Conclusions.....34
Chapter 3 Piezoelectric Vibration Energy Harvester Model.....35
3.1 The Piezoelectric Phenomenon.....35

3.2 Modeling of the Cantilevered Piezoelectric Energy Harvester 40
3.3 Identification of the System Parameters of the LEH 42
3.3.1 Damping Coefficient Identification 42
3.3.2 Identification of the Electromechanical Coefficient 44
3.4 Experimental Validation 46
3.5 Optimum Resistance for the LEH 48
3.5.1 Optimum Resistance of the LEH under Harmonic Excitation 48
3.5.2 Optimum Resistance of LEH under the Colored Noise Excitation. 53
3.6 Conclusions 56
Chapter 4 Bi-stable Energy Harvesters under the Colored Noise Excitation 58
4.1 Optimum Resistance of BEHs under the Colored Noise Excitation 59
4.1.1 Numerical Simulations of the BEHs with an Open-Circuit 59
4.1.2 Numerical Simulations of BEHs with a Closed-Circuit 67
4.1.3 Experimental Validation 71
4.1.4 Discussion of the Results 75
4.2 The Output Power verse the Excitation Level of BEHs 78
4.2.1 Numerical Simulation 79
4.2.2 Experimental Validation 82
4.3 Conclusions 84
Chapter 5 Tri-stable Energy Harvesters under the Colored Noise Excitation 85
5.1 Optimum Resistance of the TEHs under the Colored Noise Excitation 87
5.1.1 Numerical Simulation of TEHs with an Open-Circuit 87
5.1.2 Numerical Simulation of TEHs with a Closed-Circuit 95
5.1.3 Experimental Validation 99
5.1.4 Discussion of the Results 102
5.2 The Output Power verse the Excitation Level of the TEHs 105
5.2.1 Numerical Simulation 105
5.2.2 Experimental Validation 108
5.3 Conclusions 110
Chapter 6 Conclusions 112

Reference 115

List of Figures

Figure 1.1 Schemes of three vibration energy harvesters (a) electromagnetic energy harvester; (b) electrostatic energy harvester [21]; (c) piezoelectric energy harvester..4
Figure 1.2 Schematic of a tunable mono-stable cantilevered piezoelectric energy harvester [46]. 5
Figure 1.3 Schematic of multi-stable cantilevered piezoelectric energy harvesters (a) bi-stable configuration; (b) tri-stable configuration [54]. 6
Figure 2.1 Schematic of the tunable multi-stable piezoelectric energy harvester. 9
Figure 2.2 Illustration of the spatial positions and polarities of the magnets..... 11
Figure 2.3 Front view of the apparatus. 12
Figure 2.4 Top view of the apparatus. 12
Figure 2.5 Experimental setup for measuring the restoring force of the cantilever beam: (a) schematic of the setup; (b) photo of the setup. 17
Figure 2.6 The measured restoring force of the cantilever beam. 17
Figure 2.7 (a) Photo of the experimental setup, (b) Schematic of the model for the experimental setup.....19
Figure2.8 Restoring force surface for the apparatus of case (I). 20
Figure 2.9 Restoring force surface for the apparatus of case (II). 21
Figure 2.10 Restoring force surface for the apparatus of case (III). 21
Figure 2.11 Restoring force surface for the apparatus of case (IV). 22
Figure 2.12 Comparison of the experimental results (red circle) and the analytical results (blue solid line) for the total restoring forces: (a) case (I); (b) case (II); (c) case (III); (d) case (IV). 24
Figure 2.13 Flowchart of the genetic algorithm optimization.....27
Figure 2.14 fitness value of each generation, blue circles, are the best fitness values and the black circles are the mean fitness values. 29
Figure 2.15 The optimized analytical results of the restoring force verse the transverse displacement for four different tuning distances, red circle for the measured data and blue

solid line for the calculated result: (a) case (I); (b) case (II); (c) case (III); (d) case (IV). 30
Figure 2.16 Potential energies of the four cases. 31
Figure 2.17 Stability state region. 32
Figure 2.18 Potential energies of three different strengths: the strong, medium and weak tri-stable states. 33
Figure 2.19 Potential energies of three different strengths: the strong, medium and weak bi-stable states. 33
Figure 2.20 Potential energies of three different strengths: the strong, medium and weak mono-stable states. 34
Figure 3.1 The cubic (outside) and tetragonal (inside) structures of the lead zirconate titanate (PZT) crystal. 36
Figure 3.2 (a) The domains of PZT material before polarization; (b) The domains of PZT material after polarization. 37
Figure 3.3 Electric fields caused by different types of physical deformation: (a) unloaded; (b) loaded by tension force; (c) loaded by compressive force. 38
Figure 3.4 Three axes of a rectangular piezoceramic bulk. 38
Figure 3.5 Piezoelectric energy harvester operates in the $d31$ mode: (a) upward bending situation; (b) unloaded situation; (c) downward bending situation. 40
Figure 3.6 1-D model of the uni-morph cantilevered piezoelectric energy harvester.40
Figure 3.7 Free response of the LEH (blue line). And the peak values of the free-response (red circle). 43
Figure 3.8 Piezoelectric energy harvester voltage output vs relative beam displacement. 45
Figure 3.9 Voltage responses of the LEH under the different harmonic excitations: simulation results (blue solid line); measured data (red circles). 47
Figure 3.10 Relationships between the output powers and load resistances under different frequency harmonic excitations: (a) under the excitation of 4 Hz; (b) under the excitation of 5 Hz; (c) under the excitation of 6 Hz. 51
Figure 3.11 The time response and power spectrum of the open-circuit voltage of LEH

under the colored noise excitation: (a) the low-level excitation; (b) the medium-level excitation; (c) the high-level excitation.....54
Figure 3.12 Simulation results of the relationship between the output power and load resistance of LEH under the colored noise excitation: (a) the low-level excitation; (b) the medium-level excitation; (c) the high-level excitation. 55
Figure 3.13 Experimental results of the relationship between the output power and the load resistance of LEH under the different random excitation levels: (a) the low-level excitation; (b) the medium-level excitation. 56
Figure 4.1 Potential energies of three bi-stable energy harvesters: strong (BEH1), medium (BEH2) and weak (BEH3). 59
Figure 4.2 Oscillation modes of BEH1 under the three levels of colored noise excitation: (a) intra-well oscillation; (b) weak inter-well oscillation; (c) strong inter-well oscillation. 61
Figure 4.3 The time response (upper plot) and phase portrait (lower plot) of BEH1 under the colored noise excitation: (a) the low-level excitation; (b) the medium-level excitation; (c) the high-level excitation.....62
Figure 4.4 The time response and power spectrum of the open-circuit voltage of BEH1 under the colored noise excitation: (a) the low-level excitation; (b) the medium-level excitation; (c) the high-level excitation.....63
Figure 4.5 The time response (upper plot) and phase portrait (lower plot) of BEH2 under the colored noise excitation: (a) the low-level excitation; (b) the medium-level excitation; (c) the high-level excitation.....64
Figure 4.6 The response and power spectrum of the open-circuit voltage of BEH2 under the colored noise excitation: (a) the low-level excitation; (b) the medium-level excitation; (c) the high-level excitation.....65
Figure 4.7 The time response (upper plot) and phase portrait (lower plot) of BEH3 under the colored noise excitation: (a) the low-level excitation; (b) the medium-level excitation; (c) the high-level excitation.....66
Figure 4.8 The response and power spectrum of the open-circuit voltage of BEH3 under the colored noise excitation: (a) the low-level excitation; (b) the medium-level excitation;

(c) the high-level excitation.....67
Figure 4.9 Simulation results of the relationship between the output power and load resistance of BEH1 under the colored noise excitation: (a) the low-level excitation; (b) the medium-level excitation; (c) the high-level excitation. 69
Figure 4.10 Simulation results of the relationship between the output power and load resistance of BEH2 under the colored noise excitation: (a) the low-level excitation; (b) the medium-level excitation; (c) the high-level excitation. 70
Figure 4.11 Simulation results of the relationship between the output power and load resistance of BEH3 under the colored noise excitation: (a) the low-level excitation; (b) the medium-level excitation; (c) the high-level excitation. 71
Figure 4.12 Experimental results of the relationship between the output power and the load resistance of BEH1 under the different random excitation levels: (a) the low-level excitation; (b) the medium-level excitation; (c) the high-level excitation. 72
Figure 4.13 Comparison of the simulation results and experimental results for BEH1 under the high-level excitation: (a) the voltage response; (b) the output power. 73
Figure 4.14 Experimental results of the relationship between the output power and the load resistance of BEH2 under the different random excitation levels: (a) the low-level excitation; (b) the medium-level excitation; (c) the high-level excitation. 74
Figure 4.15 Experimental results of the relationship between the output power and the load resistance of BEH3 under the different random excitation levels: (a) the low-level excitation; (b) the medium-level excitation; (c) the high-level excitation. 75
Figure 4.16 The simulation results of the three BEHs: (a) the voltage responses; (b) the output powers. 80
Figure 4.17 The simulation results of time response (upper plot) and phase portrait (lower plot) of BEH1 under the specific level of random excitation: (a) under the A1 excitation level; (b) under the A2 excitation level. 80
Figure 4.18 The simulation results of time response (upper plot) and phase portrait (lower plot) of BEH2 under the specific level of random excitation: (a) under the B1 excitation level; (b) under the B2 excitation level. 81
Figure 4.19 The simulation results of time response (upper plot) and phase portrait (lower

plot) of BEH3 under the specific level of random excitation: (a) under the C1 excitation level; (b) under the C2 excitation level. 81
Figure 4.20 The experimental results of the three bi-stable energy harvesting systems: (a) voltage responses; (b) power output. 82
Figure 4.21 The experimental results of time response (upper plot) and phase portrait (lower plot) of three systems under the specific level of random excitation: (a) BEH1 under the A excitation level; (b) BEH2 under the B excitation level; (c) BEH3 under the C excitation level. 83
Figure 5.1 Potential energy of the BEH (blue solid line) and the THE (black dash line). 86
Figure 5.2 Potential energies of three strengths of TEHs: strong (TEH1), medium (TEH2) and weak (TEH3). 87
Figure 5.3 Oscillation modes of TEH1 under the three excitation levels: (a) intra-well oscillation; (b) weak inter-well oscillation; (c) strong inter-well oscillation. 89
Figure 5.4 The time response (upper plot) and phase portrait (lower plot) of TEH1 under the colored noise excitation: (a) the low-level excitation; (b) the medium-level excitation; (c) the high-level excitation. 90
Figure 5.5 The time response and power spectrum of the open-circuit voltage of TEH1 under the colored noise excitation: (a) the low-level excitation; (b) the medium-level excitation; (c) the high-level excitation. 91
Figure 5.6 The time response (upper plot) and phase portrait (lower plot) of TEH2 under the colored noise excitation: (a) the low-level excitation; (b) the medium-level excitation; (c) the high-level excitation. 92
Figure 5.7 The time response and power spectrum of the open-circuit voltage of TEH2 under the colored noise excitation: (a) the low-level excitation; (b) the medium-level excitation; (c) the high-level excitation. 93
Figure 5.8 The time response (upper plot) and phase portrait (lower plot) of TEH3 under the colored noise excitation: (a) the low-level excitation; (b) the medium-level excitation; (c) the high-level excitation. 94
Figure 5.9 The time response and power spectrum of the open-circuit voltage of TEH3

under the colored noise excitation: (a) the low-level excitation; (b) the medium-level excitation; (c) the high-level excitation. 95
Figure 5.10 Simulation results of the relationship between the output power and load resistance of TEH1 under the colored noise excitation: (a) the low-level excitation; (b) the medium-level excitation; (c) the high-level excitation. 97
Figure 5.11 Simulation results of the relationship between the output power and load resistance of TEH2 under the colored noise excitation: (a) the low-level excitation; (b) the medium-level excitation; (c) the high-level excitation. 98
Figure 5.12 Simulation results of the relationship between the output power and load resistance of TEH3 under the colored noise excitation: (a) the low-level excitation; (b) the medium-level excitation; (c) the high-level excitation. 99
Figure 5.13 Experimental results of the relationship between the output power and the load resistance of TEH1 under the low-level random excitation. 100
Figure 5.14 Experimental results of the relationship between the output power and the load resistance of TEH2 under the different random excitation levels: (a) the low-level excitation; (b) the medium-level excitation. (c) the high-level excitation. 101
Figure 5.15 Experimental results of the relationship between the output power and the load resistance of TEH3 under the different random excitation levels: (a) the low-level excitation; (b) the medium-level excitation. (c) the high-level excitation. 102
Figure 5.16 The simulation results of the three TEHs: (a) the voltage responses; (b) the output powers. 106
Figure 5.17 The simulation results of the time response (upper plot) and phase portrait (lower plot) of TEH1 under the specific level of the random excitation: (a) under the A1 excitation level; (b) under the A2 excitation level. 107
Figure 5.18 The simulation results of the time response (upper plot) and phase portrait (lower plot) of TEH2 under the specific level of the random excitation: (a) under the B1 excitation level; (b) under the B2 excitation level. 107
Figure 5.19 The simulation results of the time response (upper plot) and phase portrait (lower plot) of TEH3 under the C level of the random excitation. 108
Figure 5.20 The experimental results of the three TEHs: (a) the voltage responses; (b) the

power outputs. 109
Figure 5.21 The experimental results of the time response (upper plot) and phase portrait (lower plot) of three systems under the specific level of the random excitation: (a) TEH1 under the A excitation level; (b) TEH2 under the B excitation level; (c) TEH3 under the C excitation level. 110

List of Tables

Table 2.1 Parameters of the magnets.....10
Table 2.2 The optimum values of the magnitudes of the magnetic moment vectors. 29
Table 3.1 Parameters of the energy harvester system. 46
Table 3.2 Amplitude of the input voltage signal for experimental validation. 47
Table 3.3 Optimum resistances under different frequency harmonic excitations obtained by various methods.....52
Table 4.1 Optimum resistances and maximum output powers of BEH1 obtained by the three methods. 77
Table 4.2 Optimum resistances and maximum output powers of BEH2 obtained by the three methods. 77
Table 4.3 Optimum resistances and maximum output powers of BEH3 obtained by the three methods. 78
Table 5.1 Optimum resistances and maximum output powers of TEH1 obtained by the simulation and experiment. 104
Table 5.2 Optimum resistances and maximum output powers of TEH2 obtained by the simulation and experiment. 104
Table 5.3 Optimum resistances and maximum output powers of TEH3 obtained by the simulation and experiment. 105

List of Acronyms

PZT	Lead zirconate titanate
CAD	Computer aided design
VI	Variational indicator
LEH	Linear energy harvester
BEH	Bi-stable energy harvester
TEH	Tri-stable energy harvester
RMS	Root-mean-square
PSD	Power spectrum density

Chapter 1 Introduction

In this chapter, the motivation of the research will be briefly presented and the potential problems of energy harvester in the current design will be discussed. After that, an extensive literature review will be provided to demonstrate the evolution of energy harvesters as well as their main categories. Finally, the research objectives and the outline of the thesis will be presented at the end of the chapter.

1.1 Motivation of the Research

In this century, the manufacturing of integrated circuits (ICs) has been through a great evolution, which results in the ability to make ICs have smaller size, lower price and less power consumption. This provides a growing opportunity in the Internet of Things (IoT) technology, which has various practical applications, such as the smart home system, the health care monitoring system, and the industry monitoring system. The wireless sensor network plays an essential role in linking the existing devices to the IoT. However, some of the practical circumstances need a long life-span battery to sustain the sensors. An efficient energy harvester can solve the costly battery replacement issue [1], [2]. Energy harvester is a device that can convert ambient environment energy into electrical energy. There are several forms of energy sources that could be used: solar energy [3], [4], thermal energy [5], [6], radiofrequency (RF) energy [7], [8] and mechanical energy. Vibration is a common form of mechanical motion and ubiquitous in the world around us: from the low frequency vibration such as heartbeat, breath or movement we make, to the high frequency vibration caused by automobile or aircraft engine and most of the industrial equipment. We can capture these energies from oscillation with the piezoelectric energy harvester. A shortcoming of the traditional vibration energy harvesters is the narrow operating frequency band [9]. As we know, the frequencies of the ambient environment vibration

would be changing and likely to be wideband. Therefore, the investigation of the wideband vibration energy harvester becomes the hottest topic on the energy harvester research. As it was concluded in [10], the use of nonlinear systems as energy harvesters is an efficient way to widen the operation frequency band. To fulfill this purpose, a tunable multi-stable piezoelectric energy harvester will be developed in this study. The nonlinear restoring force is generated by interaction between a magnet fixed to the base and an assembly of three magnets that is attached to the end of a cantilever beam. By adjusting the configuration of the magnets, the system can exhibit the mono-stable, bi-stable or tri-stable behavior. This study will also investigate and compare the output performances of these three different energy harvesters.

1.2 Literature Review

1.2.1 Vibration Energy Harvesters

The conception of vibration energy harvester can be traced back to 1770 when Abraham Louis Perrelet designed an automatically self-winding watch powered by human arm movements. A heavy oscillator was used inside the watch to convert the kinetic energy of human motion to the potential energy stored in the mainspring, which could maintain the gears running [11]. Such an invention defined the idea of vibration energy harvesting, which was using a mechanism to convert kinetic energy in the ambient environment to another storable energy. Nowadays, people use diverse ways to convert ambient vibration to electricity, which makes it possible to sustain various kinds of low power electrical devices. There are three kinds of vibration energy harvesters: electromagnetic type, electrostatic type, and piezoelectric type. The description of each type is given below.

The design of an electromagnetic energy harvester is based on Faraday's law. The principle of this type of energy harvesters is shown in Figure 1.1 (a), where the magnet is attached at the spring's end, and the whole structure will move when it is subjected to the excitation. Due to the relative motion between the moving magent and the coilthe magnetic

lines will cut the coil, and then the current will be generated. A great number of researchers have investigated this type of energy harvesters [12]-[16].

The second type of vibration energy harvesters is the electrostatic energy harvester. As illustrated in the upper diagram in Figure 1.1 (b), the transducer of the electrostatic vibration energy harvester can be seen as a charged capacitor that consists of two overlapping plates. When the left plate moves due to the excitation, the overlap area of the two plates will change. Since the whole amount of charges is constant, the current will be generated. There are many studies that investigated such a category [17]-[20]. This type of energy harvesters is mostly employed in MEMS (Microelectromechanical Systems) applications. The lower diagram in Figure 1.1 (b) shows the picture of the MEMS electrostatic vibration energy harvester proposed in [21].

The third type is the piezoelectric energy harvester. Figure 1.1 (c) shows a cantilever piezoelectric vibration energy harvester with a tip mass. When the system is subjected to external excitation, the tip mass will move up and down, which causes the deflection of the piezoelectric beam. Due to the piezoelectric effect, the beam's mechanical energy will be transformed into electrical energy. Besides the cantilever beam structure, there are three more types of piezoelectric energy harvester, which are: circular diagram structure [22], [23], cymbal type [24], [25], and stack configuration [26], [27]. To further increase the harvesting efficiency, the hybrid energy harvester which employs piezoelectric-electromagnetic [28]-[30] or piezoelectric-electrostatic mechanism [31], [32] has also been investigated during recent years. Since this study focuses on the cantilever based piezoelectric vibration energy harvester, a full description of such a category is introduced in the next section.

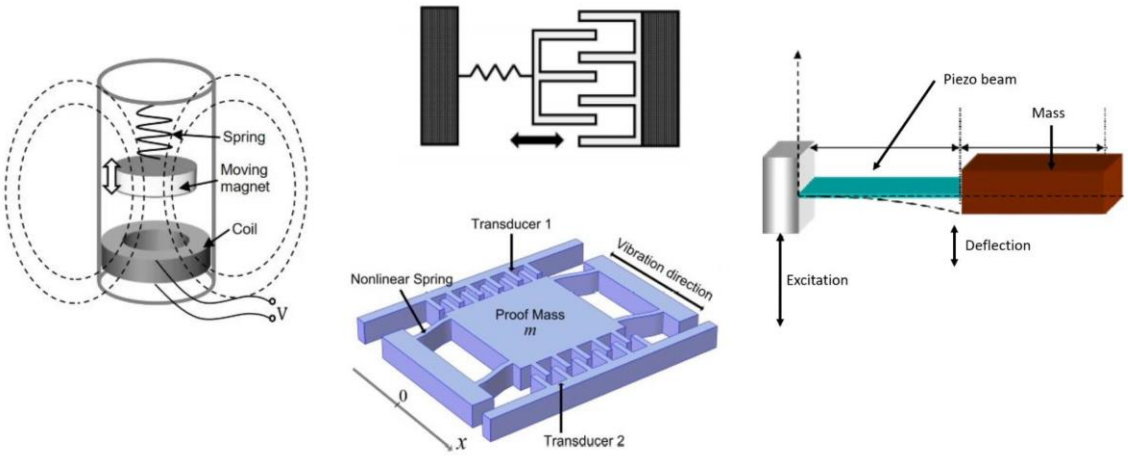

Figure 1.1 Schemes of three vibration energy harvesters (a) electromagnetic energy harvester[1]; (b) electrostatic energy harvester [21]; (c) piezoelectric energy harvester[1].

1.2.2 Cantilevered Piezoelectric Energy Harvester

The cantilevered piezoelectric transducer was first used in various kinds of force or acceleration sensors. Later, people found that it could be utilized in both macroscale [33], [34] and microscale [35] piezoelectric energy harvester applications. The studies reported in [36], [37] investigated the fundamentals of the linear energy harvester (LEH) numerically and experimentally. The results indicated that a linear oscillator had a narrow operating frequency band, because it only performed efficiently at resonance. In order to increase frequency bandwidth, various improvement methods have been proposed, for example, the frequency tuning systems [38]-[40], the multi-modal systems [41], [42], or the nonlinear energy harvesters [43]-[45]. According to the system stability, the nonlinear energy harvesters can be classified as mono-stable and multi-stable such as bi-stable or tri-stable. The nonlinearity can be derived by magnets interaction. Figure 1.2 shows the mono-

[1] https://www.allaboutcircuits.com/technical-articles/introduction-to-vibration-energy-harvesting/

stable piezoelectric energy harvester proposed in [46]. It could exhibit both hardening and softening behaviors by manually adjusting the distance *d* and *h*. The study showed that the nonlinear configuration had the advantage in responding to a wider frequency band excitation. Further, the mono-stable configuration proposed in [47] exhibited a good performance under a low excitation level.

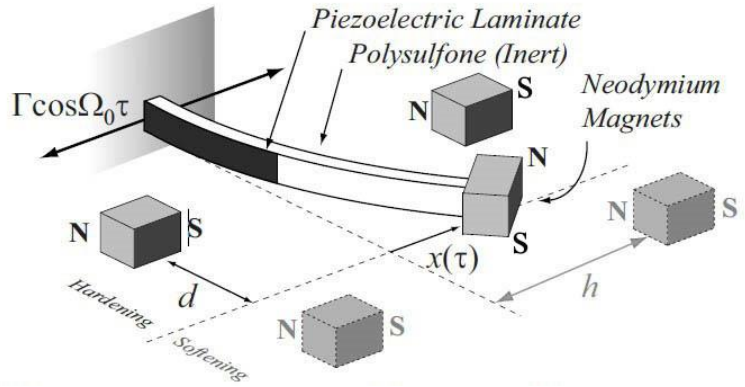

Figure 1.2 Schematic of a tunable mono-stable cantilevered piezoelectric energy harvester [46].

As illustrated in Figure 1.3 (a), a bi-stable energy harvester (BEH) can be generated by using a magnet that is attached to the free end of a piezoelectric cantilever beam and a magnet that is fixed on the base. This magnetic field induces a repulsive force between the magnets so that the beam has two stable positions: left and right. Such a configuration was proposed in [48]-[50]. The study proved that the bi-stable restoring force could enhance power output performance. The study reported in [51] investigated the responses of a BEH to white or exponentially correlated Gaussian excitation. It showed that the depth and separation distance between the potential wells play a significant role in determining the output power. The better performance of the bi-stable system subjected to stochastic excitation was also demonstrated in [52], [53]. Furthermore, to enhance the power output performance in a low-level excitation environment, tri-stable energy harvesters (TEHs) were proposed.

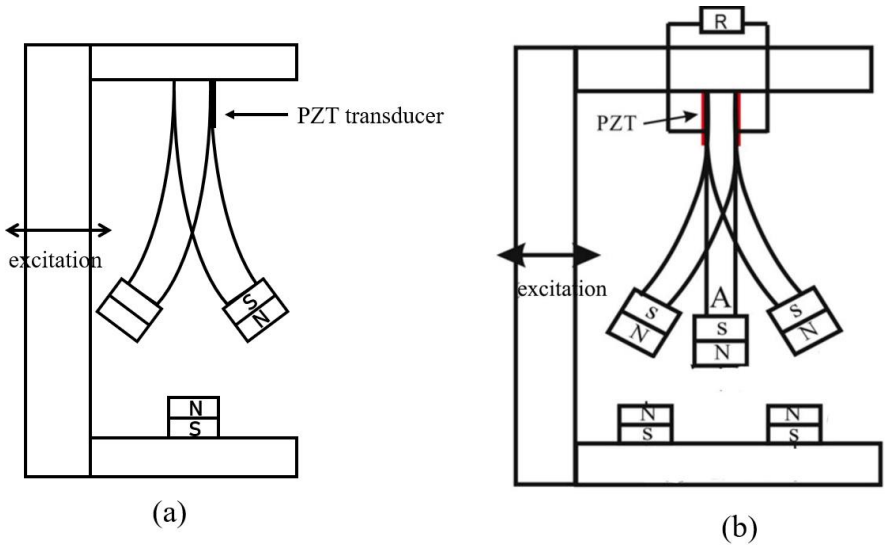

Figure 1.3 Schematic of multi-stable cantilevered piezoelectric energy harvesters (a) bi-stable configuration; (b) tri-stable configuration [54].

Based on the configuration of the bi-stable system, a tri-stable state was achieved by using two fixed magnets. As demonstrated in Figure 1.3 (b), the TEH proposed in [54] consists of an oscillating magnet that is placed between two stationary magnets. The tri-stable intensity can be tuned by varying the distance between the fixed magnets and the magnet on the beam's tip. The TEHs proposed in [55]-[57] were obtained by tuning the angular orientation of the fixed magnets. The numerical model and experimental validation of a THE in the stochastic environment were conducted in [58]. The study showed that the voltage output of the optimally designed tri-stable system outperformed that of the BEH. However, the design such as the one in [54] took a large space in order to place the fixed magnets, which is undesirable in realization through a micro-electromechanical system. Besides, low efficiency is another shortcoming, because when the beam swings to one side, the stationary magnet on the other side has little effect on the oscillating magnet. To overcome these two defects, a new configuration of magnets is proposed in this study.

1.2.3 Modelling Methods of the Cantilevered Piezoelectric Energy Harvester

There are two kinds of modelling approaches that are employed in developing a mathematical model of the cantilevered piezoelectric energy harvester: the lumped parameter modelling method [59]-[61] and the distributed parameter modelling method [36], [62]-[64].

The former method is also known as single-degree-of-freedom modelling. In this approach, the energy harvester is considered as a mass-spring-damper system. This method offers convenience to obtain the closed-form expressions of the system's model, and moreover, to analyze the system's electromechanical characteristics, including optimization and prediction of the output power for the given excitation.

The second approach is a combination of Hamilton's principle and the Rayleigh-Ritz method which employs the Euler-Bernoulli beam assumption. Compared to the first method, the distributed parameter method can provide a much accurate model, which could obtain the electromechanical response in the higher-order vibration modes [65]. However, if the natural frequencies of the higher vibration modes are much higher than the natural frequency of the first vibration mode, only a little difference exists between the models obtained from the two approaches [66]. In this study, the second method is chosen and only the first vibration mode of the beam is considered.

1.3 Research Objectives

In this study, a tunable multi-stable piezoelectric energy harvester is proposed. Different from the previous designs such as the one in [54], the proposed apparatus consists of a cantilever beam attached by an assembly of three magnets that face a stationary magnet. The assembly consists of a center magnet that is fixed to the beam's tip and two side magnets that can be slided along the beam. By varying the configuration of the magnet assembly and the distance between the magnet assembly and the stationary magnet, the

system can assume three states: tri-stable, bi-stable and mono-stable, respectively. The objectives of this thesis research are defined as follows: (1) to develop a tunable multi-stable apparatus; (2) to identify the restoring force model for the apparatus; (3) to develop and verify the electromechanical model of the system; (4) to compare the output performances of the LEH, BEHs and THEs under the colored noise excitation.

1.4 Thesis Outline

The thesis is organized as follows. In Chapter 2, the dynamic model of the proposed energy harvesting system is developed and validated. According to the measured data, the genetic algorithm is employed to optimize the model. In Chapter 3, a description of the piezoelectric effect is introduced. Based on that, the voltage responses for the linearized mono-stable energy harvester under harmonic and colored noise excitation are investigated, respectively. Further, the optimum resistance values for the different excitation conditions are also determined. Chapter 4 and Chapter 5 investigate the output performances of the BEHs and TEHs under the colored noise excitation, respectively. The optimum resistance values for these two types of the energy harvesters are determined to maximize the output power. Finally, Chapter 6 draws the main conclusions of the study and discusses future works.

Chapter 2 Apparatus and Modeling

2.1 Configuration of the Apparatus

Figure 2.1 shows a CAD drawing of the piezoelectric energy harvester developed for this study. The piezoelectric energy harvester consists of a cantilever beam and four magnets. The cantilever beam is composed of a bimorph piezoelectric beam (S128-J1FR-1808YB, Midé Corporation) and a stainless-steel beam. The free end of the beam is attached with three cylindrical bar magnets A, B, and C. The small size magnet B is held by a holder that is fixed on the tip of the beam and the medium size magnets A and C are held by a holder that can move along the beam. The cantilever beam is clamped to a stand that is fastened to a base. A large size cylindrical bar magnet D is fixed in a stand that can slide along the base. When the cantilever beam is at its equilibrium position or undeflected, the four magnets situate on the same vertical plane and magnets B and D are collinear. By sliding the stand for magnet D, its distance from magnet B can be adjusted. By sliding the holder for magnets A and C, their distance from magnet B can be adjusted. Table 1 lists some relevant parameters of the magnets.

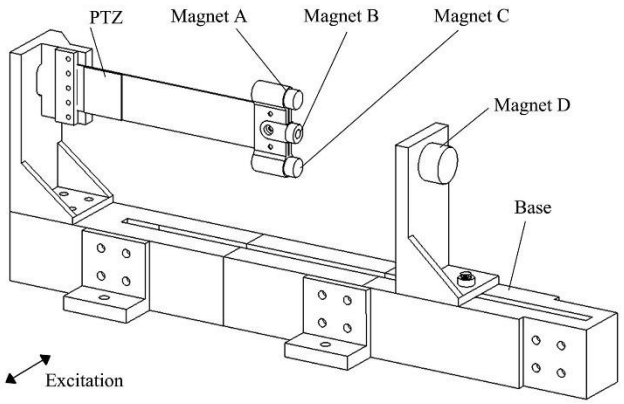

Figure 2.1 Schematic of the tunable multi-stable piezoelectric energy harvester.

Table 2.1 Parameters of the magnets

Magnet	Material	Diameter (mm)	Length (mm)
A, C	N52	12.70	25.40
B	N52	7.94	7.94
D	N52	25.40	25.40

Figure 2.2 illustrates the spatial positions and polarities of the four magnets where $\boldsymbol{m}_A$, $\boldsymbol{m}_B$, $\boldsymbol{m}_C$, $\boldsymbol{m}_D$ are the magnetic moment vectors, A_0, B_0, C_0 denote the center positions of magnets A, B and C when the beam is undeformed, A, B, and C are the center positions of magnets A, B and C when the beam is deformed, $\boldsymbol{r}_{DA}$ represents a vector from A to D, $\boldsymbol{r}_{DB}$ represents a vector from B to D, and vector's projection on the *x*-*y* plane is represented by $\boldsymbol{r}_{DAxy}$. Note that the direction of $\boldsymbol{m}_B$ is opposite to that of $\boldsymbol{m}_A$, $\boldsymbol{m}_C$, and $\boldsymbol{m}_D$. The total restoring force f_x of the system in the *x*-direction consists of a restoring force f_e due to the beam's elasticity, an attractive magnetic force f_{DBx} between magnet D and magnet B and two repulsive magnetic forces f_{DAx} between magnet D and magnet A, and f_{DCx} between magnet D and magnet C. Since magnets A and C are identical and symmetrical about the central line of the beam, the values of f_{DAx} and f_{DCx} are equal. Then the total restoring force can be expressed as:

$$f_x = f_e + f_{DBx} + f_{DAx} + f_{DCx} = f_e + f_{DBx} + 2f_{DAx} \tag{2.1}$$

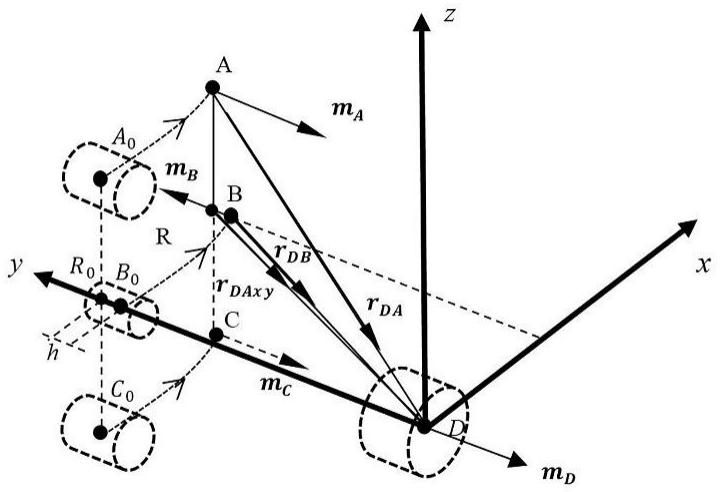

Figure 2.2 Illustration of the spatial positions and polarities of the magnets.

Figure 2.3 shows the front view of Figure 2.2, where d is the distance between magnet D and magnet B when the beam is undeformed and h is the axial gap between the center of magnet A or C and the center of magnet B, l is the length of the cantilever beam, and w is the distance between the axis of magnet B and that of magnet A or C. Figure 2.4 shows the top view of Figure 2.2 where the vectors $\boldsymbol{m}_B$, $\boldsymbol{m}_D$ and $\boldsymbol{r}_{DB}$ are indicated.

As shown in Figure 2.4, α is the angle between $\boldsymbol{m}_B$ and $\boldsymbol{m}_D$, and β is the supplementary angle between $\boldsymbol{m}_D$ and $\boldsymbol{r}_{DB}$, x and y are the transverse and longitudinal displacements of the center of magnet B, respectively. Since the slope of the beam's tip is relatively small, then it is assumed that $\angle BOB_0 \approx \alpha$. The relationship between x and y can be derived from the trigonometric relationship in triangle ORB_0 as follow:

$$y = l - \sqrt{l^2 - x^2} \tag{2.2}$$

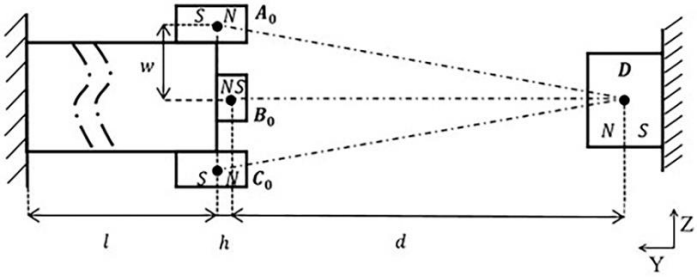

Figure 2.3 Front view of the apparatus.

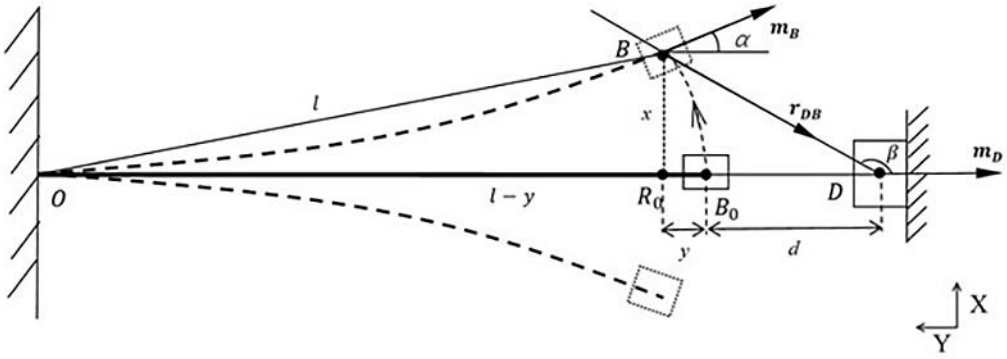

Figure 2.4 Top view of the apparatus.

In this study, the magnetic dipole approach is used to calculate the magnetic force between two magnets [67], [68]. Firstly, the magnetic force between magnet D and magnet B is considered. According to the dipole theory, the force exerted by magnet B on D is given by:

$$\boldsymbol{f}_{DB} = \nabla\left(\boldsymbol{B}_{DB} \cdot m_B\right) \tag{2.3}$$

where $\boldsymbol{B}_{DB}$ is the magnetic flux density generated by magnet D upon B which is of the form：

$$\boldsymbol{B}_{DB} = -\frac{\mu_0}{4\pi}\nabla\frac{\boldsymbol{m}_D \cdot \boldsymbol{r}_{DB}}{r_{DB}^3} \tag{2.4}$$

where r_{DB} is the magnitude of $\boldsymbol{r}_{DB}$. It can be proved that the following operation holds:

$$\nabla \frac{\boldsymbol{m}_D \cdot \boldsymbol{r}_{DB}}{r_{BD}^3} = \frac{1}{r_{DB}^3} \nabla \left(\boldsymbol{m}_D \cdot \boldsymbol{r}_{DB} \right) + \boldsymbol{m}_D \cdot \boldsymbol{r}_{DB} \nabla \frac{1}{r_{DB}^3}. \tag{2.5}$$

The gradient functions Eq. (2.6) and Eq. (2.7) given below can be used to simplify the expression in Eq. (2.5)

$$\nabla \frac{1}{r^n} = \begin{pmatrix} \partial / \partial x \\ \partial / \partial y \\ \partial / \partial z \end{pmatrix} \frac{1}{r^n} = -\frac{n}{r^{n+1}} \begin{pmatrix} x / r \\ y / r \\ z / r \end{pmatrix} = -\frac{n\boldsymbol{r}}{r^{n+2}} \tag{2.6}$$

$$\begin{aligned} \nabla \left(\boldsymbol{v}_1 \cdot \boldsymbol{r} \right) = \begin{pmatrix} \partial / \partial x \\ \partial / \partial y \\ \partial / \partial z \end{pmatrix} \left(\boldsymbol{v}_1 \cdot \boldsymbol{r} \right) &= \begin{pmatrix} \partial / \partial x (x_1 x + y_1 y + z_1 z) \\ \partial / \partial y (x_1 x + y_1 y + z_1 z) \\ \partial / \partial z (x_1 x + y_1 y + z_1 z) \end{pmatrix} \\ &= \begin{pmatrix} x_1 \\ y_1 \\ z_1 \end{pmatrix} = \boldsymbol{v}_1 \end{aligned} \tag{2.7}$$

Substituting Eq. (2.5) into Eq. (2.4) then into Eq. (2.3) yields.

$$
\begin{aligned}
\boldsymbol{f}_{DB} &= -\frac{\mu_0}{4\pi}\nabla\left\{\left[\frac{1}{r_{DB}^3}\nabla\left(\boldsymbol{m}_D\cdot\boldsymbol{r}_{DB}\right)+\boldsymbol{m}_D\cdot\boldsymbol{r}_{DB}\nabla\frac{1}{r_{DB}^3}\right]\cdot\boldsymbol{m}_B\right\}\\
&= -\frac{\mu_0}{4\pi}\nabla\left\{\left[\frac{\boldsymbol{m}_{\mathrm{D}}}{r_{DB}^3}-\left(\boldsymbol{m}_D\cdot\boldsymbol{r}_{DB}\right)\frac{3\boldsymbol{r}_{\mathrm{DB}}}{r_{DB}^5}\right]\cdot\boldsymbol{m}_B\right\}\\
&= -\frac{\mu_0}{4\pi}\nabla\left[\frac{\boldsymbol{m}_D\cdot\boldsymbol{m}_B}{r_{DB}^3}-3\left(\boldsymbol{m}_D\cdot\boldsymbol{r}_{DB}\right)\frac{\left(\boldsymbol{r}_{DB}\cdot\boldsymbol{m}_B\right)}{r_{DB}^5}\right]\\
&= -\frac{\mu_0}{4\pi}\left[\left(\boldsymbol{m}_D\cdot\boldsymbol{m}_B\right)\nabla\frac{1}{r_{DB}^3}-3\left(\boldsymbol{m}_D\cdot\boldsymbol{r}_{DB}\right)\left(\boldsymbol{r}_{DB}\cdot\boldsymbol{m}_B\right)\nabla\frac{1}{r_{DB}^5}\right.\\
&\quad\left.-3\frac{\left(\boldsymbol{m}_D\cdot\boldsymbol{r}_{DB}\right)}{r_{DB}^5}\nabla\left(\boldsymbol{m}_B\cdot\boldsymbol{r}_{DB}\right)-3\frac{\left(\boldsymbol{m}_B\cdot\boldsymbol{r}_{DB}\right)}{r_{DB}^5}\nabla\left(\boldsymbol{m}_D\cdot\boldsymbol{r}_{DB}\right)\right]\\
&= -\frac{\mu_0}{4\pi}\left[\left(\boldsymbol{m}_D\cdot\boldsymbol{m}_B\right)\left(-\frac{3\boldsymbol{r}_{DB}}{r_{DB}^3}\right)-3\left(\boldsymbol{m}_D\cdot\boldsymbol{r}_{DB}\right)\left(\boldsymbol{r}_{DB}\cdot\boldsymbol{m}_B\right)\left(-\frac{5\boldsymbol{r}_{DB}}{r_{DB}^7}\right)\right.\\
&\quad\left.-3\frac{\left(\boldsymbol{m}_D\cdot\boldsymbol{r}_{DB}\right)}{r_{DB}^5}\boldsymbol{m}_B-3\frac{\left(\boldsymbol{m}_B\cdot\boldsymbol{r}_{DB}\right)}{r_{DB}^5}\boldsymbol{m}_D\right]\\
&= \frac{3\mu_0 m_D m_B}{4\pi r_{DB}^4}\left[\hat{\boldsymbol{r}}_{DB}\left(\hat{\boldsymbol{m}}_D\cdot\hat{\boldsymbol{m}}_B\right)-5\hat{\boldsymbol{r}}_{DB}\left(\hat{\boldsymbol{m}}_D\cdot\hat{\boldsymbol{r}}_{DB}\right)\left(\hat{\boldsymbol{r}}_{DB}\cdot\hat{\boldsymbol{m}}_B\right)\right.\\
&\quad\left.+\hat{\boldsymbol{m}}_B\left(\hat{\boldsymbol{m}}_D\cdot\hat{\boldsymbol{r}}_{DB}\right)+\hat{\boldsymbol{m}}_D\left(\hat{\boldsymbol{m}}_B\cdot\hat{\boldsymbol{r}}_{DB}\right)\right]
\end{aligned}
\tag{2.8}
$$

where m_B, m_D, and r_{BD} are the magnitudes of $\boldsymbol{m}_B$, $\boldsymbol{m}_D$, and $\boldsymbol{r}_{DB}$, respectively, the values of m_B and m_D can be represented by m_B=$M_B V_B$ and m_D=$M_D V_D$ where M_B and M_D are the magnetic residual flux density and V_B and V_D are the volume of the magnets, $\hat{\boldsymbol{m}}_B$, $\hat{\boldsymbol{m}}_D$ and $\hat{\boldsymbol{r}}_{DB}$ are the unit vector of $\boldsymbol{m}_B$, $\boldsymbol{m}_D$, and $\boldsymbol{r}_{DB}$. These unit vectors can be expressed as:

$$
\begin{aligned}
&\hat{\boldsymbol{m}}_B = \left[\sin(\alpha)\ \ -\cos(\alpha)\ \ 0\right];\ \hat{\boldsymbol{m}}_D = \left[0\ \ -1\ \ 0\right];\\
&\hat{\boldsymbol{r}}_{DB} = \left[-\sin(\beta)\ \ \cos(\beta)\ \ 0\right].
\end{aligned}
\tag{2.9}
$$

Substituting the above unit vectors in the dot products of Eq. (2.8) yields:

$$
\begin{aligned}
\boldsymbol{f}_{DB} &= \frac{3\mu_0 m_D m_B}{4\pi r_{DB}^4}\left[\hat{\boldsymbol{r}}_{DB}\cos(\alpha)-5\hat{\boldsymbol{r}}_{DB}\cos(\beta)\cos(\beta-\alpha)\right.\\
&\quad\left.-\hat{\boldsymbol{m}}_B\cos(\beta)-\hat{\boldsymbol{m}}_D\cos(\beta-\alpha)\right].
\end{aligned}
\tag{2.10}
$$

Now the magnetic force in the *x*-direction can be obtained in the following form:

$$f_{DBx} = -\frac{3\mu_0 m_D m_B}{4\pi r_{BD}^4}\left\{\sin(\beta)\left[\cos(\alpha) - 5\cos(\beta)\cos(\beta-\alpha)\right] + \sin(\alpha)\cos(\beta)\right\} \tag{2.11}$$

From Figure 2.4, the trigonometric relationship in Eq. (2.11) can be expressed as follows:

$$\sin(\alpha) = \frac{x}{l};\ \cos(\alpha) = \frac{l-y}{l} \tag{2.12}$$

$$\sin(\beta) = \frac{x}{r_{DB}};\ \cos(\beta) = -\frac{y+d}{r_{DB}} \tag{2.13}$$

$$\begin{aligned}\cos(\beta-\alpha) &= \cos(\alpha)\cos(\beta) + \sin(\alpha)\sin(\beta)\\ &= \frac{l-y}{l}\left(-\frac{y+d}{r_{DB}}\right) + \frac{x}{r_{DB}}\frac{x}{l}\\ &= \frac{x^2 - ly - ld + yd + y^2}{lr_{DB}}\end{aligned} \tag{2.14}$$

Substituting Eq. (2.12), Eq. (2.13) and Eq. (2.14) into Eq. (2.11) results in the magnet force between magnet B and magnet D in the *x*-direction:

$$f_{DBx} = -\frac{3\mu_0 m_D m_B x}{4\pi r_{DB}^5 l}\left\{l - 2y - d - \frac{5}{r_{DB}^2}\left[-y^3 + (l-2d)y^2 + \left(2dl - d^2\right)y + d^2 l - (y+d)x^2\right]\right\}. \tag{2.15}$$

Following the same process given above, the magnetic force between magnet A and magnet D can be found to be:

$$f_{DAx} = \frac{3\mu_0 m_D m_A x}{4\pi r_{DA}^4 l}\left\{\frac{l-2y-d_0}{r_{DAxy}} - \frac{5}{r_{DAxy}^3}\left[-y^3 + (l-2d_0)y^2 + \left(2d_0 l - {d_0}^2\right)y + {d_0}^2 l - (y+d_0)x^2\right]\right\} \tag{2.16}$$

where $d_0 = d + h$.

The restoring force due to the beam's elasticity is assumed to be linear as follows:

$$f_e = k_b x \tag{2.17}$$

where k_b is the stiffness of the beam which can easily be determined experimentally. Substituting Eq. (2.15), Eq. (2.16) and Eq. (2.17) into Eq. (2.1) yields the analytical

model of the total restoring force f_x:

$$f_x = k_b x - \frac{3\mu_0 m_D m_B x}{4\pi r_{DB}^5 l}\left\{l-2y-d-\frac{5}{r_{DB}^2}\left[-y^3+(l-2d)y^2+(2dl-d^2)y+d^2l-(y+d)x^2\right]\right\}. + \frac{6\mu_0 m_D m_A x}{4\pi r_{DA}^4 l}\left\{\frac{l-2y-d_0}{r_{DAxy}}-\frac{5}{r_{DAxy}^3}\left[-y^3+(l-2d_0)y^2+(2d_0 l-{d_0}^2)y+{d_0}^2 l-(y+d_0)x^2\right]\right\} \quad (2.18)$$

Note that the last two terms on the right-hand side of the above equation depend on the variables d and h. By tuning these two variables, three states of stability can be achieved, namely mono-stable, bi-stable, and tri-stable. In what follows, a model validation is conducted.

2.2 Validation of the Model for the Restoring Force

In this section, the restoring forces are experimentally identified in order to validate the model given by Eq. (2.18). Firstly, the restoring force of the beam is experimentally determined. Secondly, the total restoring forces that correspond to several combinations of d and h are identified by using the restoring force surface method. The identified restoring forces are compared with those from Eq. (2.18). Thirdly, an optimization is conducted to determine the best values for the magnitudes of the magnetic vectors.

2.2.1 Identification of the Restoring Force of the Beam.

As it was mentioned previously, the stiffness k_b can be obtained from the relationship between the restoring force f_e and transverse displacement x. To measure this restoring force, an experimental setup illustrated in Figure 2.5 is developed. As shown in Figure 2.5 (a), an electric dynamometer (RC Benchmark series 1520 thrust stand) is used to exert a force against the free end of the cantilever beam through a probe which is a long steel rod. A laser reflex (RF) sensor (CP24MHT80, Wenglor) is used to measure the deflection of the

beam due to the applied force. By increasing the deflection incrementally, the relationship between the force measured by the dynamometer and the deflection measured by the RF sensor can be established.

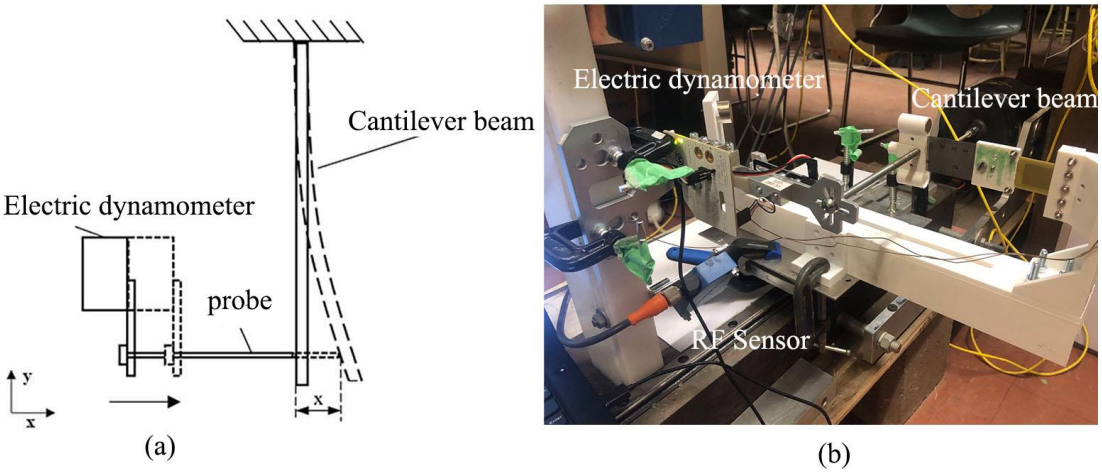

Figure 2.5 Experimental setup for measuring the restoring force of the cantilever beam: (a) schematic of the setup; (b) photo of the setup.

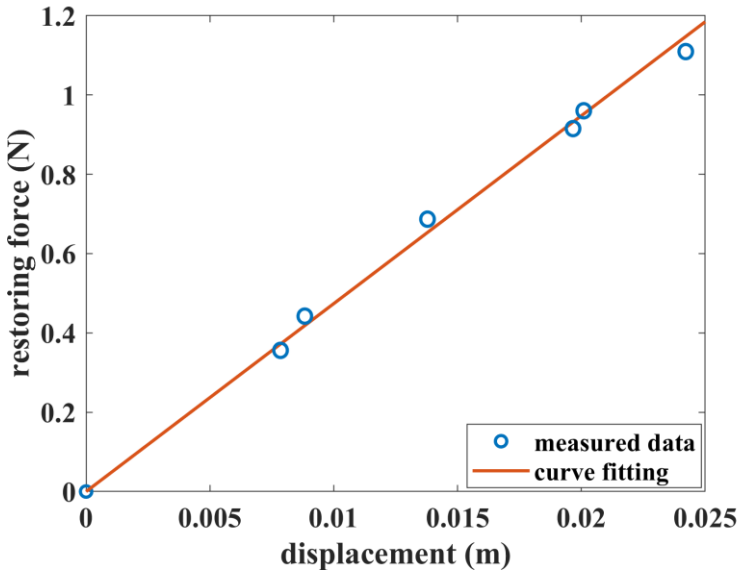

Figure 2.6 The measured restoring force of the cantilever beam.

Figure 2.6 shows the relationship between the restoring force and displacement. As a result, the linear elastic stiffness can be presented by the slop of the fitted curve, which is

founded to be k_b=47.39 N/m.

The natural frequency of the cantilever beam with the assembly of the three magnets can be determined experimentally. By tapping the beam gently, a free response is induced. By applying the Fast Fourier Transform to the measured free responses, the frequency of the response is found to be f_a=3.72 Hz. The mass of the magnet assembly can be estimated by the following equation.

$$m = \frac{k_b}{(2\pi f_a)^2} = 0.086 \text{ kg} \tag{2.19}$$

2.2.2 The Total Restoring Force Surfaces

To validate the magnetic forces determined by the dipole theory, some of the researchers directly used a digital force gauge to measure the restoring forces [69], [70]. However, the validity of these results is questionable as the measurements were conducted statically. In this study, the restoring force surface method [71] is employed to determine the restoring forces dynamically. Figure 2.7 (a) shows a photo of the experimental setup. The apparatus is mounted on a slipping table that is driven by a shaker (2809, Brüel & Kjær) through a stinger. The shaker is driven by an amplifier (2718, Brüel & Kjær). Two RF sensors (CP24MHT80, Wenglor) are used to measure the transverse displacement of the beam's tip and the base's displacement, respectively. A computer equipped with the dSPACE dS1104 data acquisition board is used to collect the sensors' data and send voltage signal to the power amplifier to drive the shaker. The control program is developed by using the Matlab Simulink which is interfaced with dSPACE Controldesk Desktop software.

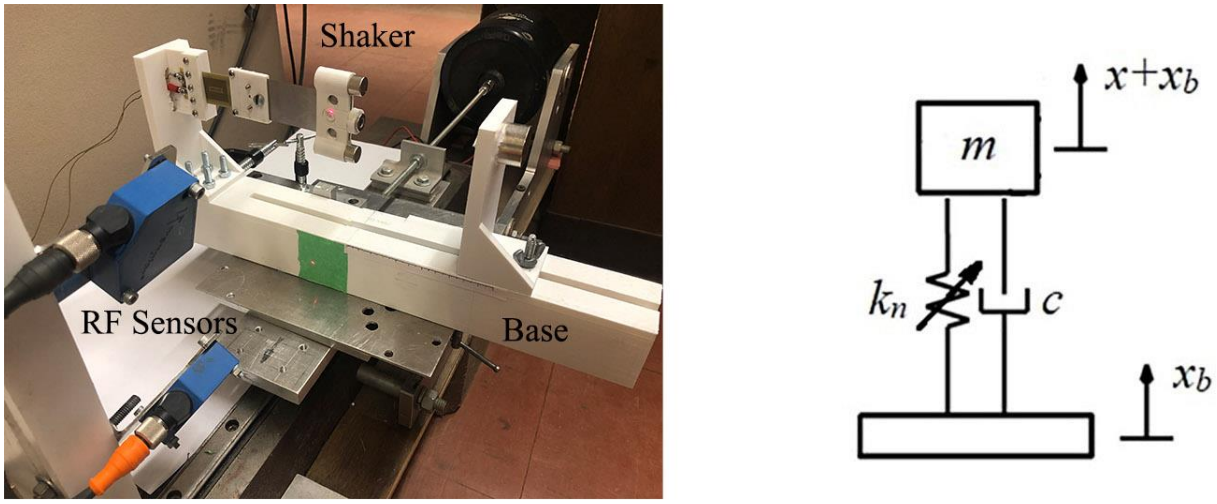

Figure 2.7 (a) Photo of the experimental setup, (b) Schematic of the model for the experimental setup.

Figure 2.7 (b) shows a schematic of the model that represents the experimental setup where x_b is the base's displacement and x is the displacement of the cantilever beam's tip relative to the base, m represents the mass of the assembly of the three magnets, c is the damping coefficient, and k_n represents the combined spring of the system. The equation of motion of this setup is given by:

$$m\left(\ddot{x}_b + \ddot{x}\right) + c\dot{x} + f\left(x\right) = 0 \tag{2.20}$$

where $f(x)$ denotes the restoring force of the combined spring. Equation (2.20) can be rewritten as:

$$F\left(x, \dot{x}\right) = -m\left(\ddot{x} + \ddot{x}_b\right) \tag{2.21}$$

A 3-dimensional plot of $F(x, \dot{x})$ verse the phase plane of x and $\dot{x}$ is referred to as the restoring force surface plot. After the displacements of the base and the beam's tip are measured by the RF sensors, their derivatives can be obtained by numerical differentiation. Therefore, the restoring force surface can be established. The excitation signal should be selected to ensure a good coverage in the phase plane. A harmonic function with a slowly modulated amplitude is chosen to drive the shaker. The voltage signal sent to the shaker

amplifier is of the form:

$$v = V\cos\left(0.01\pi t\right)\cdot\cos\left(2\pi ft\right) \tag{2.22}$$

where V and f are the amplitude and frequency of the exciting signal, respectively. The amplitude of the exciting signal is chosen to be 0.5 mV and the exciting frequency is chosen from the range of 3.5 Hz to 5 Hz by trial and error.

Figures 2.8 to 2.11 show the identified restoring force surface plots for four different combinations: case (I)=0.0407 m, h=0.0187 m; case (II) d=0.0367 m, h=0.0157 m; case (III) d=0.0407 m, h=0.0157 m, case (IV) d=0.0507 m, h=0.0187 m.

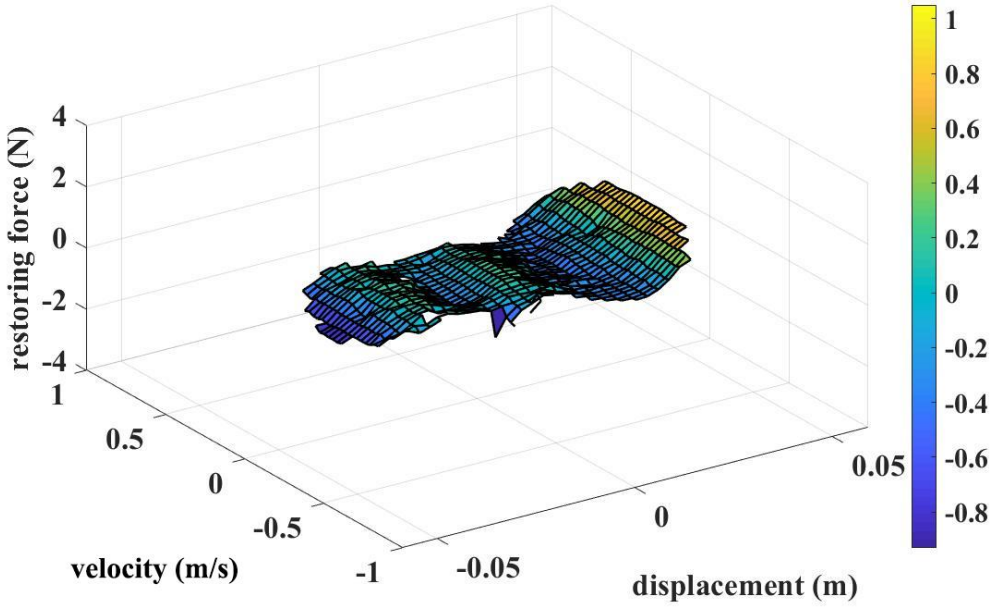

Figure2.8 Restoring force surface for the apparatus of case (I).

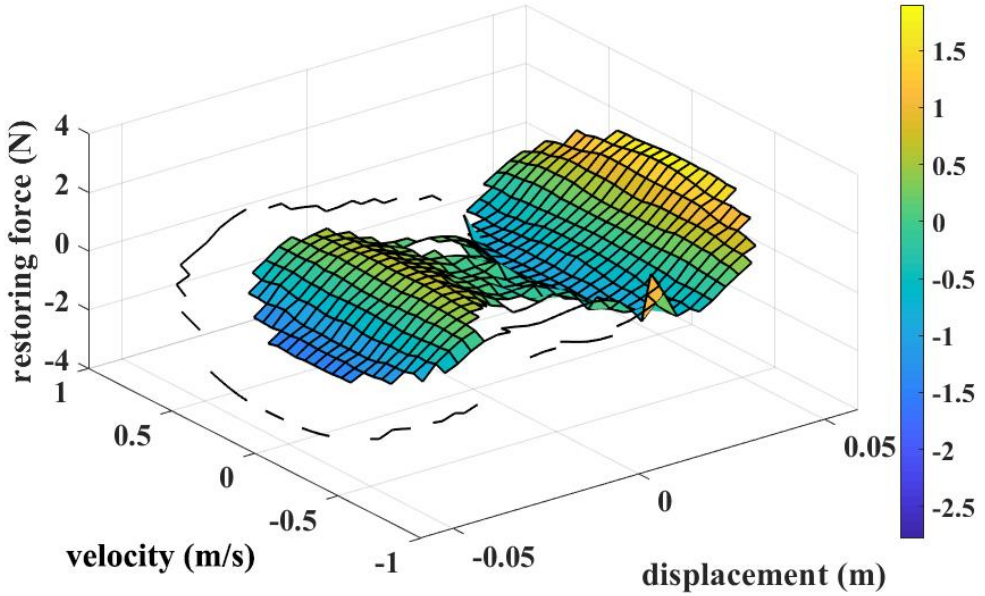

Figure 2.9 Restoring force surface for the apparatus of case (II).

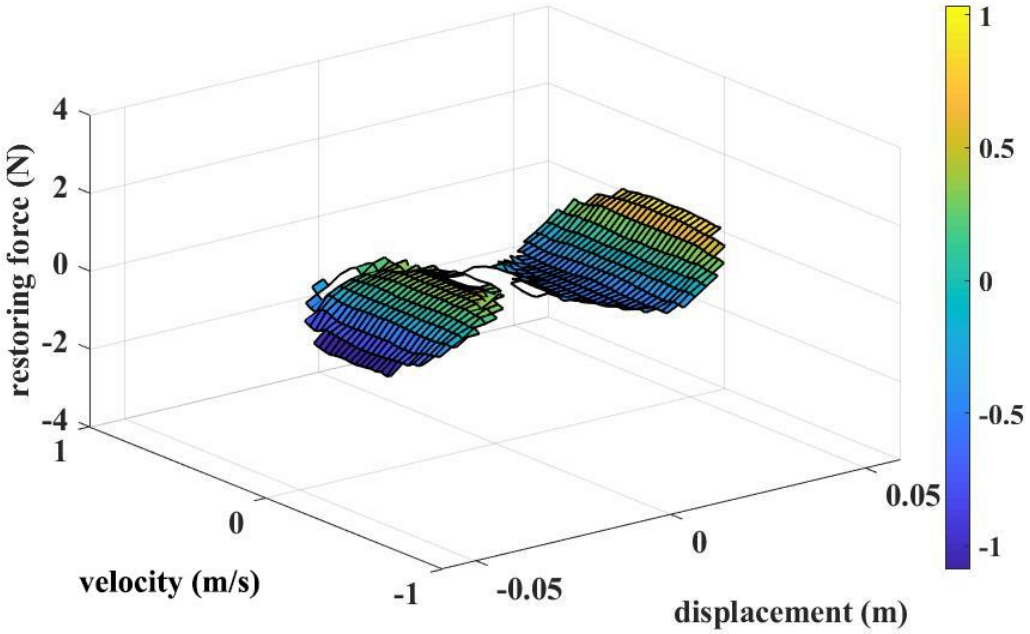

Figure 2.10 Restoring force surface for the apparatus of case (III).

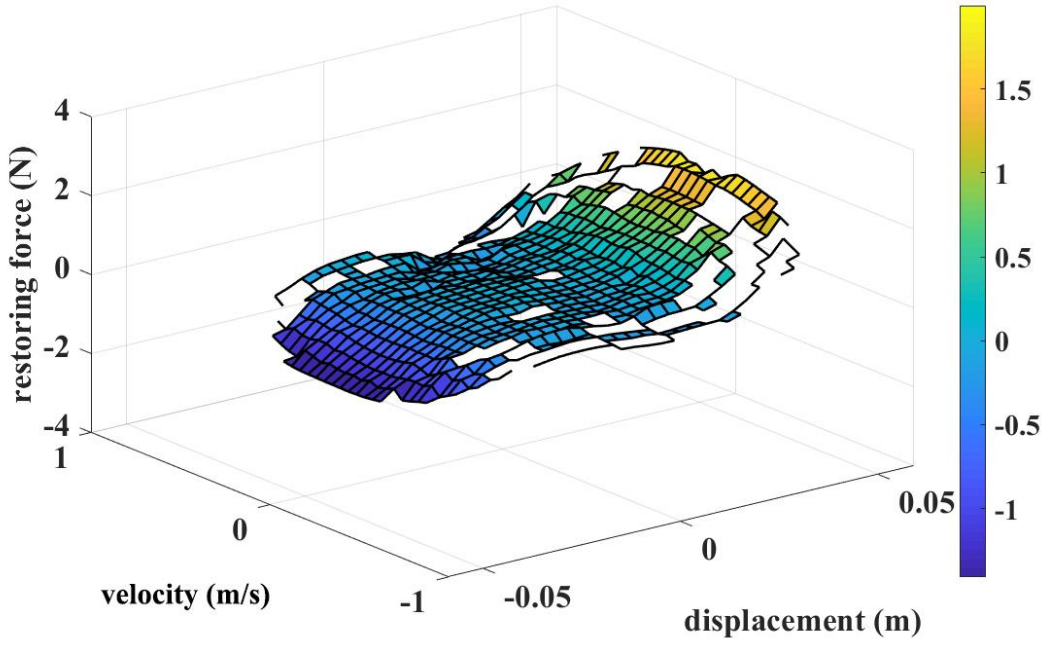

Figure 2.11 Restoring force surface for the apparatus of case (IV).

2.2.3 Comparison of the Results

Taking the section at $\dot{x} = 0$ of the restoring force surface plot results in the restoring force or $f(x) = F(x,0)$. The circles in Figure 2.12 are the results from Figures 2.8 to 2.11, respectively. The solid lines in Figure 2.12 are the analytical results based on Eq. (2.18). The parameter values used to determine the analytical results are given in Table 2.2.

Table 2.2 The parameter values used to determine the analytical restoring forces.

Symbol	**Parameters**	
	Name	**Value**
μ_0	Vacuum permeability	$4\pi\times10^{-7}$
m_D (H.m/T)	Magnitude of the magnetic moment vector of magnet D	14.953
m_B (H.m/T)	Magnitude of the magnetic moment vector of magnet B	0.456
m_A, m_C (H.m/T)	Magnitudes of the magnetic moment vectors of magnet A and C	3.738
k_b (N/m)	Stiffness of the cantilever beam	47.39
l (m)	Length of the cantilever beam	0.12
m (kg)	Mass of the system	0.086

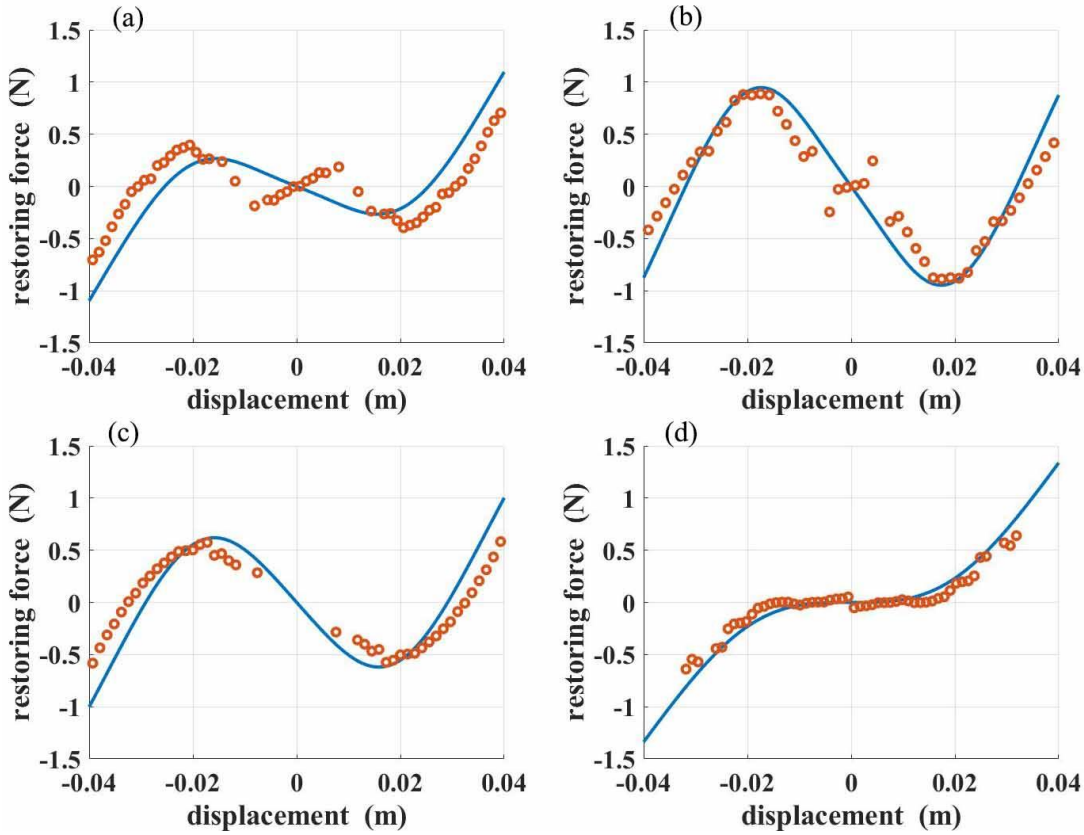

Figure 2.12 Comparison of the experimental results (red circle) and the analytical results (blue solid line) for the total restoring forces: (a) case (I); (b) case (II); (c) case (III); (d) case (IV).

In the experiments, the four cases' combinations of the tuning parameters d and h, are chosen so that the four different states of stability are obtained, i.e., (I) tri-stable, (II) transition from tri-stable to bi-stable, (III) bi-stable, and (IV) mono-stable. Comparison of the experimental results and the analytical results clearly shows that the analytical model fails to predict the first two cases and can give a satisfactory agreement for the second two cases. A possible explanation for this discrepancy is that the magnetic dipole approach idealizes the magnet as a point in the space. Therefore, the model becomes more accurate when the distance between the two magnets is large enough with respect to the dimensions of the magnets. Another reason is that the dipole model underestimates the attractive force between magnet B and magnet D when the distance between them is small. This can be easily observed from Figure 2.13 (a) and (b) that the effect of magnet B that contributes to the attractive force is insignificant. Besides, the most important difference is that the

analytical results are based on a static model while the experimental results are obtained dynamically.

2.3 Optimization of the Dipole Model

As pointed out above, the dipole model cannot accurately predict the restoring forces when the system assumes a tri-stable state. In this section, parameter optimization is carried out to improve the accuracy of the model. An examination of the dipole model shows that the magnitudes of magnetic vectors and the spatial relation for each magnet pair are crucial for determining the final result. Obviously, for a specific system setup, the geometric relationship, including the directions of the magnetic vectors and relative positions are easily measured. Hence, the magnitudes ($m_A,\ m_B,\ m_D$) of the magnetic vectors are chosen to be the parameters to be optimized. For this purpose, an objective function is defined as follow:

$$J(m_A, m_B, m_D) = \sqrt{\frac{1}{N}\sum_{i=1}^{N}(f_e(x_i) - f_a(x_i))^2} \tag{2.23}$$

where $f_e(x_i)$ is the measured restoring force, $f_a(x_i)$ is the analytical restoring force, and N is the number of the data. An optimization problem can be formulated as follow: find the best values of $m_A,\ m_B,\ m_D$ so that the objective function J is minimized.

2.3.1 Genetic Algorithm

The genetic algorithm is a well known nonlinear optimization method based on a natural selection process that emulates biological evolution. For each generation, it will search parallel from a whole population of points. Therefore, it can avoid the situation that being trapped in local optimal solution like traditional methods, which search from a single point. Figure 2.13 gives the flowchart of the genetic algorithm. In the first step, the initial ranges of the parameters and stopping criteria need to be specified. And the population size also needs to be set. This number determines how many individuals will be randomly selected from the current population and uses them as parents to produce the children for

the next generation. If the population size is big enough to cover all the search domain, it certainly has more chances to find the global minimum point, but the price is a longer computation time.

After the initialization process, the individuals of the first population are randomly generated within the specified ranges. Each of the individuals of the first generation is used in Eq. (2.18) to evaluate the corresponding analytical restoring forces. Then the analytical restoring forces and the measured ones are used in Eq. (2.23) to determine the objective function or the fitness value $J(n)$ of this individual. Once the fitness value of the population has been obtained and if at least 50 generations of offspring have been created, the following criteria would be checked to determine whether the program should continue or not.

- The smallest fitness value is smaller than the convergence tolerance λ.
- The average change in the smallest fitness value over the last 50 generations is less than the threshold $\tilde{\lambda}$, where the average change $\tilde{J}(n)$ is defined as:

$$\tilde{J}(n) = \frac{\sum_{i=n-49}^{n} \left[J(i) - J(i-1) \right]}{50 \sum_{i=n-49}^{n} J(i)} \qquad (n > 50) \tag{2.24}$$

- The generation index exceeds the maximum number of the generation N_{max}.

If any one of the above stopping conditions is fulfilled, the optimization will stop, and the individual corresponding to the smallest fitness value is chosen to be the optimum result. Otherwise, a portion of the generation is selected through a fitness-based process where fitter individuals are chosen. Then individuals of the next generation's population are generated through a combination of genetic operators: crossover and mutation, which guarantee the diversity of the offspring's chromosomes. Then the process repeats.

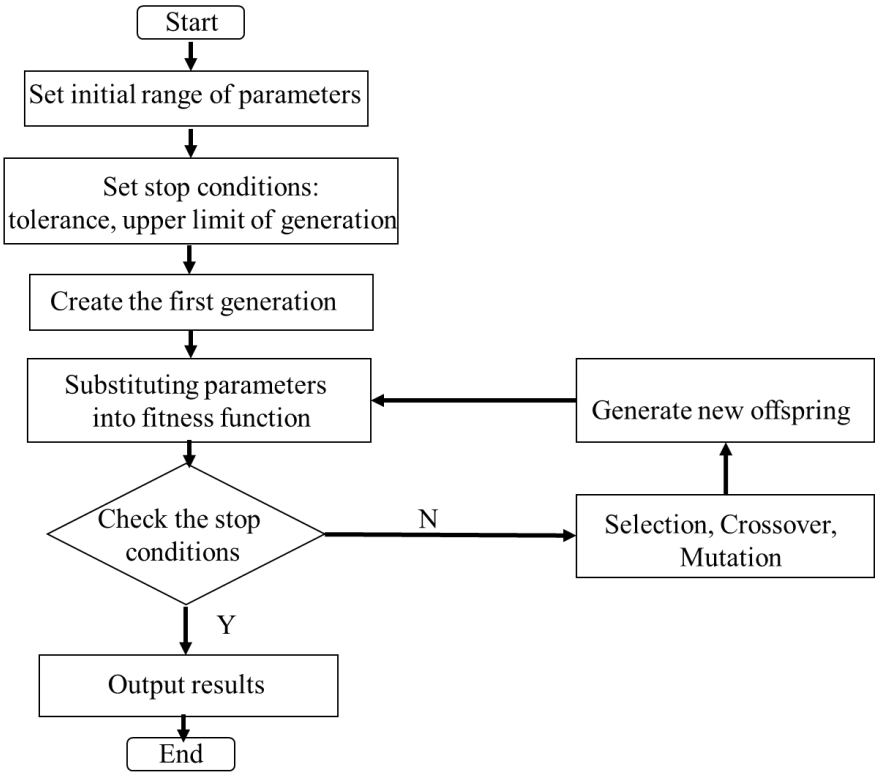

Figure 2.13 Flowchart of the genetic algorithm optimization.

2.3.2 Implementation and Results

In this study, the Matlab genetic algorithm optimization toolbox is used to solve the optimization problem. The optimization results in four sets of the best combination of the magnetic vector's amplitudes (m_A, m_B, m_D) from the four different states of the system. After that, the one that has the smallest fitness value will be chosen as the optimal parameters.

In the initialization process, the initial ranges could be approximately estimated according to the experience. In this case, the ranges of values are chosen as $1.5 \leq m_A \leq 6.5$, $0.1 \leq m_B \leq 0.8$, $6.0 \leq m_D \leq 26.7$. The convergence tolerance and the threshold of the average change of the function value are chosen to be 0.01 and 1×10^{-6}, respectively. The maximum number of generation index is set to be 300, and the population size of 1000 is used.

The experimental data for the four cases are used in the fitness calculation. And the program will run four times to find four sets of the optimum parameters. For example, in the optimization process which uses case (I)'s data as the training data, each of the individuals of the generation and the specific combination of d and h which makes the system exhibit tri-stable state is substituted in Eq. (2.18) to determine the corresponding analytical restoring forces. And then, substituting the obtained analytical restoring forces and the measured data of case (I) into Eq. (2.23) and the fitness value will be calculated. By checking the three stopping criteria, the loop will either keep running or stop and output the best individual. As shown in Figure 2.14, the optimization program stopped at the 51st epoch, because the average change of the best fitness value is less than the threshold value, and the final fitness value is J_1=0.037. By using the combination of the magnetic vectors' amplitude which obtained from the optimization of the case (I), the fitness values for the other three cases can also be calculated based on Eq. (2.18) and Eq. (2.23). As shown in the first row of Table 2.2, the calculated fitness value for the experimental data of case (II), case (III) and case (IV) is defined as J_2, J_3, and J_4, respectively. The average fitness can be represented by $\bar{J}$, who has the form of:

$$\bar{J} = \frac{1}{4}\sum_{i=1}^{4} J_i \tag{2.25}$$

After implementing the genetic algorithm to the four cases, the four sets of the optimum magnitudes of the magnetic vectors and their average fitness values can be found, which are presented in Table 2.2.

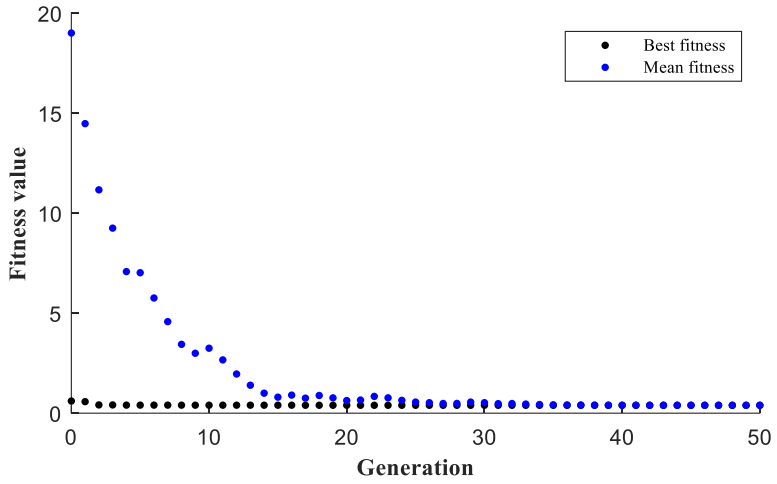

Figure 2.14 fitness value of each generation, blue circles, are the best fitness values and the black circles are the mean fitness values.

Table 2.2 The optimum values of the magnitudes of the magnetic moment vectors.

Training data	m_D (H.m/T)	m_B (H.m/T)	m_A, m_C (H.m/T)	J (N)				$\bar{J}$ (N)
				J_1	J_2	J_3	J_4	
Case (I)	25.768	0.686	3.414	0.037	0.309	0.208	0.060	0.154
Case (II)	19.467	0.637	3.505	0.188	0.104	0.107	0.082	0.120
Case (III)	20.305	0.804	3.848	0.158	0.159	0.068	0.045	0.108
Case (IV)	18.000	0.830	4.301	0.114	0.162	0.091	0.031	0.099

As shown in the last column of Table 2.2, the optimization with case (IV)'s data results in the lowest average fitness value, indicating that this set of the optimum magnitudes gives the best fit between the analytical model and the measured data for all four cases. Comparison of the optimized magnitudes in Table 2.2 and the original values given in Table 2.1 indicates that the original values underestimate the strengths of all four magnets.

Among them, magnet B sees the largest increase (82.0%) in magnitude. That explains why the analytical model yields significant discrepancy in cases (I) and (II) because magnet B plays a critical role in generating the tri-stable state behaviours.

Figure 2.15 compares the measured values and the analytical values predicted by Eq. (2.18) with the optimum results from the case (IV). Now the model is able to predict the overall trend for each of the four cases, although there are some discrepancies in the magnitudes for the tri-stable system (case (I)) and the bi-stable system (case (III)). Figure 2.16 shows the potential energies of the four cases using the optimum results of case (IV).

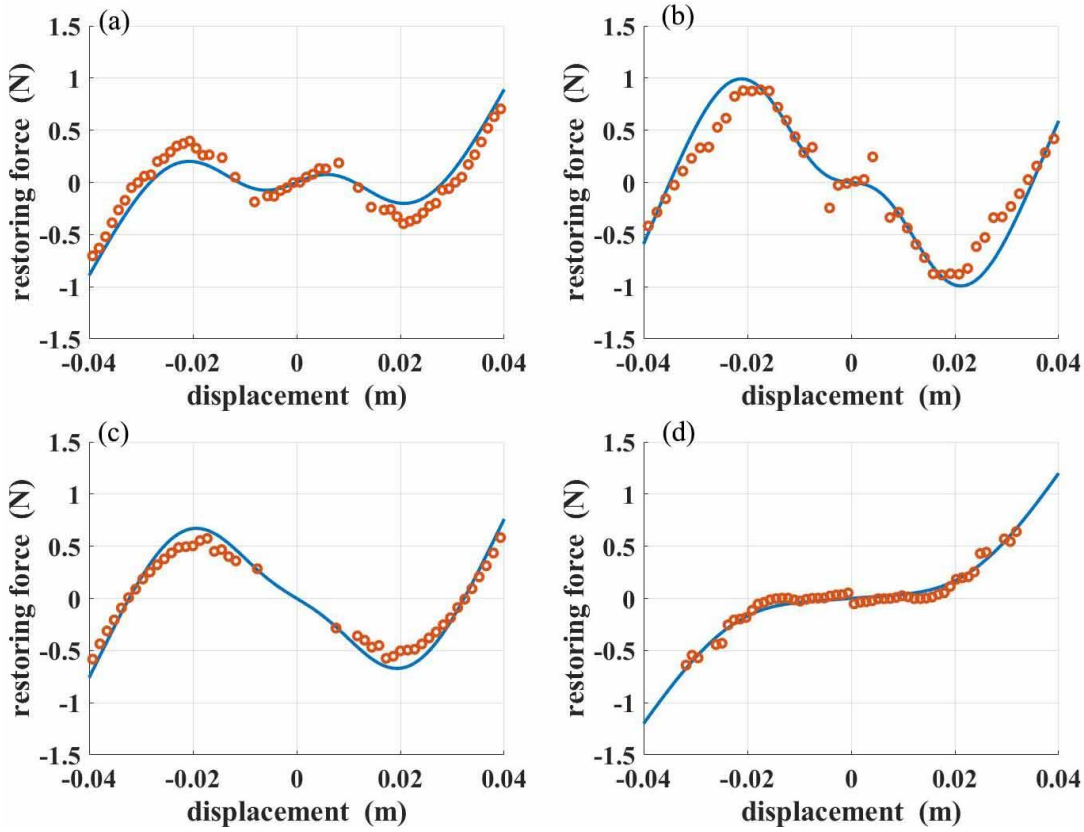

Figure 2.15 The optimized analytical results of the restoring force verse the transverse displacement for four different tuning distances, red circle for the measured data and blue solid line for the calculated result: (a) case (I); (b) case (II); (c) case (III); (d) case (IV).

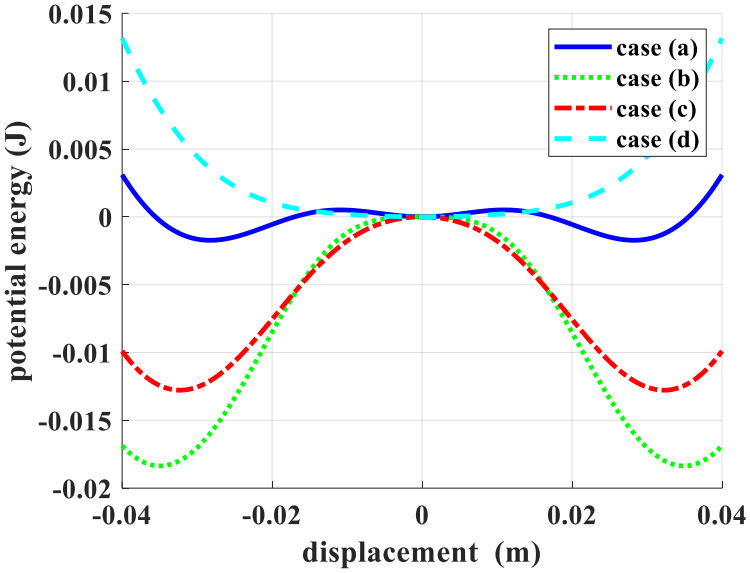

Figure 2.16 Potential energies of the four cases.

2.4 Stability State Region

In what follows, the optimum results from case (IV) are used to investigate the relationship between the stability states and the tuning parameters d and h. Figure 2.17 shows the so-called stability state region for the apparatus. The following observations can be made. Firstly, the system exhibits a bi-stable state if h is below a certain value and d varies from 0.027 m to 0.069 m. Secondly, the system assumes a tri-stable state if d is below a certain value and h varies from 0.01 m to 0.027 m. Thirdly, to achieve a mono-stable state, one can either use a large d value with a small h value or a large h value with a small d value. Fourthly, when $d \geq 0.07\ m$ and $h \geq 0.027$ m, the system can only assume a mon-stable state.

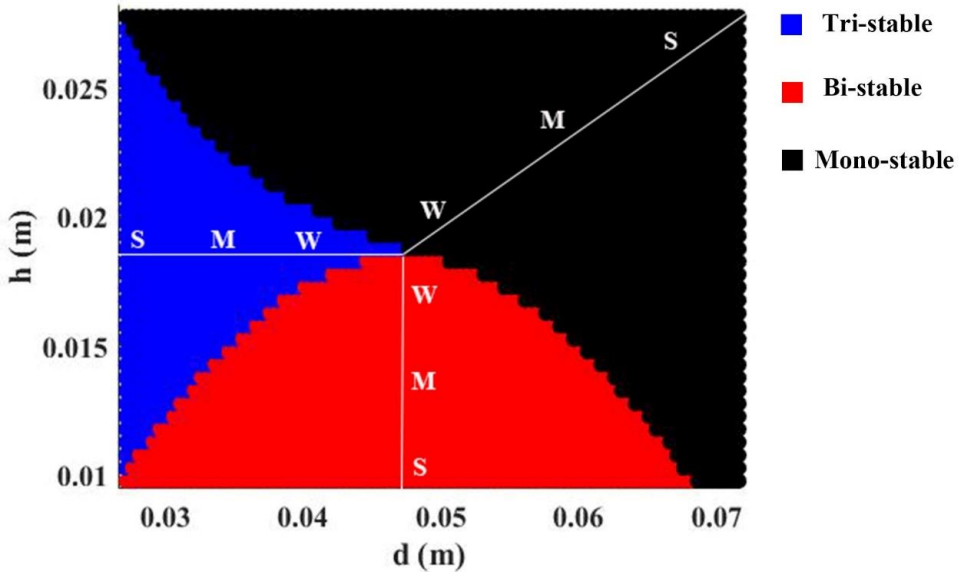

Figure 2.17 Stability state region.

As illustrated in Figure 2.18, three points are selected in each of the three regions to represent the depth of the potential wells: strong (S), medium (M), and weak (W), respectively. Figure 2.18 shows the potential energies of three tri-stable states: S (d=0.03 m, h=0.0187 m); M (d=0.035 m, h=0.0187 m); W (d=0.0407 m, h=0.0187). It can be seen that by fixing h, the shapes of the potential wells can be altered by varying d. Increasing d results in shallower wells and lower barriers. Figure 2.19 gives the potential energies of three bi-stable states: S (d=0.0407 m, h=0.01 m); M (d=0.0407 m, h=0.013 m); W (d=0.0407 m, h=0.0157 m). It can be seen that by fixing d, the potential barrier can be lowered by increasing h. Figure 2.20 shows the potential energies of three mono-stable states: S (d=0.045 m, h=0.027 m); M (d=0.045 m, h=0.022 m); W (d=0.045 m, h=0.0187 m).

For a strong or medium strength type of energy harvester, it will need a significant input excitation to make the system pass through the whole trajectory. Therefore, it is hard to accomplish an experimental validation. In the next chapter, the energy harvesting performances of three weak strength energy harvesters will be investigated.

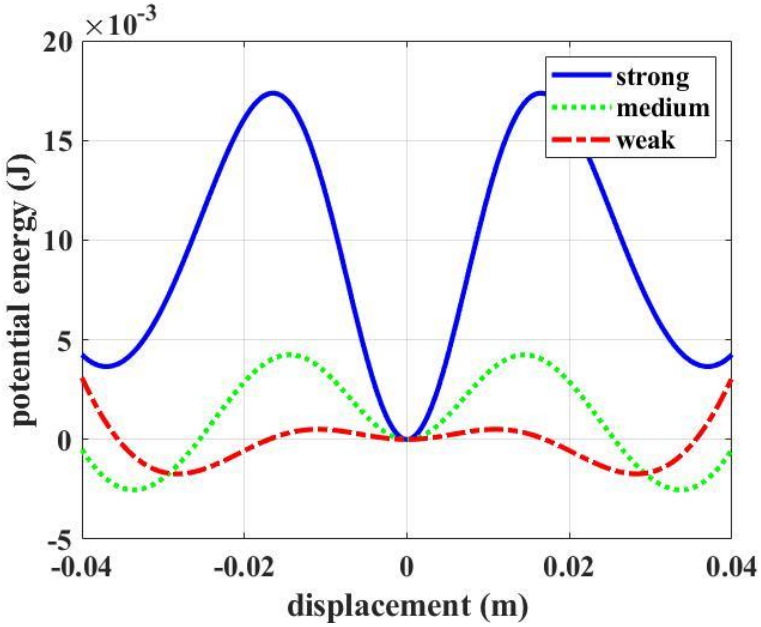

Figure 2.18 Potential energies of three different strengths: the strong, medium and weak tri-stable states.

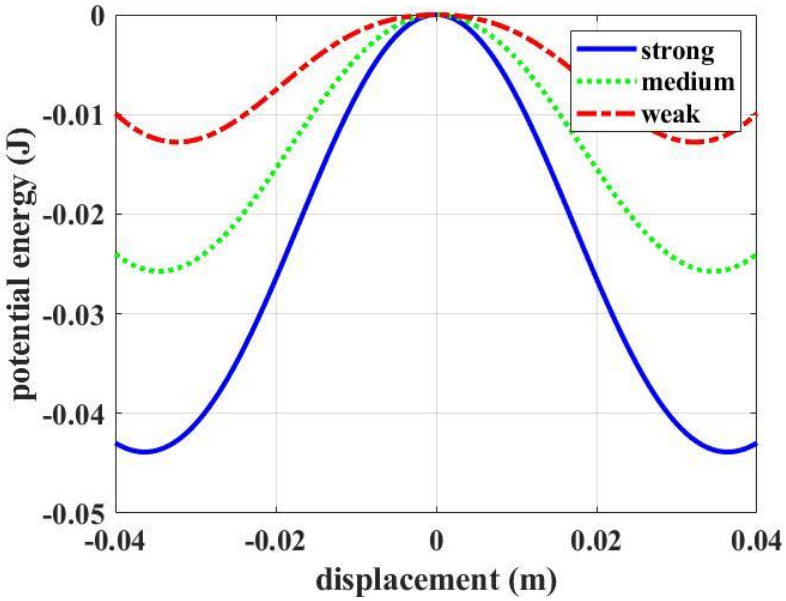

Figure 2.19 Potential energies of three different strengths: the strong, medium and weak bi-stable states.

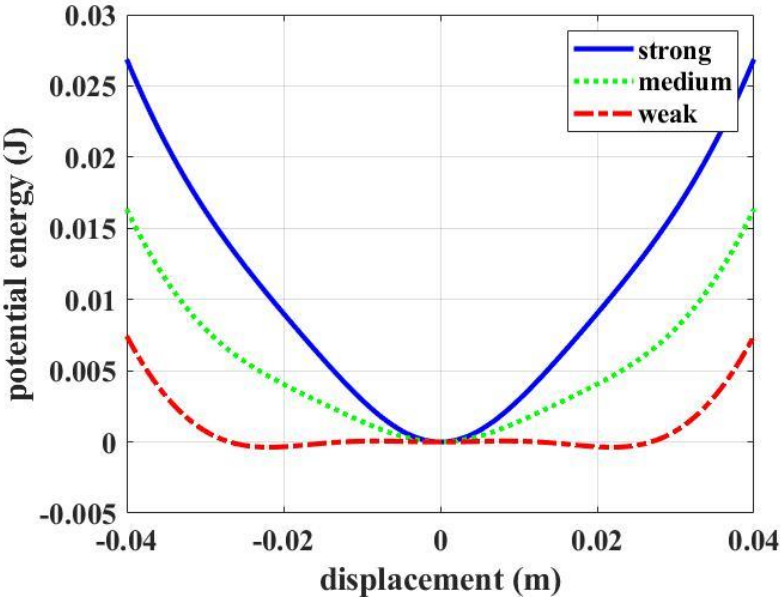

Figure 2.20 Potential energies of three different strengths: the strong, medium and weak mono-stable states.

2.5 Conclusions

In this chapter, a full description of the proposed apparatus is presented. An analytical model for the restoring force due to the magnetic interaction is developed by using the magnetic dipole approach. After that, the numerical simulation is conducted to show how the stability states can be altered. Then, an experimental validation is carried out. Finally, the genetic algorithm is used to optimize the analytical model based on the measured restoring forces. As a result, the optimized model is much accurate than the original one. Based on the optimized model, the relationship between the stability states and the tuning parameters d and h is obtained from a great number of simulation tests. Accordingly, the stable state region has been generated. Base on the dynamic model, the electromechanical model of the system will be developed in the following chapter.

Chapter 3 Piezoelectric Vibration Energy Harvester Model

The previous chapter investigated the dynamic characteristics of the developed energy harvester and founded that the system can exhibit three different states by tuning the two configuration parameters d and h. In this chapter, a full description of the piezoelectric material will be introduced. After that, the electromechanical model of the piezoelectric energy harvester will be investigated in order to explore the energy harvesting output performance for each state.

3.1 The Piezoelectric Phenomenon

Piezoelectricity is a property of some dielectric materials which can generate electric charges when they are subjected to mechanical deformation, or conversely, can produce a physical deformation when they are in the presence of an electric field. Today, a variety of piezoelectric materials have been found, including some natural crystal, human-made crystal, piezoelectric ceramic and even wood and silk [72]. The most commonly used piezoelectric material today is lead zirconate titanate (PZT), which has been chosen as the material of the energy harvesting element in this study.

Piezoelectricity is caused by the movement of electron clouds relative to their atomic centers. This process is also called spontaneous polarization. Such a character only can be found in some asymmetrical crystal structures. For example, the lead zirconate titanate has a different configuration in different temperatures. As shown in Figure 3.1, when the environment temperature is higher than the PZT's Curie temperature (about 200℃), the crystal will present a cubic configuration. In other words, it won't show any dipole or piezoelectrical character. However, below the Curie temperature, the positive ions will move a distance, and such a tetragonal structure can also gain the crystal a dipole moment. It should be noticed that the poling field of a crystal cell is from the positive dipole to the negative one, and the fields are randomly arrayed in the domain of crystals. In this case, the overall effect of a bulk of natural PZT crystal won't show any piezoelectric character.

Only if the material exhibits macroscopic polarization character, it could achieve a decent piezoelectric performance [73].

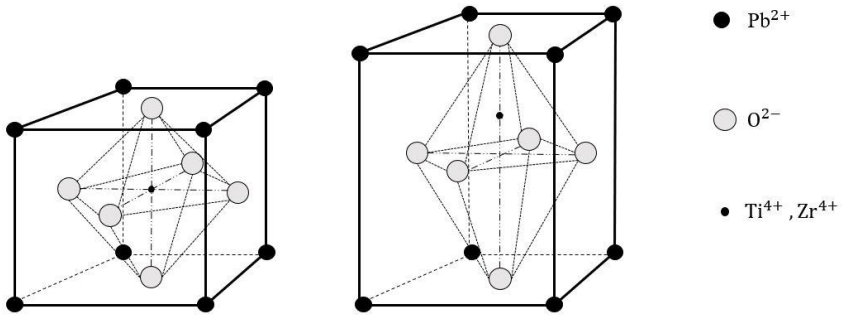

Figure 3.1 The cubic (outside) and tetragonal (inside) structures of the lead zirconate titanate (PZT) crystal.

Macroscopic polarization can be achieved by applying a strong electric field (about 2 KV/mm) to the piezoelectric material. As shown in Figure 3.2(a), the polar domains of the PZT crystal cells are randomly orientated before polarizing. As illustrated in Figure 3.2(b), almost all the polar domains are turned in the same direction after polarization. During the polarization process, PZT material in the orientation of poling field will be permanently extended. The effort of polarization is permanent, only when the temperature of the enviorment is higher than Curie temperature or applying another strong electric field that has the orientation is opposite to the original polar direction.

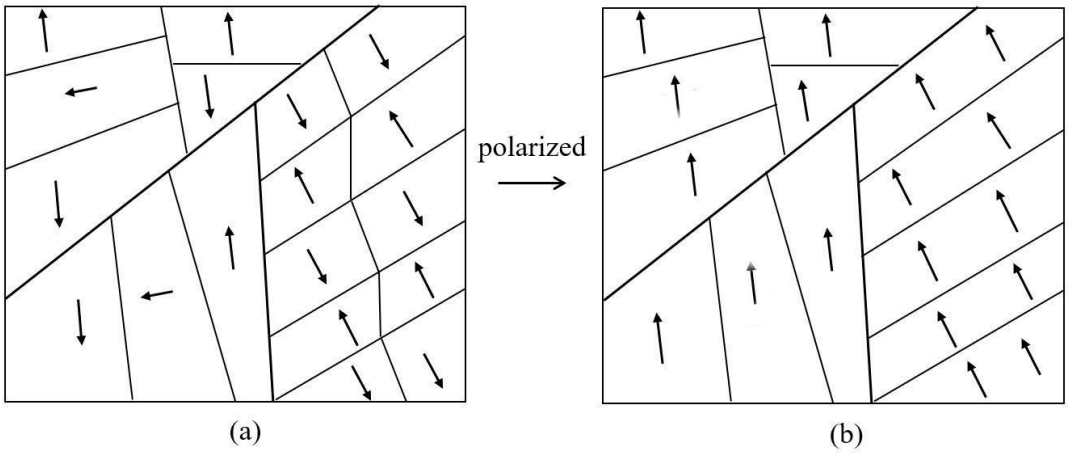

Figure 3.2 (a) The domains of PZT material before polarization; (b) The domains of PZT material after polarization.[2]

Figure 3.3 (a) shows that the PZT bulk would maintain electrical neutrality if there are no forces exert on it. As shown in Figure 3.3 (b), when a tension force is exerted on the polar axis, the crystal will create an electric field E that opposites to the original polar direction, and tends to compress the bulk against the applied tension force. Similarly, as demonstrated in Figure 3.3 (c), when the material is being compressed, the electric field will be generated against the compression, and the orientation of it is parallel to the polar direction.

[2] https://piezo.com/pages/piezoelectric-transducers-abstract

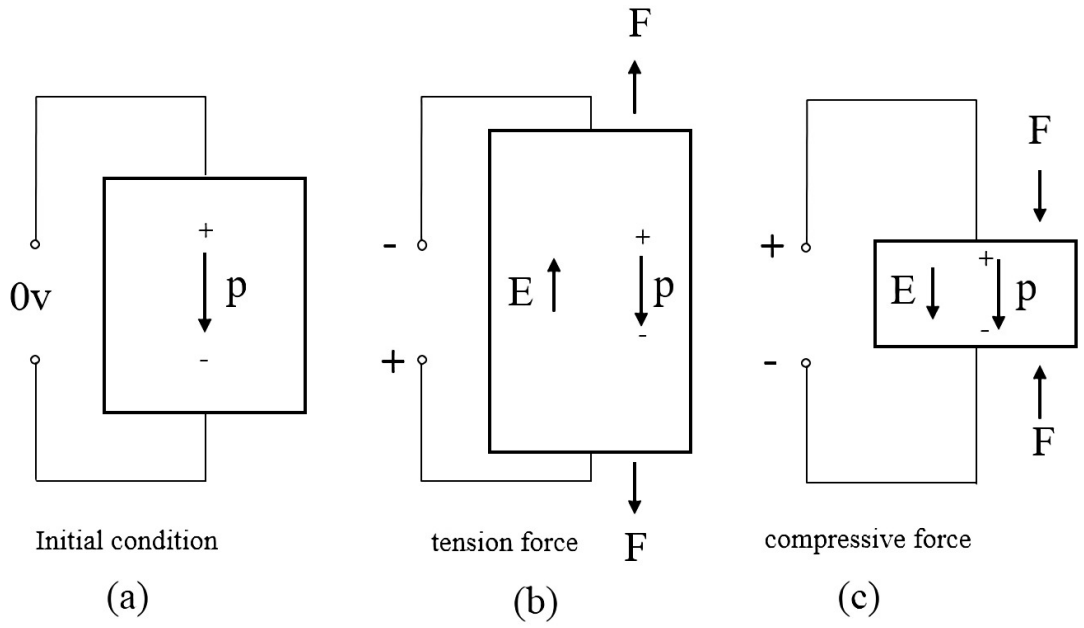

Figure 3.3 Electric fields caused by different types of physical deformation: (a) unloaded; (b) loaded by tension force; (c) loaded by compressive force.

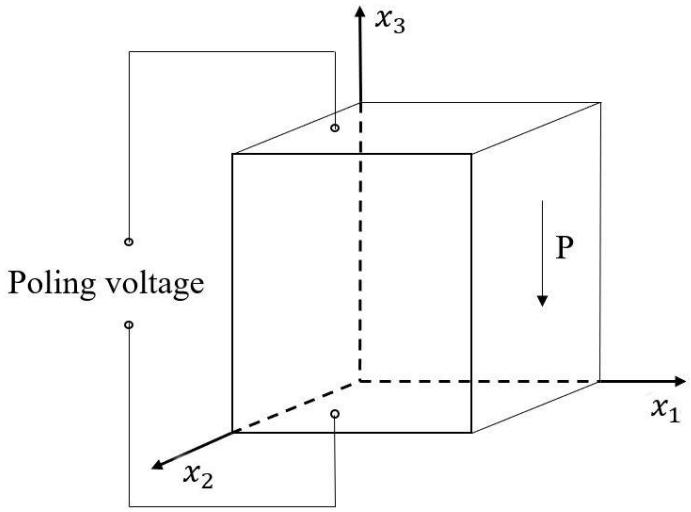

Figure 3.4 Three axes of a rectangular piezoceramic bulk.[3]

[3] https://piezo.com/pages/piezoelectric-transducers-abstract

As shown in Figure 3.4, three axes are used to define the piezoceramic material: x_3 is aligned along the polar axis, x_1 and x_2 are called the transverse axis. This coordinate system will facilitate the analysis process of the electrical and mechanical behaviours of the PZT ceramic material.

There are two main operation modes of the piezoelectric energy harvester: the d_{33} mode and the d_{31} mode. The difference between them is the directions of the poling field and the applied force. In the d_{33} mode, the direction of the applied force is parallel to the polarization direction, while in the d_{31} mode, they are perpendicular to each other. Figure 3.3 shows the case of the d_{33} mode. Figure 3.5 shows a bending beam structure energy harvester works in the d_{31} operation mode. As shown in Figure 3.5 (b), the PZT material is fixed on the substrate structure, and the output voltage is zero when there is no deformation of it. When the beam is subjected to an upward bending, which has shown in Figure 3.5 (a), the direction of the generated electric field will opposite to the poling field due to the PZT layer being compressed alone the x_1 axis. Similarly, when the beam is subjected to a downward bending, as illustrated in Figure 3.5 (c), the generated electric field and the poling field will have the same direction due to the PZT layer being stretched along the x_1 axis.

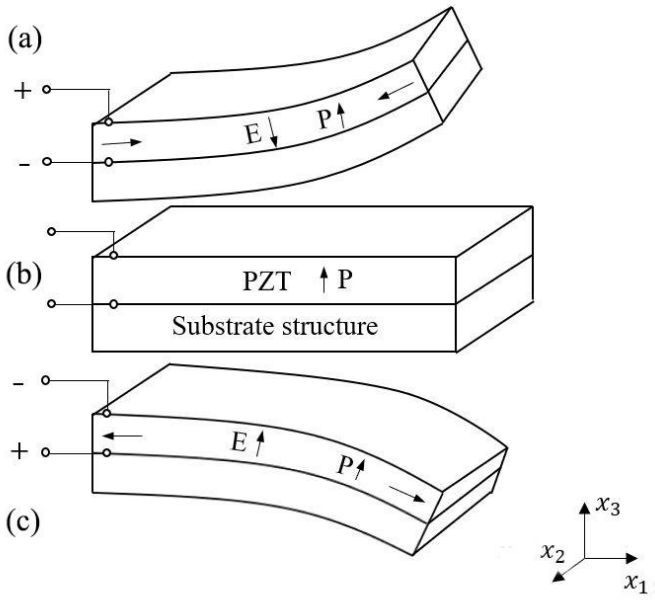

Figure 3.5 Piezoelectric energy harvester operates in the d_{31} mode: (a) upward bending situation; (b) unloaded situation; (c) downward bending situation.

3.2 Modeling of the Cantilevered Piezoelectric Energy Harvester

In this section, the dynamic model of the uni-morph cantilevered piezoelectric energy harvester will be developed.

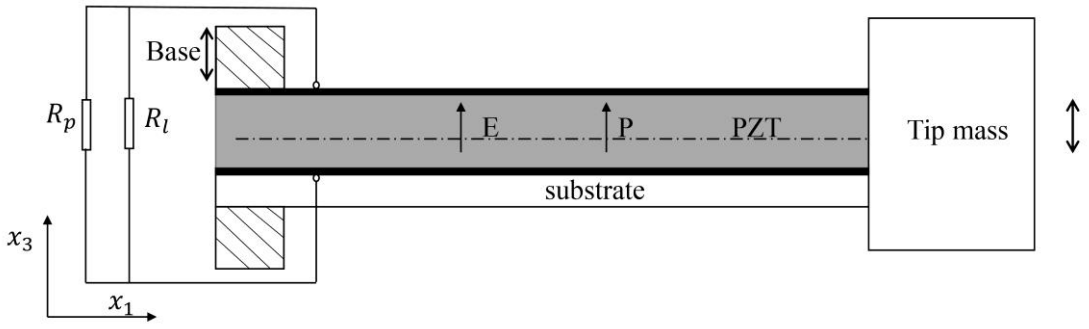

Figure 3.6 1-D model of the uni-morph cantilevered piezoelectric energy harvester.

As shown in Figure 3.6, a 1-D piezoelectric energy harvester is subjected to a base vibration, where R_l and R_p in the circuit are load resistance and leakage resistance, respectively. The electrodes in the figure are illustrated by two black rectangular, and the thickness of it can be neglected in this circumstance.

The analytical model of the cantilevered piezoelectric energy harvester can be derived by using the energy method. Based on the Hamilton principle, the variational indicator (*VI*) should always be zero through the Lagrange function [74]:

$$VI = \int_{t_1}^{t_2} \left[\delta \left(T_k - U \right) + \delta W \right] dt = 0 \tag{3.1}$$

where T_k is the system's kinetic energy, U is the potential energy of the system, and W is the external work done on the system by the base excitation. Basically, there are two things that really matter in energy harvesting: the input force and output electricity, and the relationship of them could be obtained by the following constitutive equation [75]:

$$\begin{bmatrix} \boldsymbol{S} \\ \boldsymbol{D} \end{bmatrix} = \begin{bmatrix} c^E & -e^t \\ e & \varepsilon^S \end{bmatrix} \begin{bmatrix} \boldsymbol{T} \\ \boldsymbol{E} \end{bmatrix} \tag{3.2}$$

where $\boldsymbol{T}$, $\boldsymbol{D}$, $\boldsymbol{S}$, $\boldsymbol{E}$ represent the matrix of stress, charge density, strain and electric field, respectively, c^E is the compliance of the material under an electric field, ε^S signifies the permittivity of the material, and e is the piezoelectric constant, which represents the relationship between the strain and charge density. Since the cantilevered piezoelectric energy harvester operates at mode d_{31}, Then Eq. (3.2) can be expanded into two equations that are shown as below:

$$T_1 = c^E S_1 - e_{31} E_3 \tag{3.3}$$

$$D_3 = e_{31} S_1 + \varepsilon^S E_3. \tag{3.4}$$

It is helpful to point out that the subscript 1 indicates that the direction of T and S is parallel to the x_1 axis and the subscript 3 indicates that the direction of D and E is along the x_3 axis. Thus the constant e_{31} indicates that the direction of the charge movement is

parallel to the x_3 axis and the direction of generated stress is along the x_1 axis [76]. In addition, since the constant e_{31} is unavailable sometimes, it also can be expressed by a more commonly used constant d_{31} as [77]:

$$e_{31} = d_{31} c^E \tag{3.5}$$

According to the Euler-Bernoulli beam theory and the Rayleigh-Ritz method [78], the dynamic model of the linear energy harvester (LEH) can be obtained. And it also can be considered as an equation of motion for a mechanical dynamic equation of a 1-D spring-mass system that can be rewritten as [69], [79], [80]:

$$m\ddot{z} + c\dot{z} + kz + \theta v = -m\ddot{w}_b \tag{3.6}$$

$$\frac{v}{R_l} + C_p \dot{v} - \theta \dot{z} = 0 \tag{3.7}$$

where m, c, k are the equivalent mass, equivalent damping coefficient and equivalent stiffness, respectively, θ is the equivalent electromechanical coupling coefficient, z and w_b are the tip displacement relative to the base and the base displacement, respectively, R_l is the load resistance, and C_P is the capacitance of the piezoelectric element which has the value of 100×10^{-9} F obtained from the datasheet of the piezoelectric bending transducer (MIDE S128-J1FR-1808YB) that is used in this study.

3.3 Identification of the System Parameters of the LEH

3.3.1 Damping Coefficient Identification

Eq. (3.6) and Eq. (3.7) describe the dynamic model of an LEH system. As shown in Eq. (3.6), c is the equivalent damping coefficient which can be calculated by the following equation:

$$c = 2\zeta\omega_n m, \tag{3.8}$$

where ω_n=2π(3.8)=23.88 rad/s is the natural frequency of the system, and ζ is the

damping ratio that can be experimentally determined by using the logarithmic decrement method [81]. By measuring the free response of the system and capturing all the peak values, the damping ratio can be obtained as follows:

$$\delta = \frac{1}{n} \ln\left(\frac{x(t)}{x(t+nT)}\right) \tag{3.9}$$

$$\zeta = \frac{\delta}{\sqrt{4\pi^2 + \delta^2}} \tag{3.10}$$

where $x(t)$ is the first peak value of the free response, and $x(t+nT)$ is the peak value after n successive periods. As shown in Figure 3.7, a typical free response of the system is obtained experimentally, and the peak values have been marked with a series of red circles. After the damping ratio has been calculated, the damping coefficient can be derived from Eq. (3.8) and listed in Table 3.1.

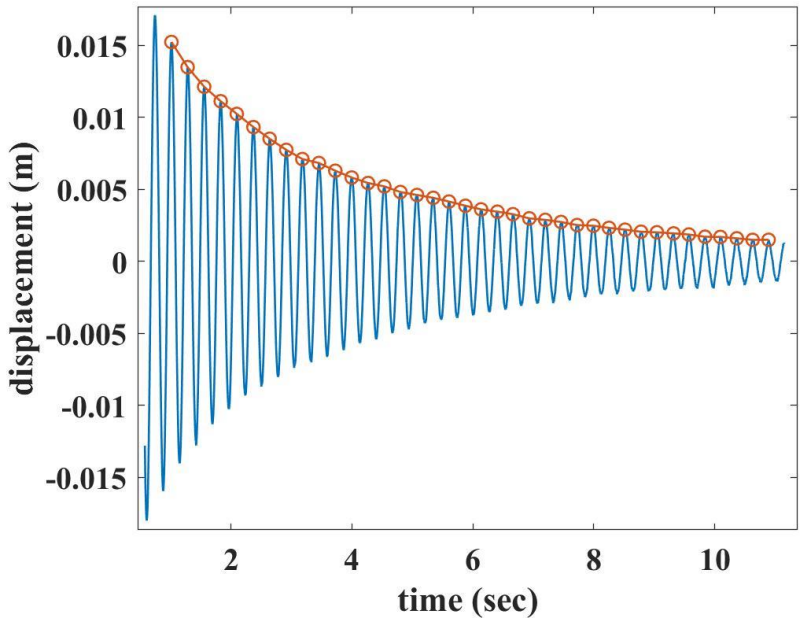

Figure 3.7 Free response of the LEH (blue line). And the peak values of the free-response (red circle).

3.3.2 Identification of the Electromechanical Coefficient

The electromechanical coefficient θ can be determined experimentally. The open-circuit voltage of the LEH and the relative beam's tip displacement data are measured to calculate the approximate value of θ. As shown in Eq. (3.7), the term of v/R_l can be eliminated when the circuit is open or $R_l = \infty$. Then, Eq. (3.7) becomes:

$$\dot{v} = \frac{\theta}{C_p}\dot{z} \tag{3.11}$$

Take the integral for both sides, and it will become:

$$v = \frac{\theta}{C_p}z + C \tag{3.12}$$

where C is zero if the hysteresis is neglected. As shown in Figure 3.8, the blue ellipses represent the measured open-circuit voltage data verse displacement of the tip mass, and the red line is the result that fits the measured voltage data using the first-order polynomial, which gives $\theta/C_p = 1.88\times10^{3}$. Since the value of C_P is already known as 100×10^{-9} F then θ can be obtained as 1.88×10^{-4} N/V. Table 3.1 summarizes all the values of parameters.

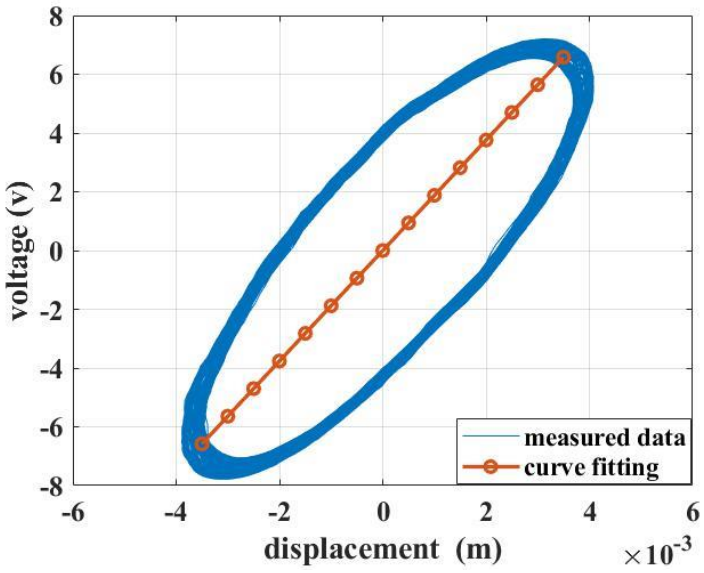

Figure 3.8 Piezoelectric energy harvester voltage output vs relative beam displacement.

Table 3.1 Parameters of the energy harvester system.

Symbol	Parameters	
	Name	Value
m (kg)	Equivalent mass of the system	0.086
c (Ns/m)	Damping coefficient	0.0668
k (N/m)	Stiffness coefficient	47.39
θ (N/V)	Electromechanical Coefficient	1.88×10^{-4}
C_P (F)	Capacitance of the piezoelectric beam	100×10^{-9}

3.4 Experimental Validation

Since the electromechanical model of the energy harvest system has been developed, a simulation for the voltage response under the harmonic excitation can be performed using the MATLAB software to validate the accuracy of the model. The acceleration of the harmonic base motion is chosen as:

$$\ddot{w}_b = A\sin\left(2\pi f\right)t \tag{3.13}$$

where A is the amplitude of the acceleration which is chosen to be 0.068 m/s^2, f is the exciting frequency that varies from 3 Hz to 5 Hz. In the simulation, the frequency is increased by 0.2 Hz each iteration. By solving Eq. (3.6) and Eq. (3.7) with zero initial conditions using the MATLAB ODE45 solver, the relative displacement and the open-circuit voltage response can be obtained. For the sake of comparison, the root-mean-square (RMS) value is used to represent the overall value of a set of voltage signals.

The experiment platform is the same one that was mentioned in Section 2.2.2. The input voltage signals sent to the shaker amplifier has the form of:

$$v_e = V_e\sin(2\pi f)t \tag{3.14}$$

where V_e is the amplitude of the input voltage. In order to maintain the constant acceleration of A=0.068 m/s^2, an experiment is conducted to determine V_e for each of the exciting frequencies, and Table 3.2 lists all the results. To capture the open-circuit voltage, the DS1104 data acquisition board's input terminals are connected directly to the leads of the piezoelectric energy harvester.

Table 3.2 Amplitude of the input voltage signal for experimental validation.

f (Hz)	3	3.2	3.4	3.6	3.65	3.7	3.72	3.75	3.77
V_e (V)	0.146	0.128	0.114	0.101	0.098	0.095	0.094	0.093	0.092
f (Hz)	3.8	3.9	4	4.2	4.4	4.6	4.8	5	
V_e (V)	0.091	0.086	0.082	0.074	0.067	0.062	0.056	0.052	

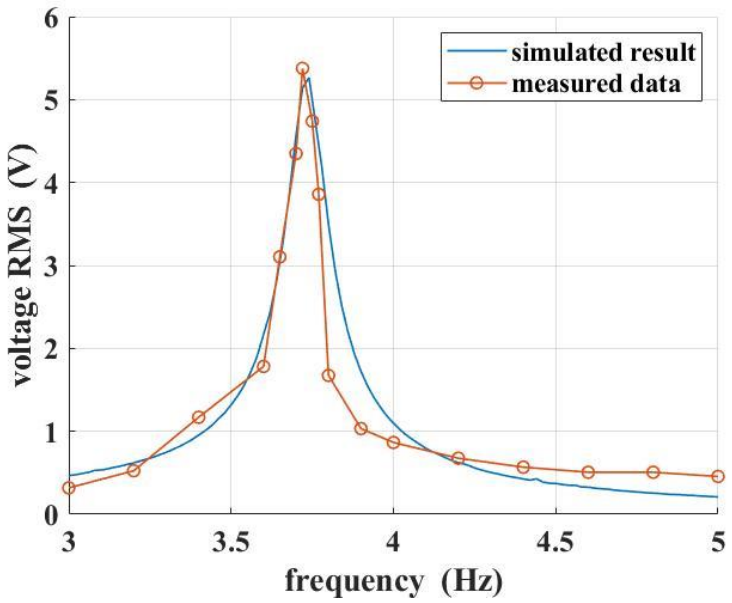

Figure 3.9 Voltage responses of the LEH under the different harmonic excitations: simulation results (blue solid line); measured data (red circles).

As shown in Figure 3.9, both the simulation voltage and the measured voltage reach the peak value at 3.75 Hz because of the resonance phenomenon. And the simulation results

based on the electromechanical model are in a good agreement with the experimental results.

To sum up, the comparison of the simulation results and the measured voltage of the LEH responses to a low amplitude base motion verifies that the electromechanical model is accurate. However, instead of the voltage value, the output power P is the common term used to estimate the efficiency of the system. It has the form of:

$$P = \frac{V_{RMS}^2}{R_l} \tag{3.15}$$

In order to maximize the power output, the optimum resistance should be obtained at first. In the next section, the system's optimum resistance under the harmonic excitation and colored noise excitation will be determined.

3.5 Optimum Resistance for the LEH

3.5.1 Optimum Resistance of the LEH under Harmonic Excitation

The analytical method can be used to define the optimum resistance of an LEH under harmonic excitation. By applying the Fourier transform to Eq. (3.6) and Eq. (3.7), the motion equations can be rewritten in the frequency domain:

$$-m\omega^2 Z(\omega) + j\omega c Z(\omega) + kZ(\omega) + \theta V(\omega) = m^2 \omega W_b(\omega) \tag{3.16}$$

$$\frac{V(\omega)}{R_l} + C_p j\omega Z(\omega) - \theta j\omega Z(\omega) = 0 \tag{3.17}$$

where ω is the angular exciting frequency and j is the imaginary number which equals to $\sqrt{-1}$. And based on Eq. (3.17), the expression of $V(\omega)$ can be found as:

$$V(\omega) = \frac{\theta Z(\omega) j\omega}{C_p j\omega + \frac{1}{R_l}} \tag{3.18}$$

Substituting Eq. (3.18) to Eq. (3.16) yields:

$$Z(\omega)=\frac{-m\omega^2 W_b(\omega)}{\left(k-m\omega^2\right)+\left(c+\dfrac{\theta^2}{cC_P j\omega+\dfrac{1}{R_l}}\right)j\omega} \tag{3.19}$$

Then substituting Eq. (3.19) into Eq. (3.18), the expression of the voltage can be obtained. Hence the expression of the maximum output power is given by

$$\begin{aligned} p &= \frac{V_{rms}^2}{R_l}=\frac{V(\omega)^2}{2R_l} \\ &= \frac{m^2\theta^2\omega^6 W_b^2(\omega)}{2R_l\left[\left(\dfrac{k-m\omega^2}{R_l}-\left(cC_P\omega^2\right)\right)^2+\left(kC_P-mC_P\omega^2+\theta^2+\dfrac{c}{R_l}\right)^2\omega^2\right]} \end{aligned} \tag{3.20}$$

where $V(\omega)$ is the amplitude of the steady-state response of load voltage signal which respects to a specific excitation frequency. It should be noticed that the RMS value of a sinusoidal voltage signal is $1/\sqrt{2}$ of the peak value. To maximize the output power, the denominator of Eq. (3.20) should assume the minimum. Let the denominator part be a function g:

$$g(R_l)=R_l\left[\left(\frac{k-m\omega^2}{R_l}-\left(cC_P\omega^2\right)\right)^2+\left(kC_P-mC_P\omega^2+\theta^2+\frac{c}{R_l}\right)^2\omega^2\right] \tag{3.21}$$

To minimize the function $g(R_l)$, let the derivative of $g(R_l)$ with respect to R_l be zero:

$$\frac{dg(R_l)}{dR_l}=0 \tag{3.22}$$

Then the optimum resistance can be found as:

$$R_{opt}=\sqrt{\frac{\left(k-m\omega^2\right)^2+\omega^2c^2}{\omega^2\left[\left(kC_P-m\omega^2C_P+\theta^2\right)^2+c^2{C_P}^2\omega^2\right]}} \tag{3.23}$$

Because the electromechanical coefficient θ is relatively small, hence it can be neglected. Hence, Eq. (3.23) can be simplified as:

$$R'_{opt} = \frac{1}{\omega C_P} \tag{3.24}$$

On the other hand, based on the impedance matching principle[82], an energy harvesting system will output the maximum power when the load resistance equals to the internal impedance of the energy harvester. Since the piezoelectric element can be seen as a pure capacitor in the energy harvesting system, the value of the equivalent capacitive impedance X_C can be expressed as:

$$X_C = \frac{1}{\omega C_P} \tag{3.25}$$

which has the same form as the simplified optimum resistance as shown in Eq. (3.24). The analytical results of the optimum resistance of the LEH under the 4 Hz, 5 Hz, and 6 Hz harmonic excitations given by Eq. (3.24) and the corresponding maximum output powers by using Eq. (3.20) are listed in Table 3.2. To verify those analytical results, a series of simulations and experiments have been conducted.

In the simulation, The load resistance varies from 10 KΩ to 1 MΩ, in an increment of 50 KΩ. The acceleration of input signal has the form as Eq. (3.13), to ensure the voltage can reach a sufficient value when the load resistance is small, the amplitude of acceleration A is chosen to be 0.75 m/s^2, f is the frequency of the base excitations which are set to be 4 Hz, 5 Hz, and 6 Hz, respectively. By solving Eq. (3.6) and Eq. (3.7) with the zero initial conditions in the period of T=60 s using the MATLAB ODE45 solver, the steady-state responses of the relative displacements and load voltages can be obtained. Based on the RMS values of the voltage signals, the output powers can be calculated by using Eq. (3.15).

In addition, for the sake of comparison, the experimental validations are conducted as well. The input voltage signals have the same form as shown in Eq. (3.14). To maintain the amplitude of acceleration of the excitation A=0.75 m/s^2, the amplitude of the input voltage signal V_e has been chosen as 0.916 V, 0.610 V, and 0.381 V for 4 Hz, 5 Hz and 6 Hz harmonic excitations, respectively. Base on the RMS values of the response voltage signals, the output power under the specific excitation frequency and load resistance can be derived by using Eq. (3.15).

The results of the simulations and experiments under the 4 Hz, 5 Hz and 6 Hz harmonic excitations are shown in Figure 3.10 (a), (b) and (c). The optimum resistance values obtained by the analytical method, the simulation method and the experiment method are listed in Table 3.3. the peak values of output powers under different frequency harmonic excitations are also listed.

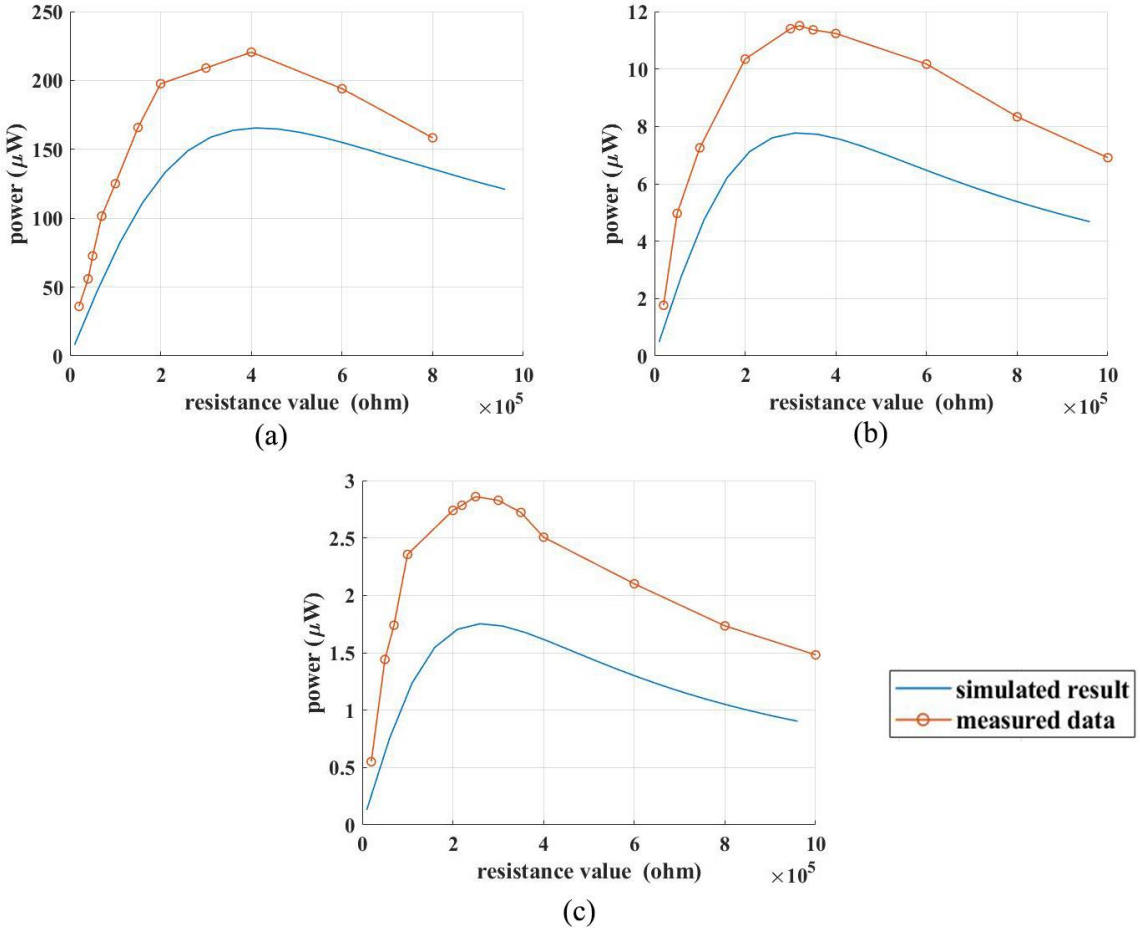

Figure 3.10 Relationships between the output powers and load resistances under different frequency harmonic excitations: (a) under the excitation of 4 Hz; (b) under the excitation of 5 Hz; (c) under the excitation of 6 Hz.

Table 3.3 Optimum resistances under different frequency harmonic excitations obtained by various methods.

	Analytical result		Simulation result		Experimental result	
	R_{opt} (KΩ)	P_{max} (μW)	R_{opt} (KΩ)	P_{max} (μW)	R_{opt} (KΩ)	P_{max} (μW)
4 Hz	397	174.56	410	165.6	400	220.6
5 Hz	318	8.97	310	8.86	320	11.51
6 Hz	265	2.21	260	2.12	250	2.86

As shown in Table 3.3, there is only a small difference between the values of R_{opt} derived from the analytical method, those from simulations and those from the experiments. For instance, Under the 4 Hz harmonic excitation, the simulation and experimental results have a 3.2% and 0.7% difference from the analytical result, respectively. For the 5 Hz excitation, the simulation result is lower than the analytical result with a 2.5% deviation, and the experimental result is 0.6% higher than the analytical result. And for the 6 Hz case, the differences are 1.8% and 5.6%, respectively.

Besides, it also could be found in Table 3.3 that the discrepancy between the maximum output powers P_{max} obtained from the analytical method and simulations are fairly small. And the differences between the analytical results and experimental results are 26.3%, 28.3 % and 29.4% under 4 Hz, 5 Hz and 6 Hz harmonic excitations, respectively. And the differences between the simulation results and experimental results are 33.2%, 29.9% and 29.4%, respectively. As the result of the resonance phenomenon, the output power under the 4 Hz excitation is significantly higher than that under the 5 Hz and 6 Hz excitations due to the resonance.

In conclusion, for an LEH, the optimum resistance value will decrease as the excitation frequency increases. And the system will reach the highest output power when the frequency of the harmonic excitation is close to the natural frequency of the system.

3.5.2 Optimum Resistance of LEH under the Colored Noise Excitation.

In general, an energy harvester works in an environment that has random ambient vibration. Hence, a discussion of the LEH under random excitation is necessary. Therefore, a series of simulations have been conducted to investigate the optimum resistance and output performance of the system, and the experimental results have also been presented.

The simulation is based on the electromechanical model given by Eq. (3.6) and Eq. (3.7). The parameters in these equations are listed in Table 3.1. The input signal $\ddot{w}_b(t)$ is the colored noise signal which can be obtained from a white Gaussian noise passing through a 20^{th} order bandpass filter, and the lower and higher cut-off frequency has been chosen as 3 Hz and 20 Hz, respectively. The random excitation can be divided into three different levels: low-level excitation (S =0.205 g), medium-level excitation (S =1.115 g), and high-level excitation (S =1.569 g) where S represents the integral of power spectrum density (PSD) of the colored random acceleration.

According to Eq. (3.24), to define the optimum resistance for an LEH, the dominant frequency of the voltage response should be obtained at first. As mentioned in [83], when an LEH that is subjected to the random excitation, The peak value of the PSD of response voltage corresponds to the system's resonance frequency. It indicates that the dominant frequency of the system's response equals to the resonance frequency. As a verification, three sets of simulations for different levels of random input excitations with zero initial conditions have been conducted. The corresponding output open-circuit voltage and the power spectrum are shown in Figure 3.11.

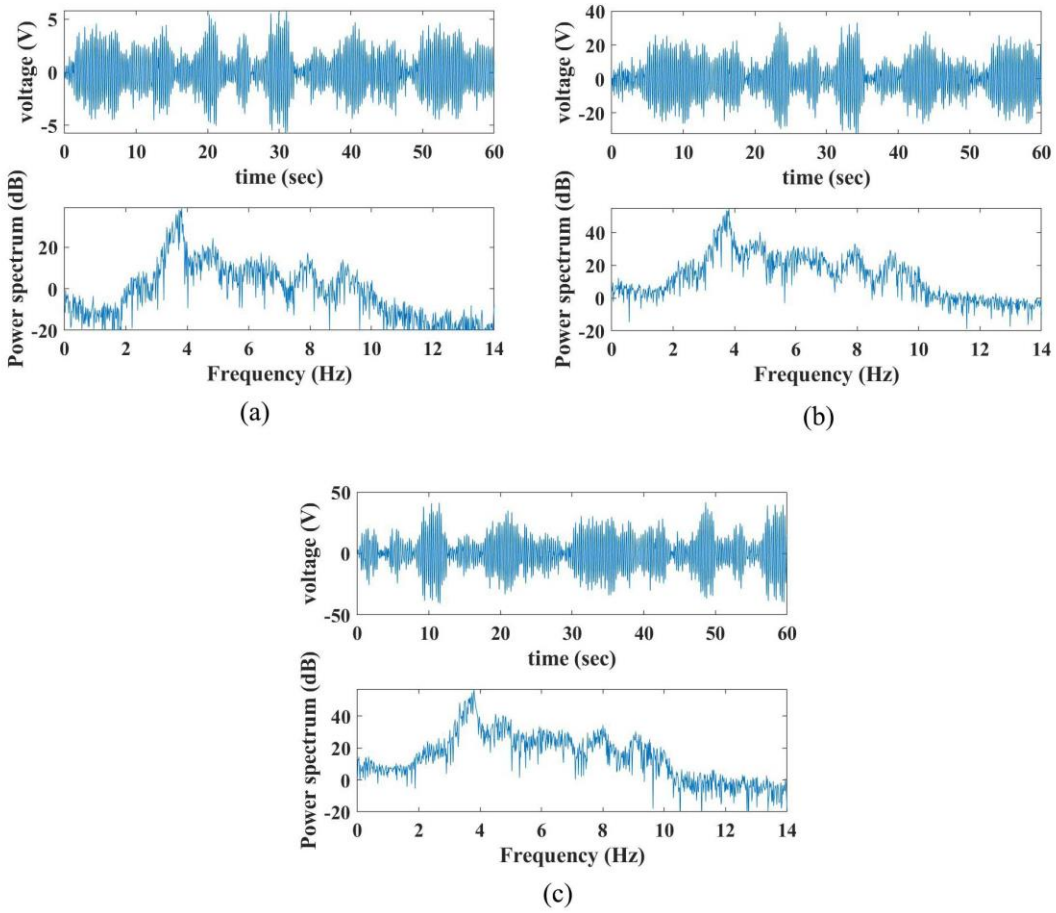

Figure 3.11 The time response and power spectrum of the open-circuit voltage of LEH under the colored noise excitation: (a) the low-level excitation; (b) the medium-level excitation; (c) the high-level excitation.

As shown in the upper plots of Figure 3.11 (a), (b) and (c), the output voltage grows as the excitation level increases. As illustrated in the lower figure of Figures 3.11 (a), (b) and (c), the dominant frequency for all of the three cases is at 3.79 Hz, which is very close to the resonance frequency. Hence, the optimum resistance can be obtained from the numerical method by using Eq. (3.24), which is 419 KΩ.

To investigate the calculated optimum resistance, a series of simulations have been conducted. In the simulation, the load resistance varies from 10 KΩ to 1 MΩ, in an increment of 50 KΩ. By solving Eq. (3.6) and Eq. (3.7) with zero initial conditions using

the MATLAB ODE45 solver, the relative displacements and the load voltage responses can be obtained. And the output powers can be calculated by using Eq. (3.15). In order to reduce the fluctuation of the output power, ten simulations have been conducted for each resistance value, and the average output power has been chosen as the final result. As shown in Figure 3.12 (a), (b) and (c) that give the maximum, average, and minimum values, the values of the optimum resistance are both at 410 KΩ which has a 2.19% difference from the analytical result. And the maximum values of output power are 4.25 μW, 150 μW and 215.12 μW for the low-level, the medium-level, and the high-level random excitations, respectively.

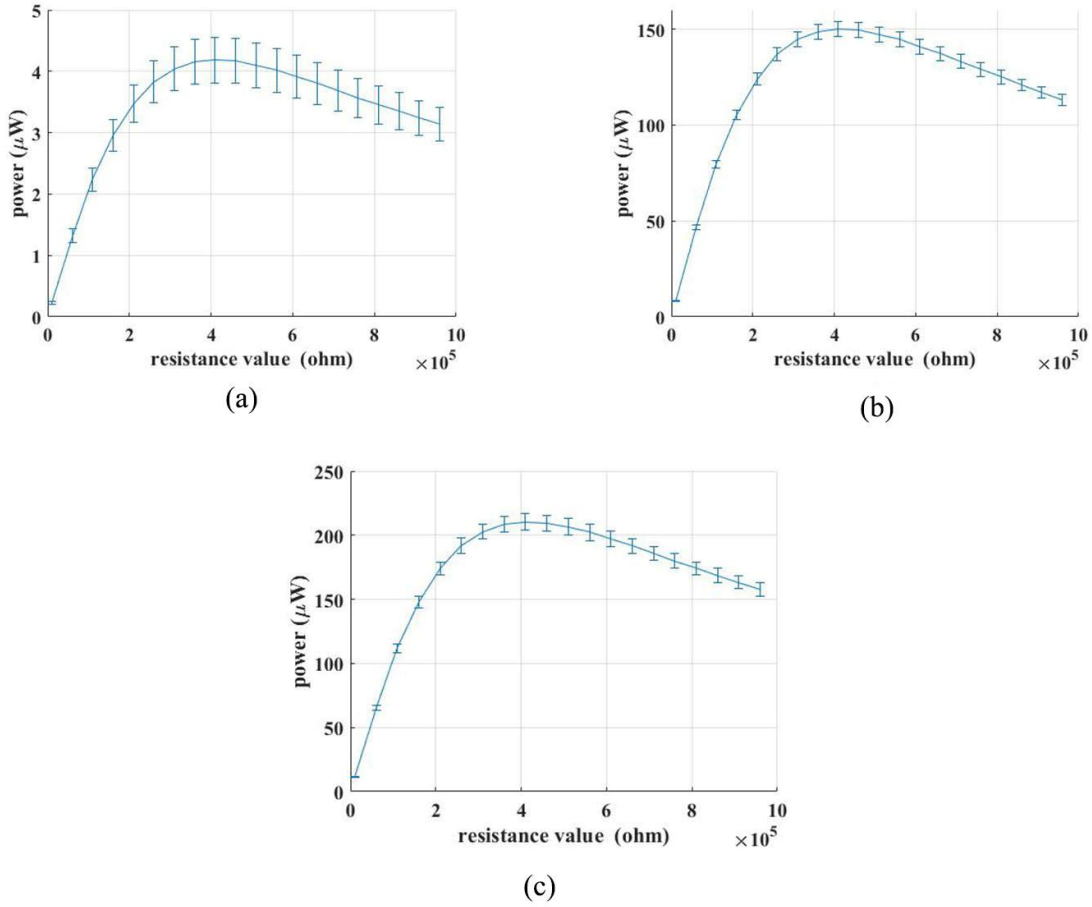

Figure 3.12 Simulation results of the relationship between the output power and load resistance of LEH under the colored noise excitation: (a) the low-level excitation; (b) the medium-level excitation; (c) the high-level excitation.

The experimental validations of LEH subjected to the low-level and medium-level colored noise excitations have also been developed. Considering the high-level excitation may damage the piezoelectric transducer, the experiment of the high-level excitation is not attempted. As shown in Figure 3.13 (a), the optimum resistance is 400 KΩ which has an 4.6% difference with the analytical result. And the maximum output power is 9.1 μW which is slightly higher than the simulation result. As illustrated in Figure 3.12 (b), the optimum resistance for medium-level excitation is 400 KΩ which has a 4.6% difference from the analytical result. And the maximum output power is 205 μW which is higher than the simulation result with 26.8%.

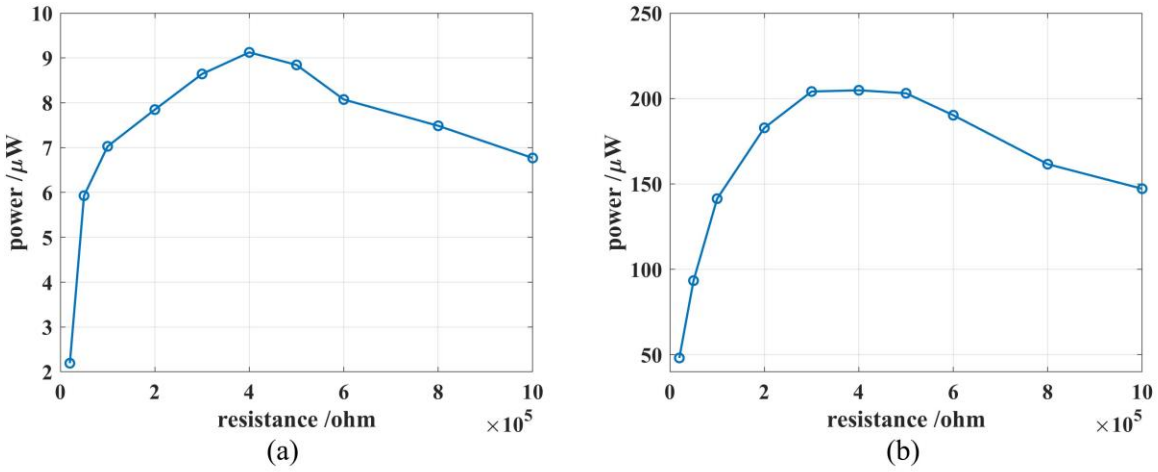

Figure 3.13 Experimental results of the relationship between the output power and the load resistance of LEH under the different random excitation levels: (a) the low-level excitation; (b) the medium-level excitation.

To sum up, the value of the optimum resistance of an LEH depends on the resonance frequency of the system, which indicates that the analytical result based on the harmonic excitation still applies to the situation of the colored noise excitation. Besides, the maximum output power increases when the acceleration level of excitation increases.

3.6 Conclusions

In this chapter, the electromechanical model of the cantilevered piezoelectric energy

harvester is developed. Then the model is approximated as a linear system. The optimum resistances of the LEH under harmonic excitation and colored noise excitation are investigated, respectively. Through a series of numerical simulations and experimental validations, the following conclusions can be derived. The optimum resistance value will decrease as the excitation frequency increases. For the colored noise excitation, the value of the optimum resistance depends on the resonance frequency of the system, which indicates that the analytical result based on the harmonic excitation still applies to the situation of the colored noise excitation. Besides, the maximum output power increases with the acceleration level of excitation increases.

Chapter 4 Bi-stable Energy Harvesters under the Colored Noise Excitation

In principle, the characteristics of a nonlinear piezoelectric energy harvester can enhance the performance of energy harvesting. For instance, a multi-stable cantilevered piezoelectric energy harvester may have two or even more stable equilibrium states, which can efficiently enlarge the displacement of the beam's tip when the beam moves between two wells.

For the developed system, the electromechanical model given in Eq. 3.6 and Eq. 3.7 can be rewritten as follow:

$$m\ddot{z} + c\dot{z} + f_x(z) + \theta v = -m\ddot{w}_b \tag{4.1}$$

$$\frac{v}{R_l} + C_p\dot{v} + -\theta\dot{z} = 0 \tag{4.2}$$

where f_x is the nonlinear restoring force which is related to the relative displacement and defined by the model established in Chapter 2.

This chapter focuses on the performance of the bi-stable energy harvester (BEH). For this purpose, three different strengths of BEHs are considered. As shown in Figure 4.1, the three chosen configurations can make the apparatus exhibit strong, medium and weak bi-stable state behaviors, namely BEH1, BEH2 and BEH3 with the configurations: BEH1 (d=0.0467 m, h=0.0157 m); BEH2 (d=0.0467 m, h=0.0157m); BEH3 (d=0.0407 m, h=0.0177 m). It should be noticed that the potential energy functions in Figure 4.1 have been obtained from the integral of the simulated restoring forces f_x. The potential functions of BEH1, BEH2 and BEH3 have one unstable point which at the middle, and two stable points which are located at: ±0.0273 m, ±0.0252 m and ±0.0226 m, respectively.

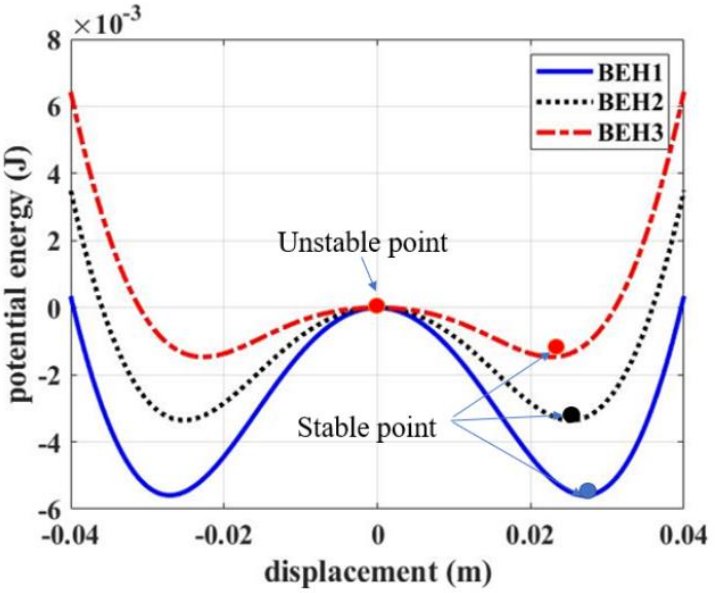

Figure 4.1 Potential energies of three bi-stable energy harvesters: strong (BEH1), medium (BEH2) and weak (BEH3).

In this chapter, the output performance of these three BEHs will be investigated, including the computer simulations and experimental validations of the optimum resistances and the power output performances under three different levels of colored noise excitation. In addition, the output powers of the three BEHs under the increased level of excitation will be compared at the end of the chapter.

4.1 Optimum Resistance of BEHs under the Colored Noise Excitation

4.1.1 Numerical Simulations of the BEHs with an Open-Circuit

Comparing with the LEH system, the optimum resistance of a nonlinear system is not easy to obtain due to the lack of an analytical solution. Alternatively, by analyzing the power spectrum of the output voltage, the approximate value of optimum resistance can be obtained. [14]

The following simulations are based on the electromechanical model given by Eq. (4.1) and Eq. (4.2). The input signal $\ddot{w}_b(t)$ is the colored noise signal which can be obtained by passing a white gaussian noise through a 20th order bandpass filter whose the lower and higher cut-off frequency are chosen as 3 Hz and 20 Hz, respectively. The random excitations can be divided into three different levels: low-level excitation (S =0.205 g), medium-level excitation (S =1.115 g), and high-level excitation (S =1.569 g), where S represents the integral of the power spectrum density (PSD) of the colored noise acceleration. To mimic the open-circuit condition, the load resistance used in simulations is 3MΩ.

As shown in Figure 4.2, BEH1 has two potential wells which locate symmetrically around the origin. The trajectory (a) in Figure 4.2 represents an intra-well oscillation, in which the piezoelectric beam oscillates in one of the potential wells when the random excitation is not strong enough. As demonstrated in Figure 4.3 (a), such an intra-well oscillation exhibits a strong linear behavior.

The paths (b) and (c) in Figure 4.2 illustrate the chaotic inter-well oscillation, in which the BEHs oscillate between the two potential wells, and the time response plots and phase portrait plots are given in Figure 4.3 (b) and (c), respectively. It can be seen that under the middle-level excitation, the beam of the BEH1 oscillates mainly in one of the wells and occasionally jumps to another well, while under the high-level excitation, jumping occurs more frequently, and the oscillation exhibits strongly chaotic behavior.

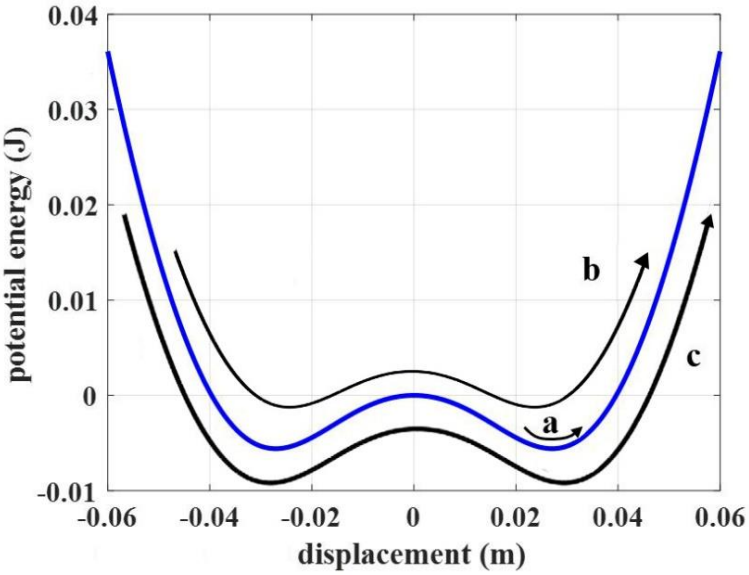

Figure 4.2 Oscillation modes of BEH1 under the three levels of colored noise excitation: (a) intra-well oscillation; (b) weak inter-well oscillation; (c) strong inter-well oscillation.

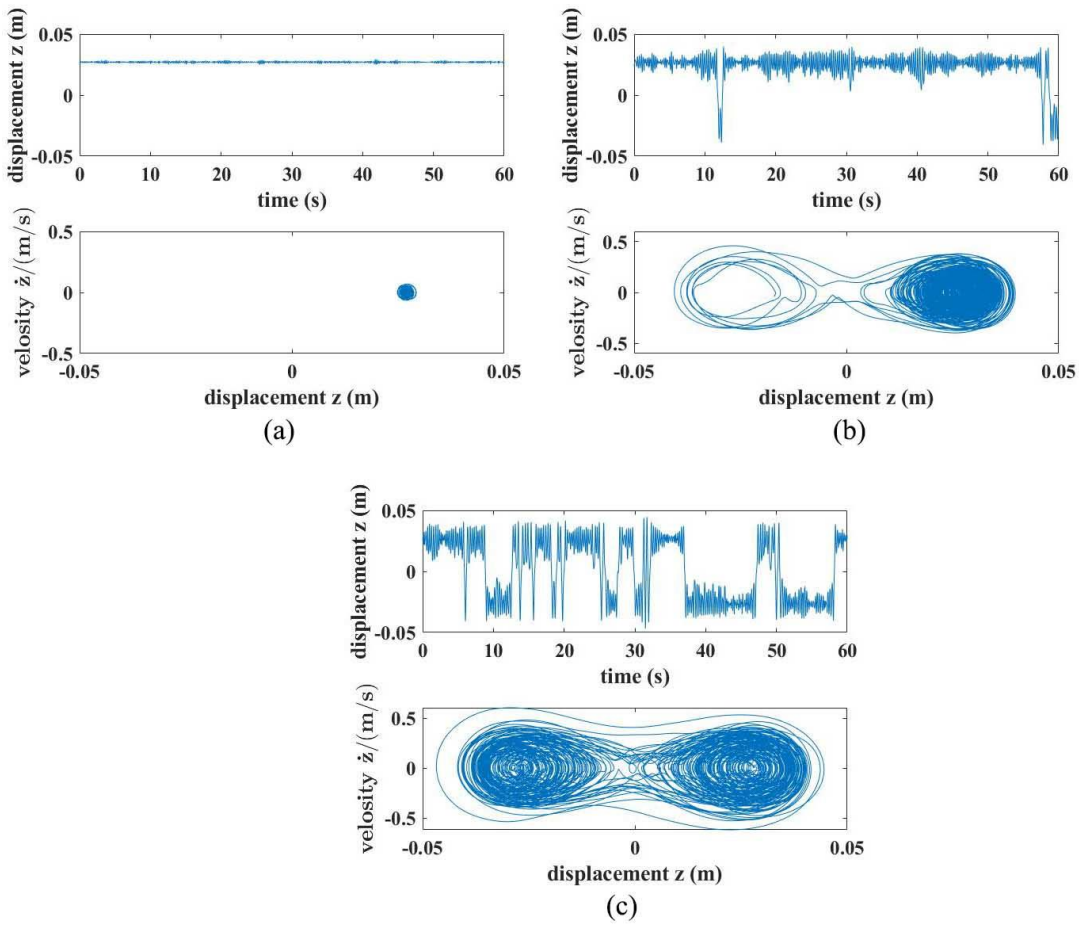

Figure 4.3 The time response (upper plot) and phase portrait (lower plot) of BEH1 under the colored noise excitation: (a) the low-level excitation; (b) the medium-level excitation; (c) the high-level excitation.

The voltage response (upper plot) and the corresponding power spectrum (lower plot) under the low-level excitation are shown in Figure 4.4 (a). It can be seen that the dominant frequency is 4.09 Hz. Then the optimum resistance is found to be 388 KΩ using Eq. (3.24). Under the low-level excitation, the system can only generate a very low amount of voltage (lower than 5 V). As illustrated in Figure 4.4 (b) and (c), When the system operates in the inter-well oscillation, the output voltage can reach about 50 V. It can also be observed that the dominant frequency range shifts to the lower frequencies with an increase of excitation level. It is hard to estimate an optimum resistance value because of the strong nonlinear behavior. If the frequency value corresponding to the power spectrum's peak values are

chosen as the dominant frequencies, namely 3.62 Hz and 3.73 Hz, an estimate optimum resistance value can be obtained. Hence, the calculated values for the optimum resistances are found to be 438 KΩ and 426 KΩ for the system under the middle-level excitation and high-level excitation, respectively. All the calculated optimum resistance values are listed in Table 4.1.

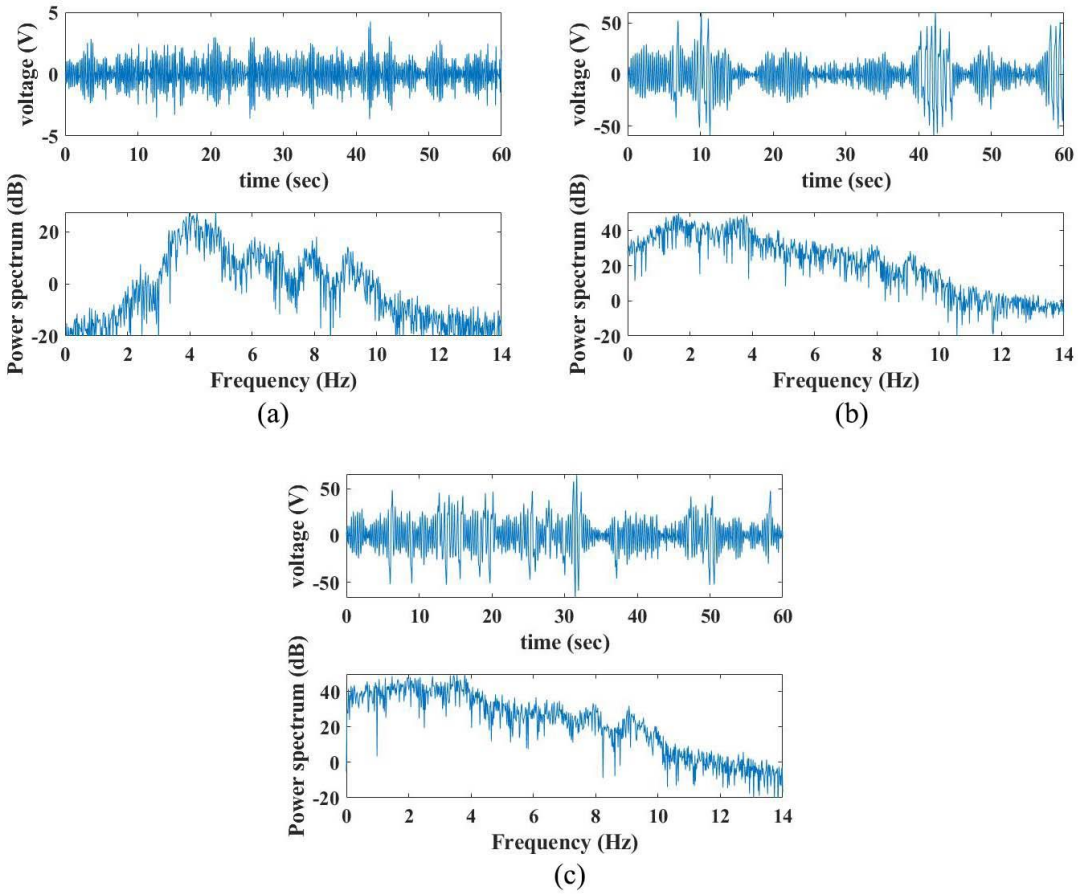

Figure 4.4 The time response and power spectrum of the open-circuit voltage of BEH1 under the colored noise excitation: (a) the low-level excitation; (b) the medium-level excitation; (c) the high-level excitation.

The medium bi-stable energy harvester (BEH2) has two shallower potential wells compared to BEH1, which can benefit the harvesting performance in some ways. As shown in the lower plot of Figure 4.5 (a), the circle of phase portrait is clearly larger than the one shown in Figure 4.3 (a), which means that BEH2 is more sensitive to response to the lower

level excitation than BEH1. In addition, by comparing the upper plot in Figure 4.5 (b) and Figure 4.3 (b), it can be seen that BEH2 oscillates between two potential wells more often than BEH1.

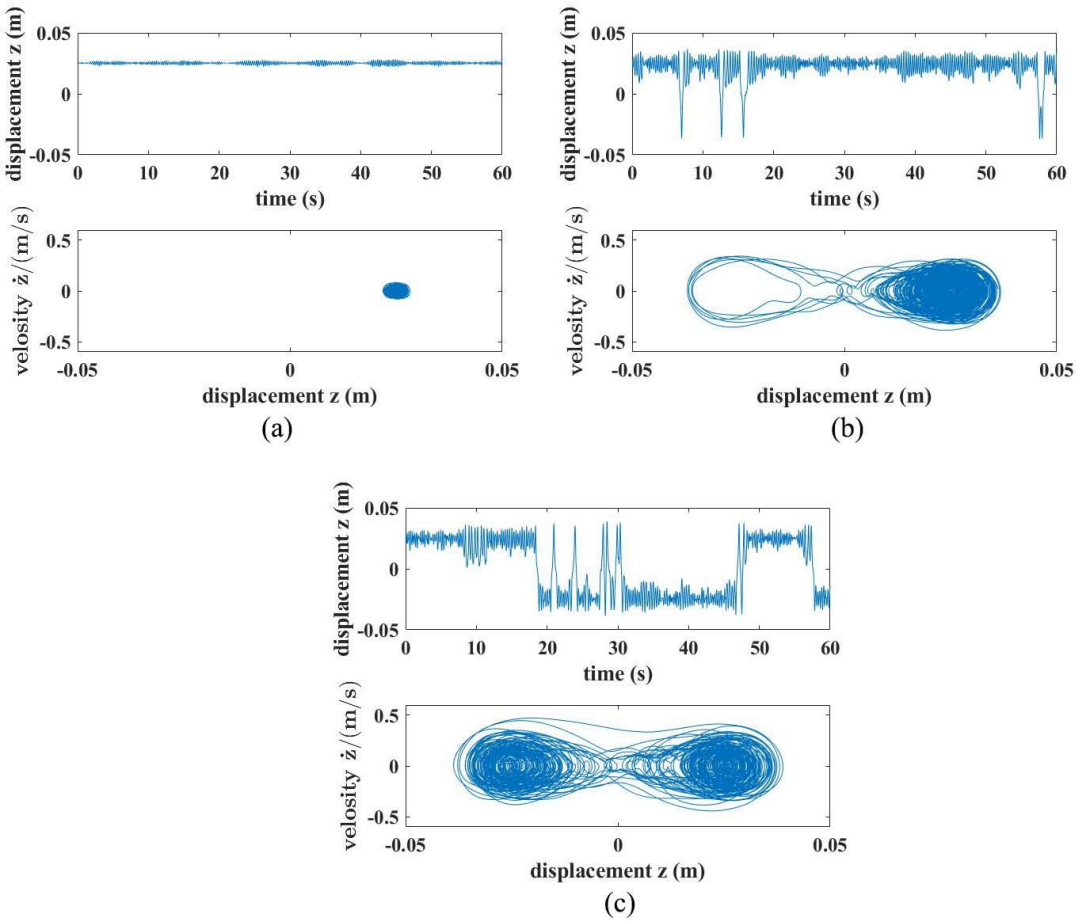

Figure 4.5 The time response (upper plot) and phase portrait (lower plot) of BEH2 under the colored noise excitation: (a) the low-level excitation; (b) the medium-level excitation; (c) the high-level excitation.

The open-circuit voltage response (upper plot) and the corresponding frequency spectrum (lower plot) of BEH2 under the three different levels of excitations are shown in Figure 4.6. The dominant frequencies are 3.62 Hz, 3.43 Hz and 3.21 Hz, respectively. The corresponding optimum resistances can be obtained and are listed in Table 4.2.

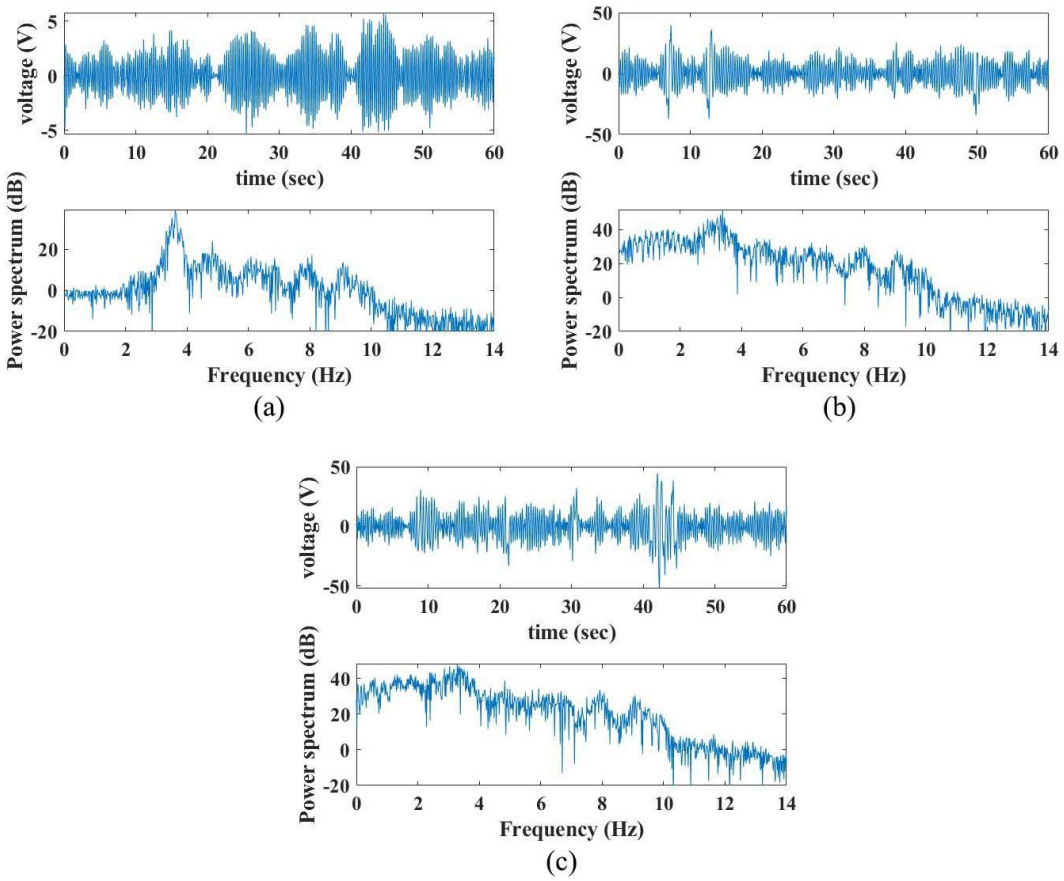

Figure 4.6 The response and power spectrum of the open-circuit voltage of BEH2 under the colored noise excitation: (a) the low-level excitation; (b) the medium-level excitation; (c) the high-level excitation.

The wells of BEH3 or the weak BEH are shallowest among the three chosen bi-stable systems. As demonstrated in Figure 4.7, BEH3 operates in the inter-well oscillation only under the high-level random excitation. It indicates that BEH3 is hard to set into the inter-well oscillation mode. This phenomenon can be explained as follows: In theory, two shallow potential wells have a lower barrier in between, making the system much easier to transfer between the two wells. But the inter-well oscillation of the bi-stable system is a typically hardening-type response [84]. BEH3 has a quasi-zero stiffness factor near the middle position, such softening characteristics constrains the beam to vibrate at one of the wells. Accordingly, BEH3 is hard to set into the inter-well oscillation mode.

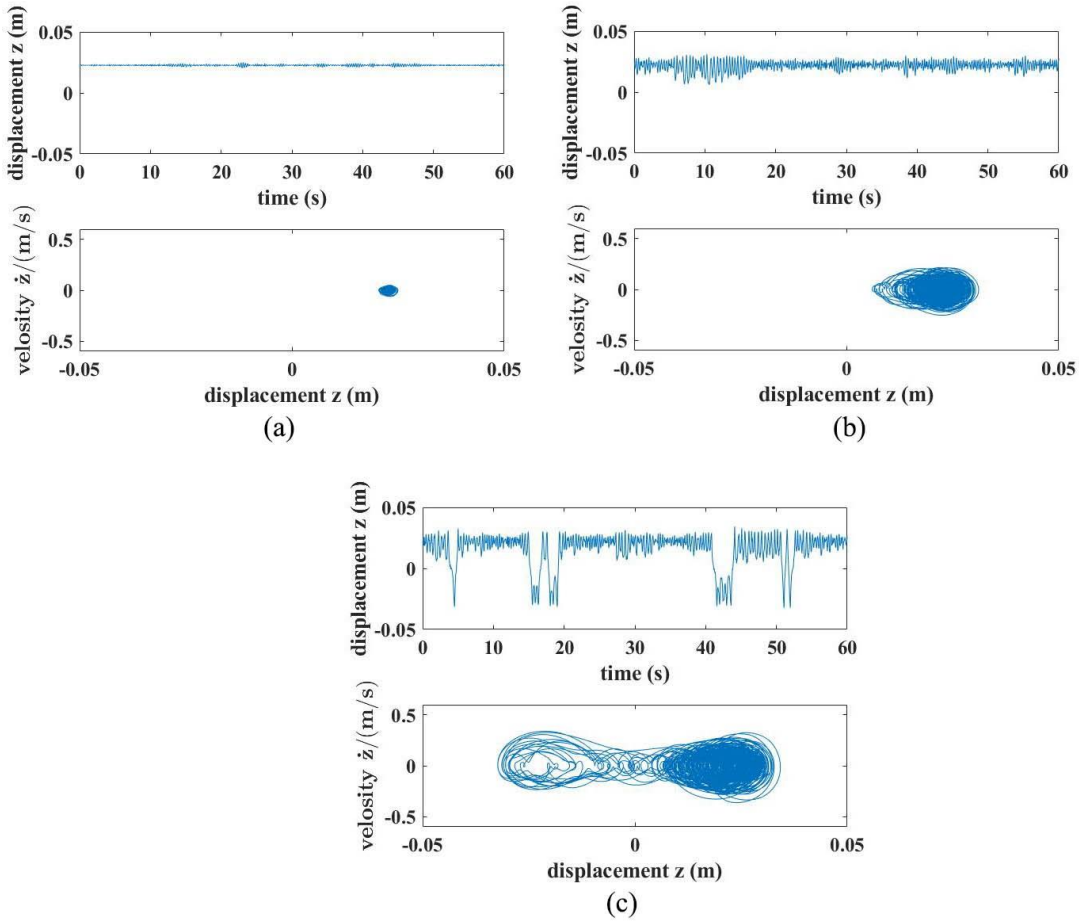

Figure 4.7 The time response (upper plot) and phase portrait (lower plot) of BEH3 under the colored noise excitation: (a) the low-level excitation; (b) the medium-level excitation; (c) the high-level excitation.

The open-circuit voltage response and the corresponding power spectrum of BEH3 under the three different levels of excitations are shown in Figure 4.8. The dominant frequencies can be obtained as 3.02 Hz, 2.68 Hz and 2.67 Hz, and the corresponding optimum resistances are listed in Table 4.3.

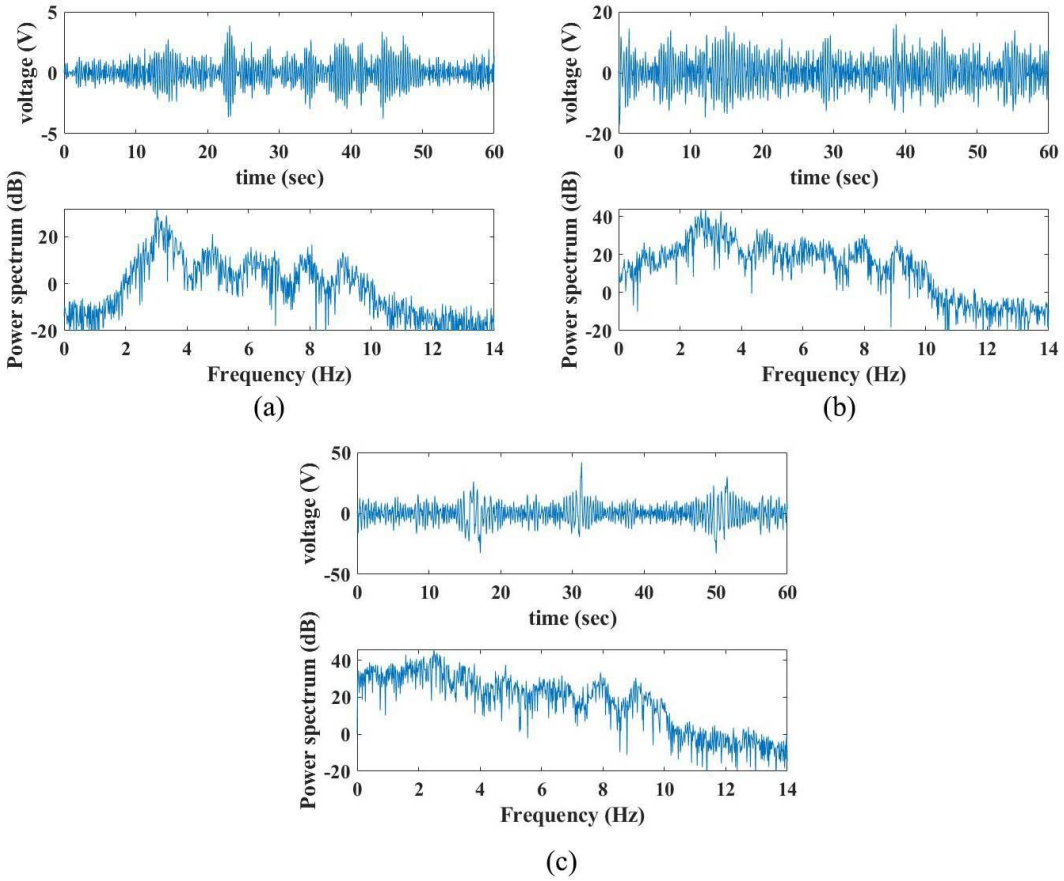

Figure 4.8 The response and power spectrum of the open-circuit voltage of BEH3 under the colored noise excitation: (a) the low-level excitation; (b) the medium-level excitation; (c) the high-level excitation.

4.1.2 Numerical Simulations of BEHs with a Closed-Circuit

For the closed-circuit simulation, the load resistance varies from 10 KΩ to 1 MΩ with an increment of 50KΩ. By solving Eq. (4.1) and Eq. (4.2) with initial displacements at 0.0273 m, 0.0252 m and 0.0226 m in the period of T=60 s using the MATLAB ODE45 solver, the relative displacements and the load voltage responses can be obtained. Based on the RMS value of the voltage response over such a period, the corresponding output power can be calculated.

Because of the nonlinear system's sensitivity and chaotic characteristics under the

random excitation, the voltage response may be different for each simulation. In order to reduce the fluctuation of the output power, ten simulations have been conducted for each of the resistance values. The error bar plot is used to reveal the variation of the responses. The top and bottom of the bar represent the maximum and minimum values of the output powers in the ten simulations, respectively. The line curve of the error bar plot connects the average values for every ten simulations. Based on the average values, the optimum resistances for different levels of excitations and their corresponding maximum output powers can be obtained. As shown in Figure 4.9 (a), the smooth curve represents that BEH1 operates in the intra-well oscillation. As shown in Figure 4.9 (b) and (c), the curves for BEH2 and BEH3 have some fluctuations, indicating that the system enters the inter-well oscillation mode. It can be obtained from Figure 4.9 (a), (b) and (c) that the optimum resistance values are 360 KΩ, 360 KΩ and 500 KΩ, respectively. The optimum resistances and corresponding maximum output powers under the different excitations are listed in Table 4.1.

In addition, as illustrated in Figure 4.10 (a), (b) and (c), the optimum resistances for BEH2 are 410 KΩ, 560 KΩ and 460 KΩ, respectively. For BEH3, it can be observed from Figure 4.11 (a), (b) and (c) that the optimum resistances are 510 KΩ, 510 KΩ and 560 KΩ, respectively. The optimum resistances and corresponding maximum output powers under the different excitations for BEH2 and BEH3 are listed in Table 4.2 and Table 4.3, respectively.

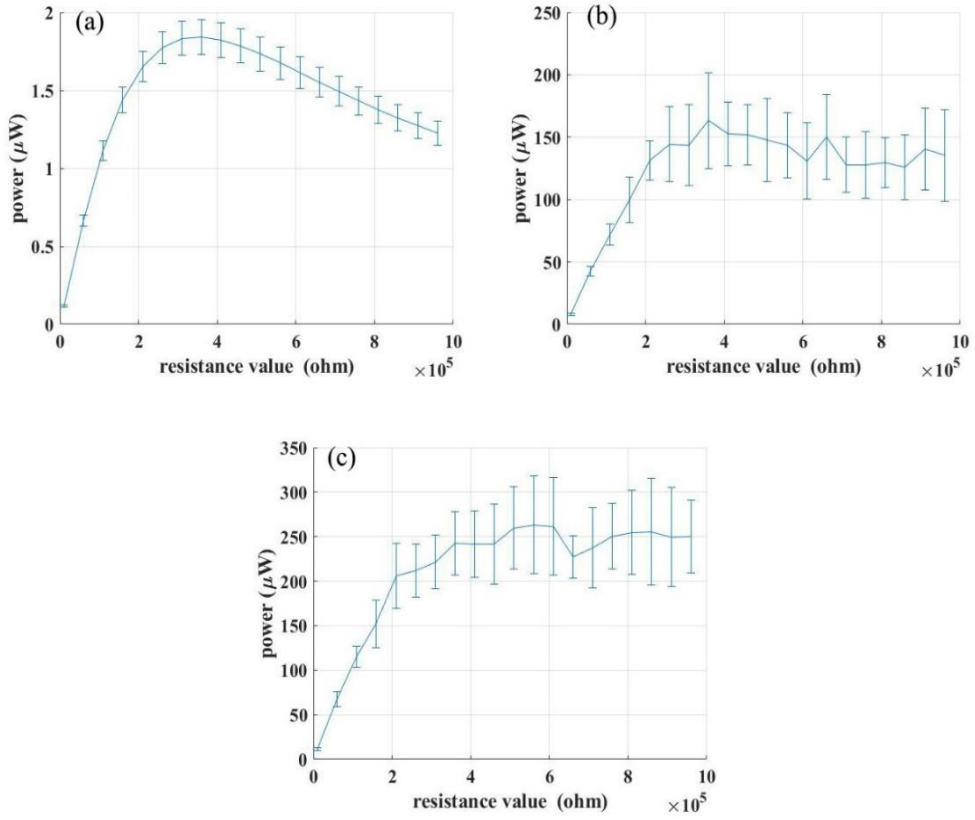

Figure 4.9 Simulation results of the relationship between the output power and load resistance of BEH1 under the colored noise excitation: (a) the low-level excitation; (b) the medium-level excitation; (c) the high-level excitation.

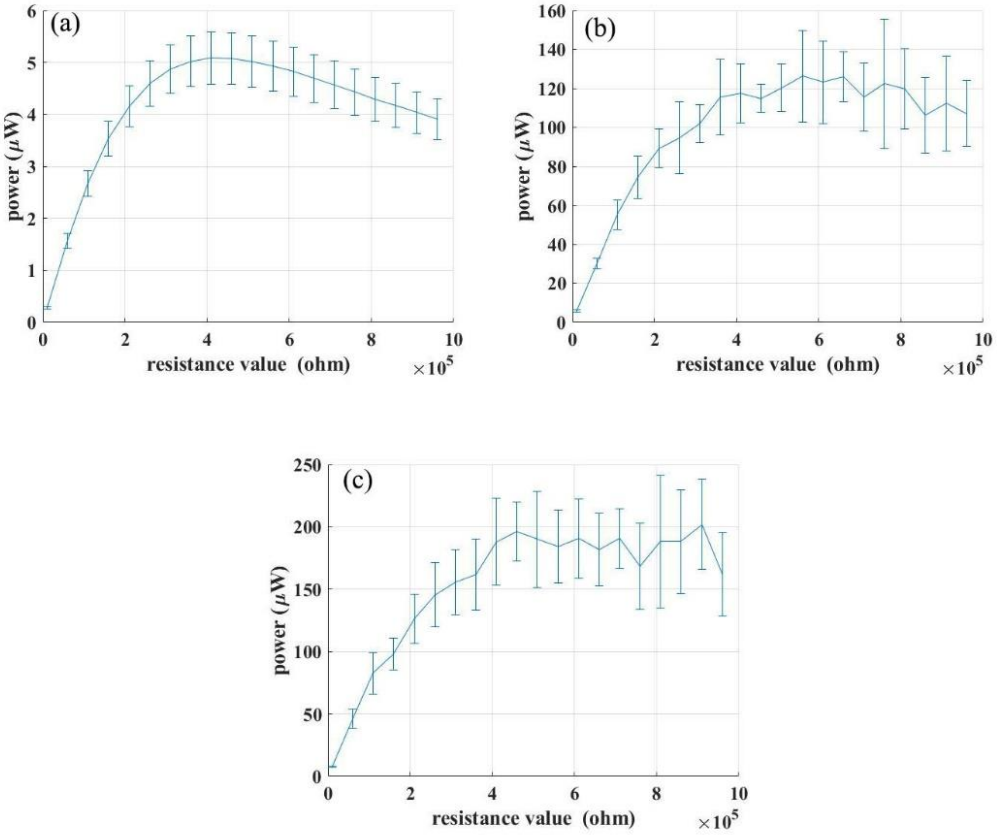

Figure 4.10 Simulation results of the relationship between the output power and load resistance of BEH2 under the colored noise excitation: (a) the low-level excitation; (b) the medium-level excitation; (c) the high-level excitation.

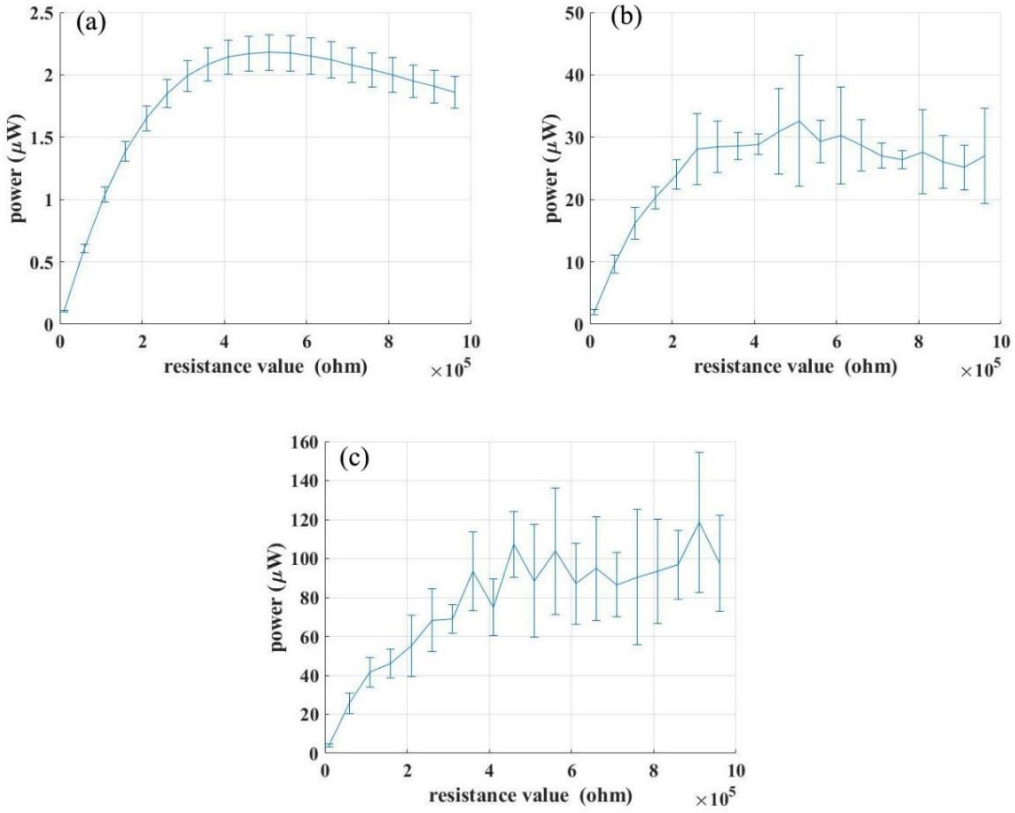

Figure 4.11 Simulation results of the relationship between the output power and load resistance of BEH3 under the colored noise excitation: (a) the low-level excitation; (b) the medium-level excitation; (c) the high-level excitation.

4.1.3 Experimental Validation

The experimental validations of BEH1, BEH2 and BEH3 which are subjected to the three different excitation levels are also conducted. The voltage signals is recorded for the time period of 60 seconds. The RMS values of the voltage signals are used to compute the output powers. It should be noticed that the trend of the experimental results is fairly repeatable, there is no need to take multiple measurements for each of the setups.

The experimental results of BEH1 under the low-level, middle-level and high-level random excitations are shown in Figure 4.12 (a), (b) and (c), respectively. The optimum

resistance values obtained by the experiments are listed in Table 3.1. The maximum values of the corresponding output powers are also listed.

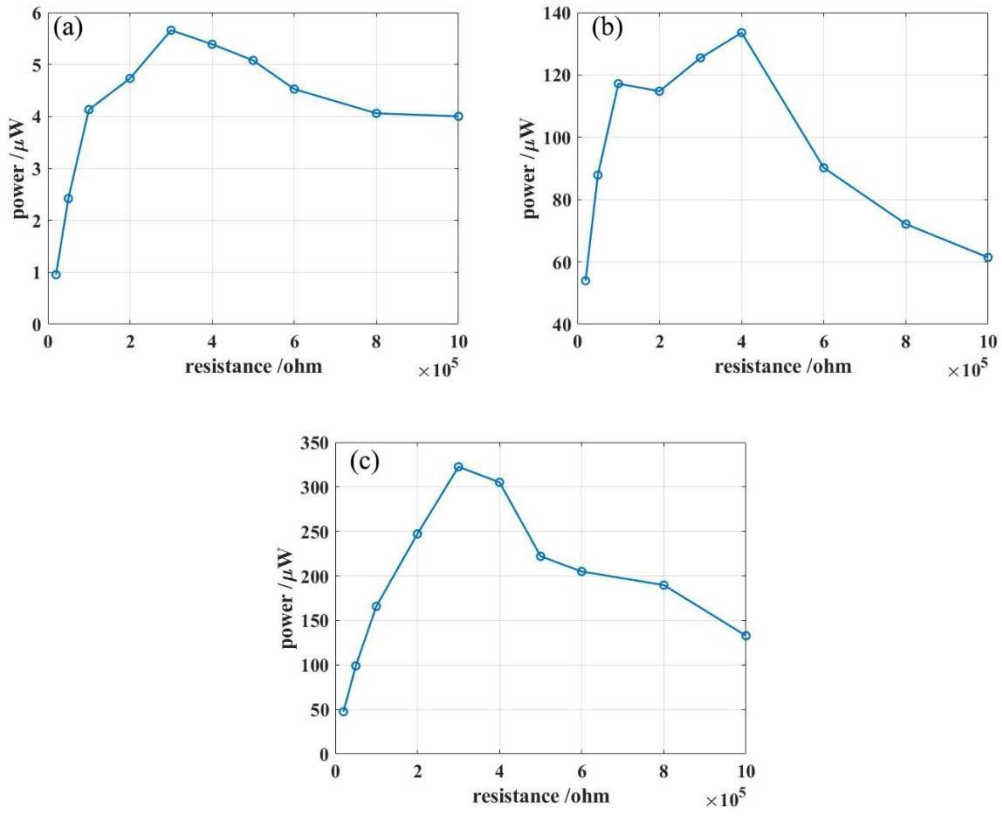

Figure 4.12 Experimental results of the relationship between the output power and the load resistance of BEH1 under the different random excitation levels: (a) the low-level excitation; (b) the medium-level excitation; (c) the high-level excitation.

Comparing the simulation results shown in Figure 4.9 and the experimental results shown in Figure 4.12 reveals some similarities and discrepancies. In both cases, as the load resistance increases, the output power rises rapidly. However, when the output power reaches its maximum value, it decreases with an increase of the resistance. This trend agrees with the one from the simulation under the low-level excitation and does not agree with those from the simulations under the middle-level and high-level excitations. To explain this difference, the performance of BEH1 under the high-level excitation is further

investigated.

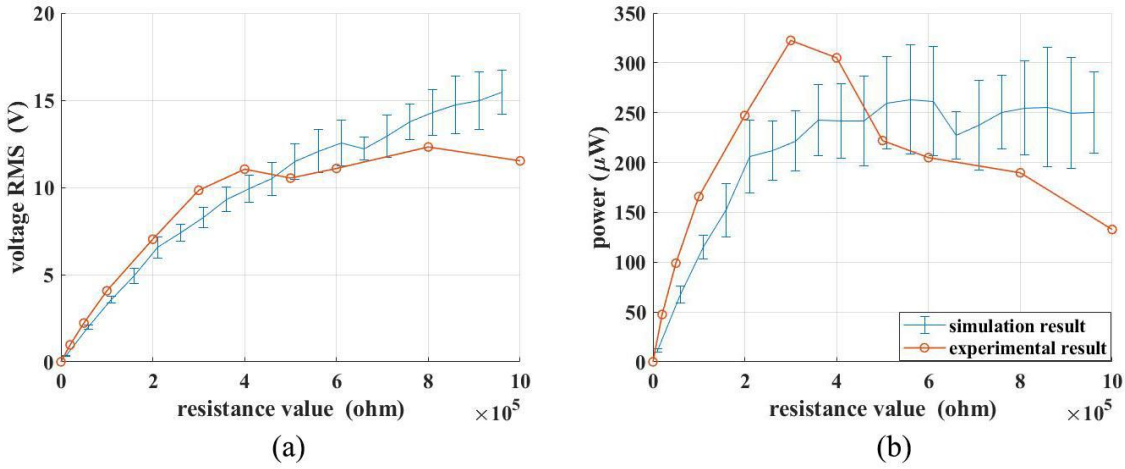

Figure 4.13 Comparison of the simulation results and experimental results for BEH1 under the high-level excitation: (a) the voltage response; (b) the output power.

As shown in Figure 4.13 (a), the simulation voltage response increases gradually as the load resistance increases while the experimental voltage response increases at a rapid rate first and then at a slow rate after the load resistance is higher than 400 KΩ. A reasonable explanation is that when the piezoelectric beam oscillates between the two wells, the simulation results of the response voltage can reach a very high value (peak amplitude of 50 V), while the voltage output from the real piezoelectric beam can not reach such a high value. As a result, the real system's output power will decrease when the load resistance value is higher than the optimum resistance. In addition, the real output power reaches the peak value when the load resistance at 300 KΩ, which is lower than the optimum resistance value obtained from the simulation.

The experimental results of BEH2 and BEH3 are shown in Figure 4.14 and Figure 4.15, respectively. The obtained optimum resistance values and corresponding maximum output powers are listed in Table 4.2 and Table 4.3, respectively.

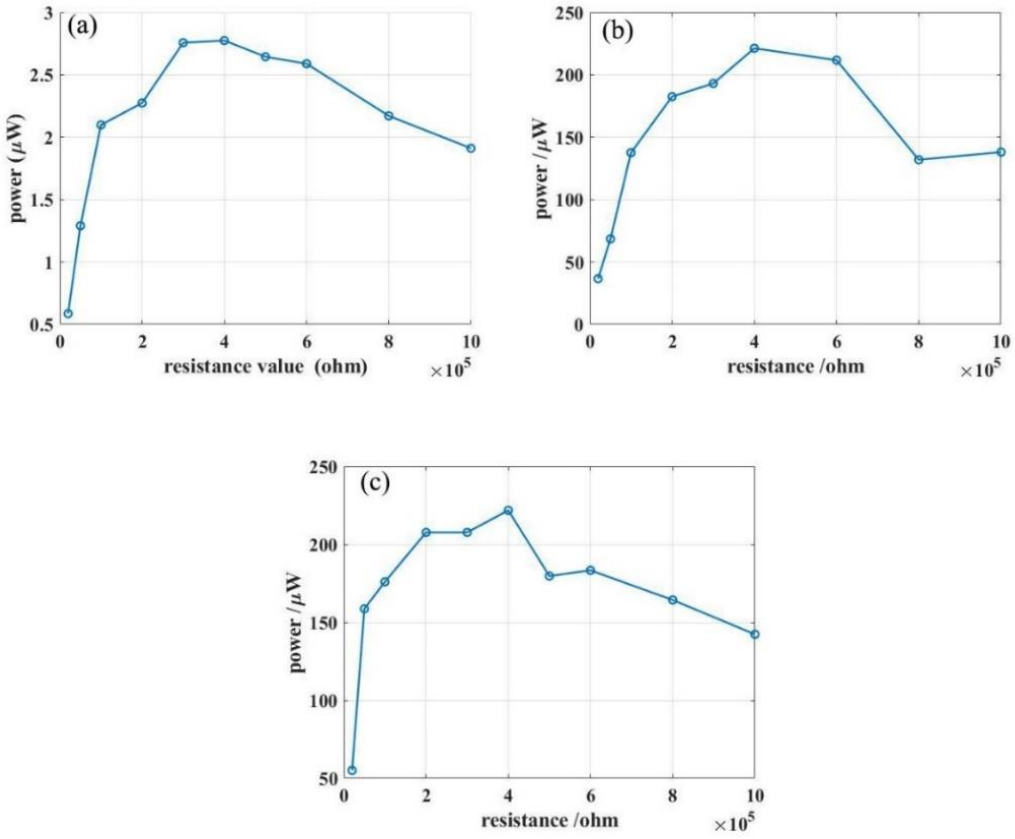

Figure 4.14 Experimental results of the relationship between the output power and the load resistance of BEH2 under the different random excitation levels: (a) the low-level excitation; (b) the medium-level excitation; (c) the high-level excitation.

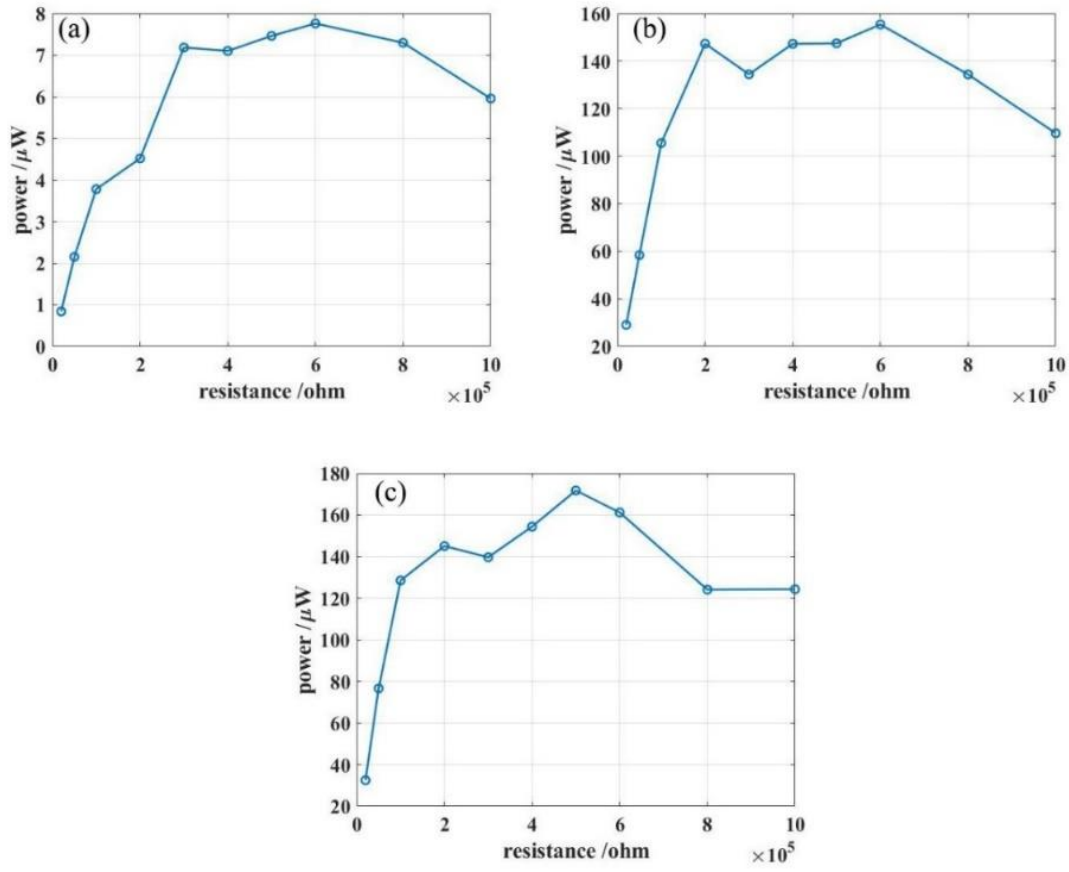

Figure 4.15 Experimental results of the relationship between the output power and the load resistance of BEH3 under the different random excitation levels: (a) the low-level excitation; (b) the medium-level excitation; (c) the high-level excitation.

4.1.4 Discussion of the Results

As shown in Table 4.1, under the low-level excitation or when the system operates in the intra-well oscillation mode, the calculation results based on the dominant frequency of the simulation open-circuit time response, the simulation results and experimental results of the optimum resistance are all around 300 KΩ. On the other hand, the calculation and simulation results of the optimum resistance exhibit an increasing trend when the system switches from the intra-well oscillation mode to the inter-well oscillation mode. The main reason is that the low-frequency components of the voltage response become more

significant when the bi-stable system enters into the inter-well oscillation mode. This means that the system's internal impedance (equal to the optimum resistance) is larger when the system operates in the inter-well oscillation mode than in the intra-well oscillation mode.

The optimum resistances obtained from the experimental results vary little as the excitation level increases. Such a phenomenon can be attributed to the fact that the output voltage of the real piezoelectric energy harvester reaches its limit when the system operates in the high energy orbit. The same trend can also be found in Table 4.2 and Table 4.3.

According to the simulation results and experimental results are shown in Table 4.1, Table 4.2 and Table 4.3, the maximum output power increases when the excitation level increases. And the performance of the piezoelectric energy harvester can be greatly enhanced when the system operates in the inter-well oscillation. Since BEH1 has a larger distance between two wells, it can generate more power among the three BEHs.

As shown in the first two columns of Table 4.3, the simulation results are much lower than the experimental results for both optimum resistance and maximum output power. This discrepancy may be attributed to the inaccurate dynamic models and vibration isolation characteristics of the BEHs. It can be further explained as follows: for the situation of BEH3, The frequency band of the input colored noise excitations used in the experiments are from 3 Hz to 20 Hz, which are higher than the resonance frequency of BEH3's numerical model (2 Hz). It means that the numerical model operates in the isolation region, While the resonance frequency of the real BEH3 is about 3 Hz which is slightly higher than that of the numerical model, due to the resonance phenomenon, the average deflections of the real piezoelectric beam is obviously larger than that of the simulations. This explains why the output powers based on the experimental results are greater than that based on the simulation results.

Further, it can be concluded that if the frequency range of the colored noise excitation covers the system's resonance frequency range, and the system operates in the intra-well

oscillation, the shallower potential wells can make the BEH more efficient.

Table 4.1 Optimum resistances and maximum output powers of BEH1 obtained by the three methods.

Method	**Low-level**		**Middle-level**		**High-level**	
	R_{opt} (KΩ)	P_{max} (μW)	R_{opt} (KΩ)	P_{max} (μW)	R_{opt} (KΩ)	P_{max} (μW)
Calculation	388	-	438.8	-	426	-
Simulation	360	1.9	360	163.3	560	305.9
Experiment	300	5.6	400	133.5	300	322.5

Table 4.2 Optimum resistances and maximum output powers of BEH2 obtained by the three methods.

Method	**Low-level**		**Middle-level**		**High-level**	
	R_{opt} (KΩ)	P_{max} (μW)	R_{opt} (KΩ)	P_{max} (μW)	R_{opt} (KΩ)	P_{max} (μW)
Calculation	438	-	463	-	498	-
Simulation	410	5.0	560	126.3	460	196.4
Experiment	400	2.7	400	221.3	400	221.9

Table 4.3 Optimum resistances and maximum output powers of BEH3 obtained by the three methods.

Method	Low-level		Middle-level		High-level	
	R_{opt} (KΩ)	P_{max} (μW)	R_{opt} (KΩ)	P_{max} (μW)	R_{opt} (KΩ)	P_{max} (μW)
Calculation	527	-	592	-	596	-
Simulation	510	2.2	510	32.6	560	107.3
Experiment	600	7.8	600	166.1	500	171.7

To sum up, the calculated predictions and simulation results are relatively accurate when the BEH behaves as a linear system in the intra-well oscillation mode. When the system operates in the inter-well oscillation mode, the optimum resistance of an ideal BEH shows an increasing trend as the excitation level rises while the optimum resistance of the real BEH is relatively consistent due to the limitation of the output voltage capability. The range of the optimum resistance for each system can be determined as follows: 300-400 KΩ for BEH1; 400-500 KΩ for BEH2; 500-600 KΩ for BEH3.

On the other hand, when the BEH operates in the intra-well oscillation mode, the power output is influenced by the depth of the potential wells. The system that has shallower potential wells is more efficient in energy harvesting. And when the system operates in the inter-well oscillation, the key factor which influences the harvesting performance is the distance between the two wells. So the BEH3 and BEH1 are the most efficient configurations when the system operates in the intra-well and inter-well oscillation modes, respectively.

4.2 The Output Power verse the Excitation Level of BEHs

This section focuses on the relationship of the output power verse the excitation level.

For this purpose, the value of the load resistance is kept to be 1000 KΩ and the level of the colored noise excitation is varied.

4.2.1 Numerical Simulation

The random excitation signals used in the simulations are obtained from the experimental tests by measuring the base displacements. The excitation level is measured by the integrals of PSD of the base acceleration. The following values are used in the simulations: 0.205 g, 0.487 g, 0.639 g, 0.822 g, 0.959 g, 1.153 g, 1.391g, and 1.569g. With the initial displacements: 0.0273 m for BEH1, 0.0252 m for BEH2 and 0.0226 m for BEH3, Eq. (4.1) and Eq. (4.2) are solved for the period of T=60 s using the MATLAB ODE45 solver for the relative displacements and the load voltage responses. Based on the RMS values of the voltage response shown in Figure 4.16 (a), the output powers under the different excitation levels are obtained, and shown in Figure 4.16 (b). The points A1, B1 and C1 correspond to the excitation levels at which the BEHs operate in the intra-well oscillation. The points A2, B2 and C2 correspond to the excitation levels at which the BEHs switch to the inter-well oscillation. The time responses and phase portraits of A1, A2 are shown in Figure 4.17, the time responses and phase portraits of B1, B2 and C1, C2 are demonstrated in Figure 4.18 and Figure 4.19, respectively.

As illustrated in Figure 4.16 (b), when the excitation level is lower than 1.153 g, BEH2 is more efficient in energy harvesting. And it is the easiest to enter the inter-well oscillation mode among the three BEHs. In addition, when the three BEHs both operate in the inter-well oscillation, BEH1 is the most efficient one.

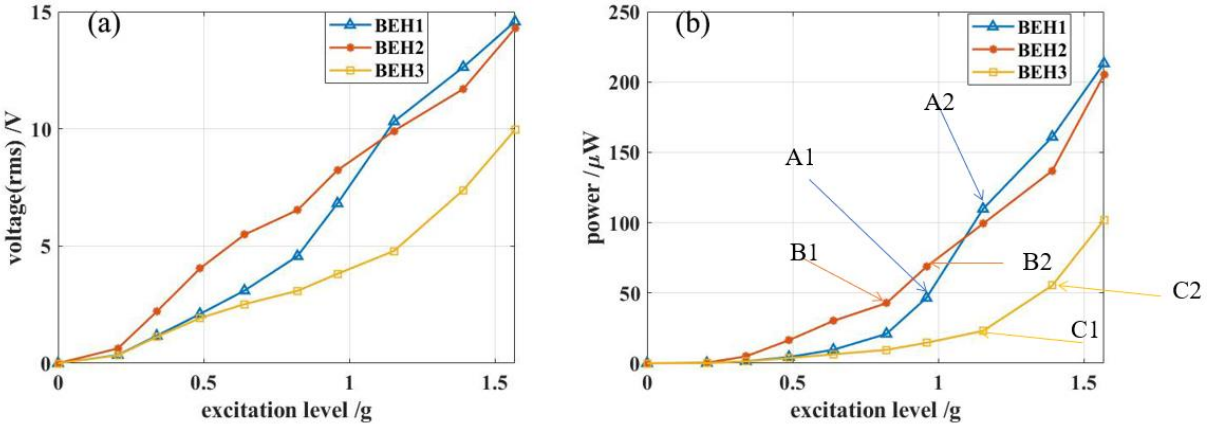

Figure 4.16 The simulation results of the three BEHs: (a) the voltage responses; (b) the output powers.

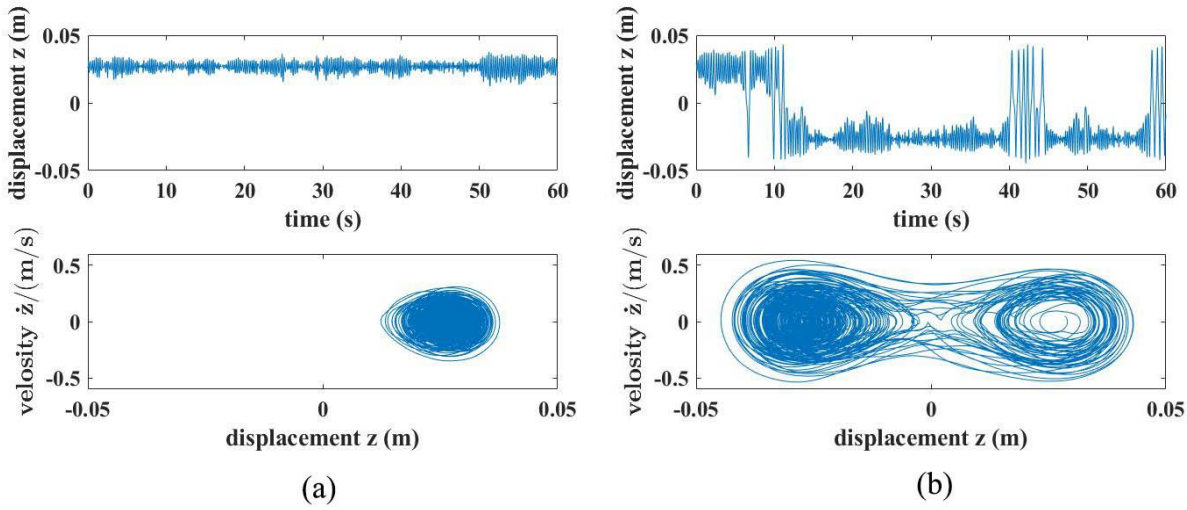

Figure 4.17 The simulation results of time response (upper plot) and phase portrait (lower plot) of BEH1 under the specific level of random excitation: (a) under the A1 excitation level; (b) under the A2 excitation level.

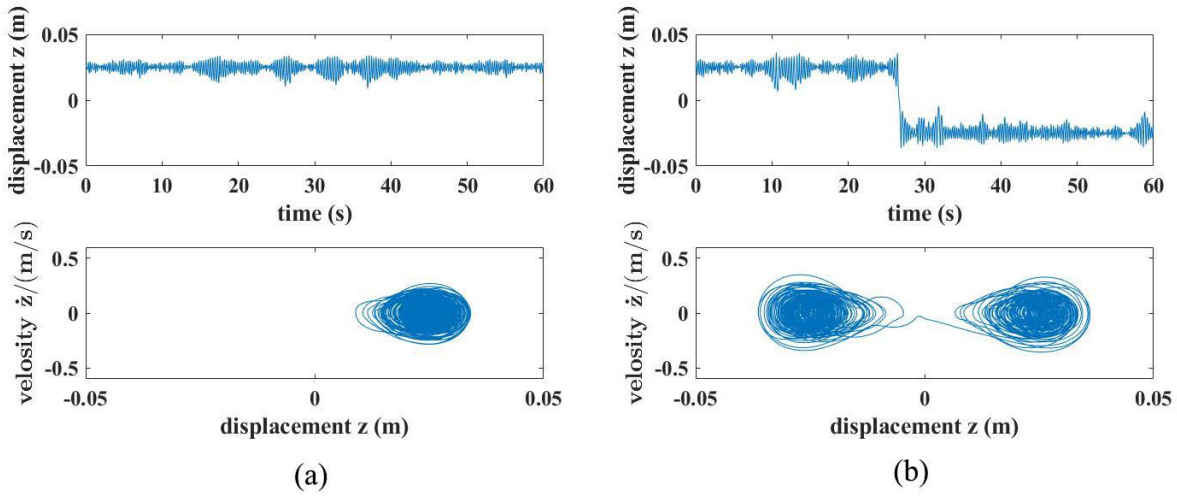

Figure 4.18 The simulation results of time response (upper plot) and phase portrait (lower plot) of BEH2 under the specific level of random excitation: (a) under the B1 excitation level; (b) under the B2 excitation level.

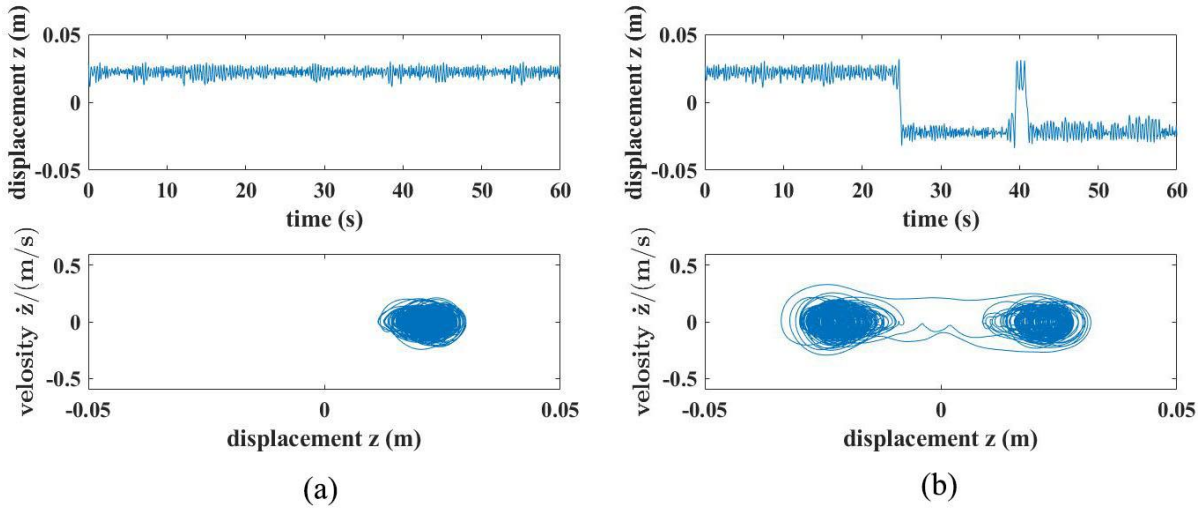

Figure 4.19 The simulation results of time response (upper plot) and phase portrait (lower plot) of BEH3 under the specific level of random excitation: (a) under the C1 excitation level; (b) under the C2 excitation level.

4.2.2 Experimental Validation

In this section, a series of experimental validations of the voltage resposes and output powers for the BEHs under the different excitation levels are conducted. The experimental results are shown in Figure 4.20. The points A, B and C indicate that BEH1, BEH2 and BEH3 switch from the intra-well oscillation mode to the inter-well oscillation mode. Their time responses and phase portrait plots are shown in Figure 4.21 (a), (b) and (c). The corresponding excitation levels are 1.153 g, 0.959 g, and 1.391 g, respectively. And it can be found that the values agree with the results obtained by the simulations.

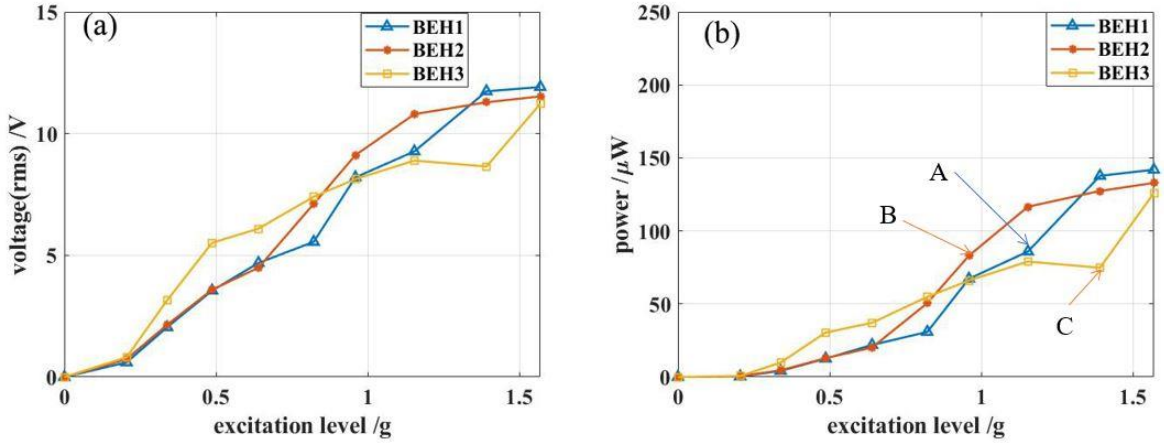

Figure 4.20 The experimental results of the three BEHs: (a) the voltage responses; (b) the power output.

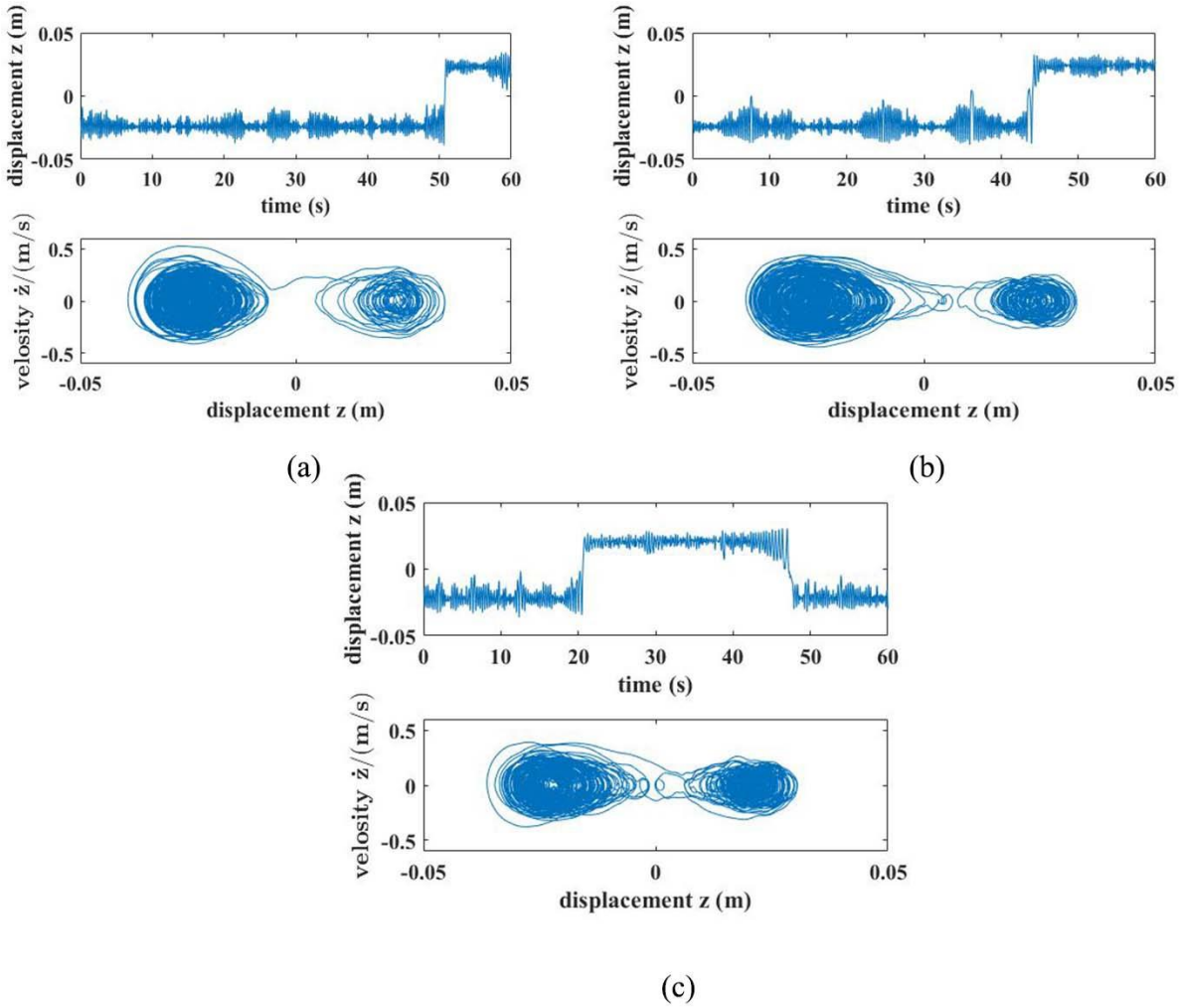

Figure 4.21 The experimental results of time response (upper plot) and phase portrait (lower plot) of three systems under the specific level of random excitation: (a) BEH1 under the A excitation level; (b) BEH2 under the B excitation level; (c) BEH3 under the C excitation level.

As shown in Figure 4.20 (b), when the excitation level is lower than 0.822 g, BEH3 can generate more power. When the excitation is between 0.822 g and 1.391 g, BEH2 is more effective since it starts to operate in the inter-well oscillation mode at the point B. When the excitation level is higher than 1.391 g, the three BEHs both enter the inter-well oscillation mode. In this case, BEH1 becomes the most efficient system due to its widely separate potential wells.

4.3 Conclusions

In this chapter, the optimum resistances for the three different BEHs have been determined, And the comparison of their power output performances has also been conducted.

The results show that the frequency analysis method can be used to determine the optimum resistance for the nonlinear energy harvester. As the calculation results and the simulation results have shown, the optimum resistances will increase when the BEHs enter the inter-well motion. Since the real BEHs has a limited voltage output when they operate in the high energy orbit, then, the increasing trends are not obvious in the experimental results. However, the results still verify that the ranges of the optimum resistance are: 300-400 KΩ for BEH1; 400-500 KΩ for BEH2; 500-600 KΩ for BEH3.

By comparing the output performances of the three BEHs, it can be concluded that BEH 2 is much easier to enter the inter-well oscillation under the low level excitations, and BEH 1 can generate more energy when the excitation level is high.

Future research could consider the effect of the voltage limit phenomenon in modelling. For instance, the electromechanical coupling coefficient θ can be represented by a function of the relative displacement. When the relative displacement exceeds a certain level, θ is reduced.

Chapter 5 Tri-stable Energy Harvesters under the Colored Noise Excitation

In the previous chapter, a comparison of the performances of the three bi-stable vibration energy harvesters (BEHs) has been carried out. And it has been concluded that the inter-well oscillation mode can significantly improve the system's output performance, and in this mode, the BEH that has a larger separation between the two equilibrium positions can produce more power. The study has shown that among the three BEHs considered, BEH1 is the most efficient one. But the deeper wells can make it harder for the system to operate at the inter-well oscillation mode. Hence, in order to balance the separation distance between the wells and the depth of the wells, adding a middle potential well in between the two wells to generate a tri-stable system can be seen as a solution.

For our system, the tri-stable state can be achieved by reducing d and increasing h. The potential functions of a BEH with the configuration of d=0.0467 m, h=0.0157 m and a tri-stable energy harvester (TEH) with the configuration of d=0.0377 m, h=0.0188 m are shown in Figure 5.1 The separation distances for the TEH and BEH are represented by $\Delta D1$ and $\Delta D2$, respectively. While the depths of the potential wells for THE and BEH are represented by $\Delta U1$ and $\Delta U2$, respectively. As shown in the figure, the THE has a larger separate distance ($\Delta D1 > \Delta D2$) and shallower potential wells ($\Delta U1 < \Delta U2$) comparing with the BEH. This means that the tri-stable system could be easier to be set into the inter-well oscillation mode and generate more power.

This chapter focuses on the electromechanical performances of the TEHs. For this purpose, the three TEHs with different configurations are investigated and they are referred to as TEH1 (d=0.0377 m, h=0.0188 m), TEH2 (d=0.0397 m, h=0.0189 m) and TEH3 (d=0.0467 m, h=0.0188 m). As shown in Figure 5.2, the three chosen configurations can

make the apparatus exhibit strong, medium and weak tri-stable state behaviors, respectively. The potential functions of TEH1, TEH2 and TEH3 have one stable point at the middle and two stable points which are symmetrically located at: ±0.032 m , ±0.029 m and ±0.018 m, respectively.

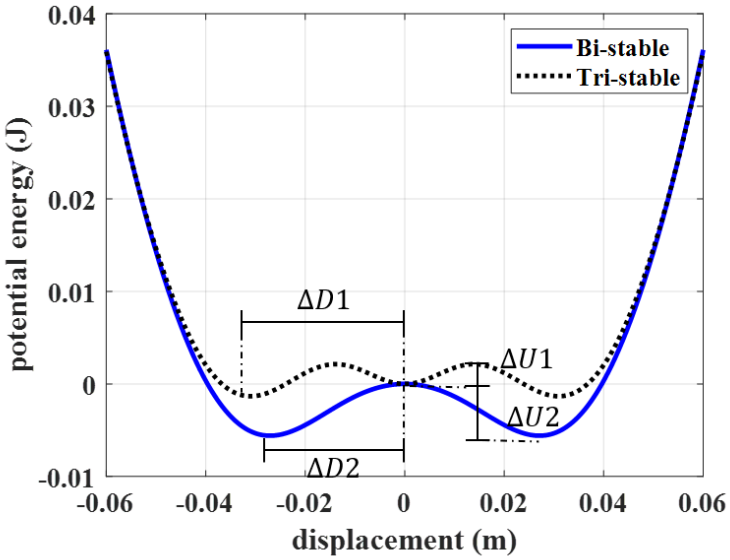

Figure 5.1 Potential energy of the BEH (blue solid line) and the THE (black dash line).

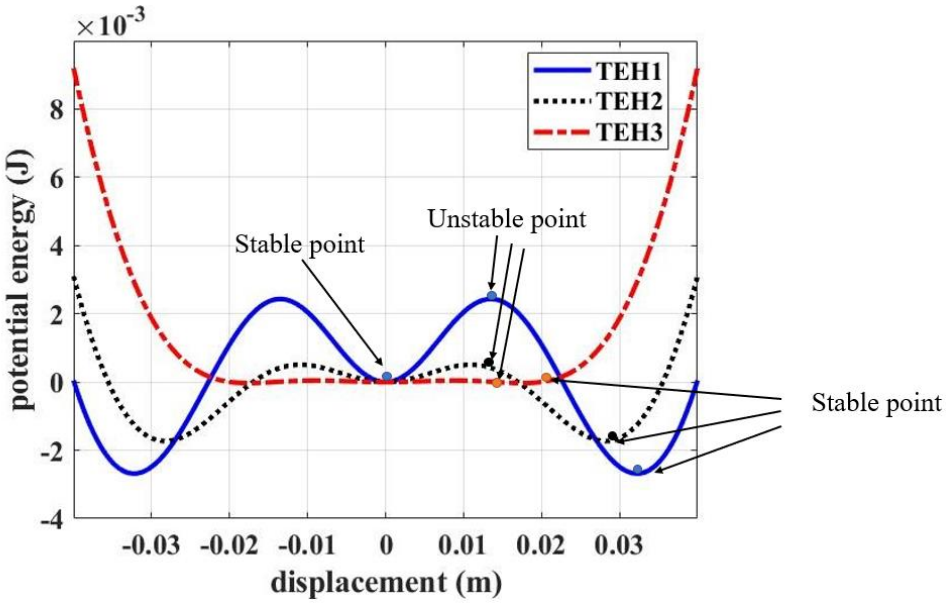

Figure 5.2 Potential energies of three strengths of TEHs: strong (TEH1), medium (TEH2) and weak (TEH3).

In this chapter, the output performances of these TEHs will be investigated, including numerical simulations and experimental validations of the optimum resistances for the three chosen TEHs. The power output performances under varying levels of random excitation will also be presented for each TEH. In the end, three TEHs' voltage responses and output powers under the increased level of excitation will be compared.

5.1 Optimum Resistance of the TEHs under the Colored Noise Excitation

5.1.1 Numerical Simulation of TEHs with an Open-Circuit

To obtain the optimum resistance for the chosen TEHs, the power spectrum analysis has been applied first. The base excitation used in the simulation is the colored noise acceleration which can be obtained from passing a white Gaussian noise signal through a 20^{th} order bandpass filter, and the lower and higher cut-off frequencies are chosen as 3 Hz

and 20 Hz, respectively. Three different excitation levels are considered, namely low-level excitation (S =0.205 g), medium-level excitation (S =1.115 g), and high-level excitation (S =1.569 g), where S represents the integral of the power spectrum density (PSD) of the colored noise acceleration. To mimic the open-circuit condition, the resistance value used in the simulation is 3MΩ. The numerical simulations for TEH1, TEH2 and TEH3 follow the same procedure as that mentioned in Section 4.1.1.

As shown in Figure 5.3, TEH1 has three potential wells located symmetrically around the origin. The trajectory (a) in Figure 5.3 represents an intra-well oscillation, in which the piezoelectric beam oscillates in one of the potential wells when the excitation is not strong enough. As demonstrated in Figure 5.4 (a), such an intra-well oscillation exhibits a strong linear behavior. The paths (b) and (c) in Figure 5.3 result in the chaotic inter-well oscillation, in which the piezoelectric beam oscillates between the three potential wells, and the corresponding time response plots and phase portrait plots are given in Figure 5.5 (b) and (c), respectively. It can be seen that under the medium-level excitation, TEH1 oscillates mainly in one of the wells and occasionally jumps to the other two wells, while under the high-level excitation, jumping occurs more frequently, and the oscillation exhibits strongly chaotic behavior.

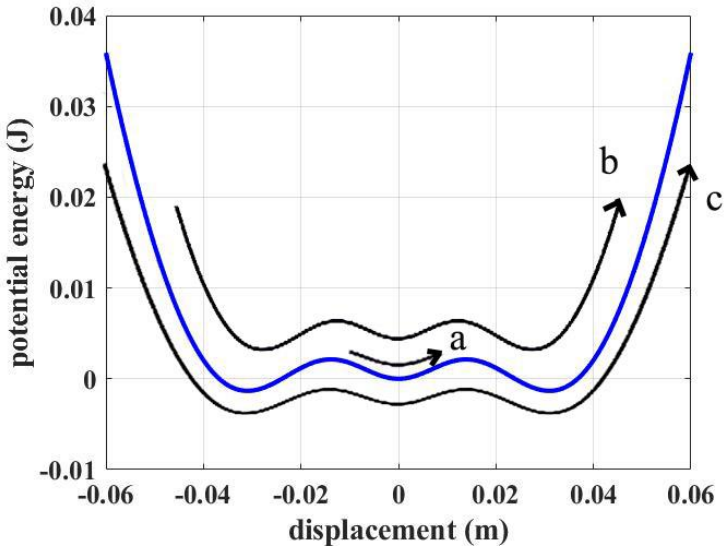

Figure 5.3 Oscillation modes of TEH1 under the three excitation levels: (a) intra-well oscillation; (b) weak inter-well oscillation; (c) strong inter-well oscillation.

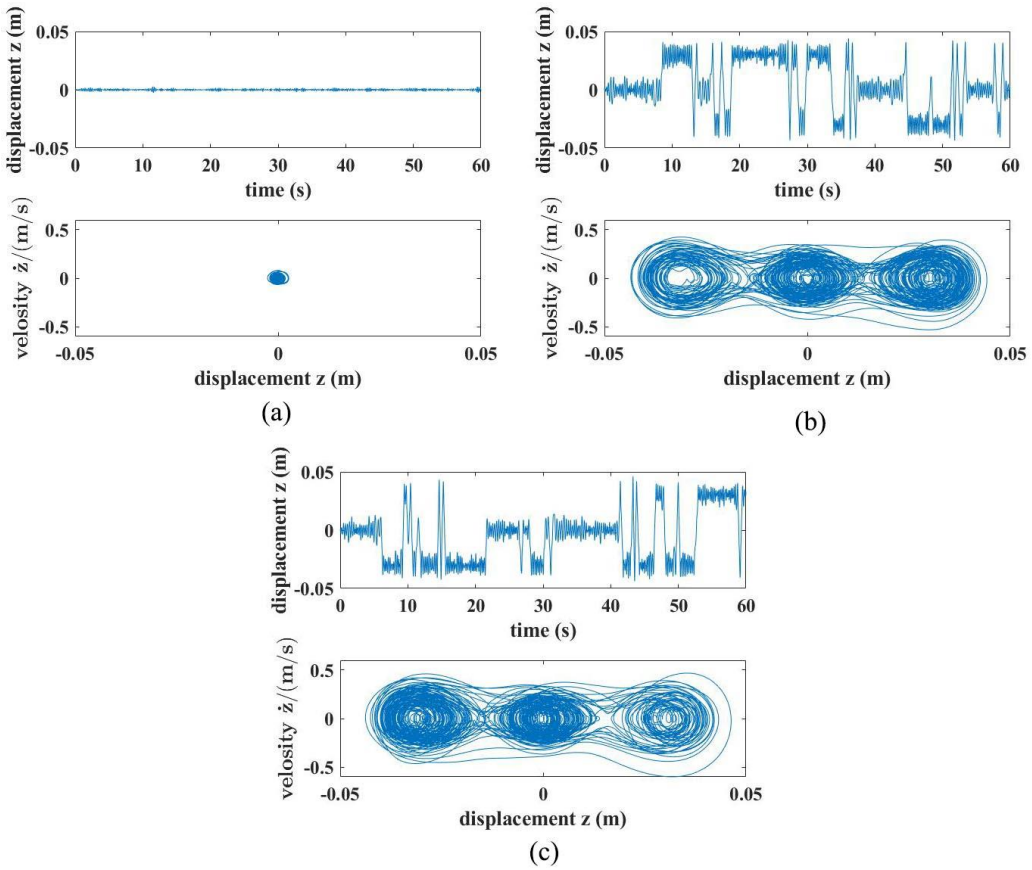

Figure 5.4 The time response (upper plot) and phase portrait (lower plot) of TEH1 under the colored noise excitation: (a) the low-level excitation; (b) the medium-level excitation; (c) the high-level excitation.

The voltage responses (upper plot) and the corresponding power spectra (lower plot) under the low-level excitation are shown in Figure 5.5 (a). It can be seen that the dominant frequency is 3.99 Hz. Then the optimum resistance is found to be 398.5 KΩ using Eq. (3.24). As illustrated in Figure 5.5 (b) and (c), the system operates in the inter-well oscillation under the medium-level and high-level excitation. Because of the variable frequency component of excitation and strong nonlinear characteristics of theTEH, multiple peaks are exhibited in the power spectrum. Hence, when the THE is engaged in a strong inter-well oscillation, the frequency analysis fails to identify a dominant frequency, which makes the determination of the optimum resistance impossible. Therefore, in the next section, the numerical simulation analysis is applied to estimate the optimum

resistance.

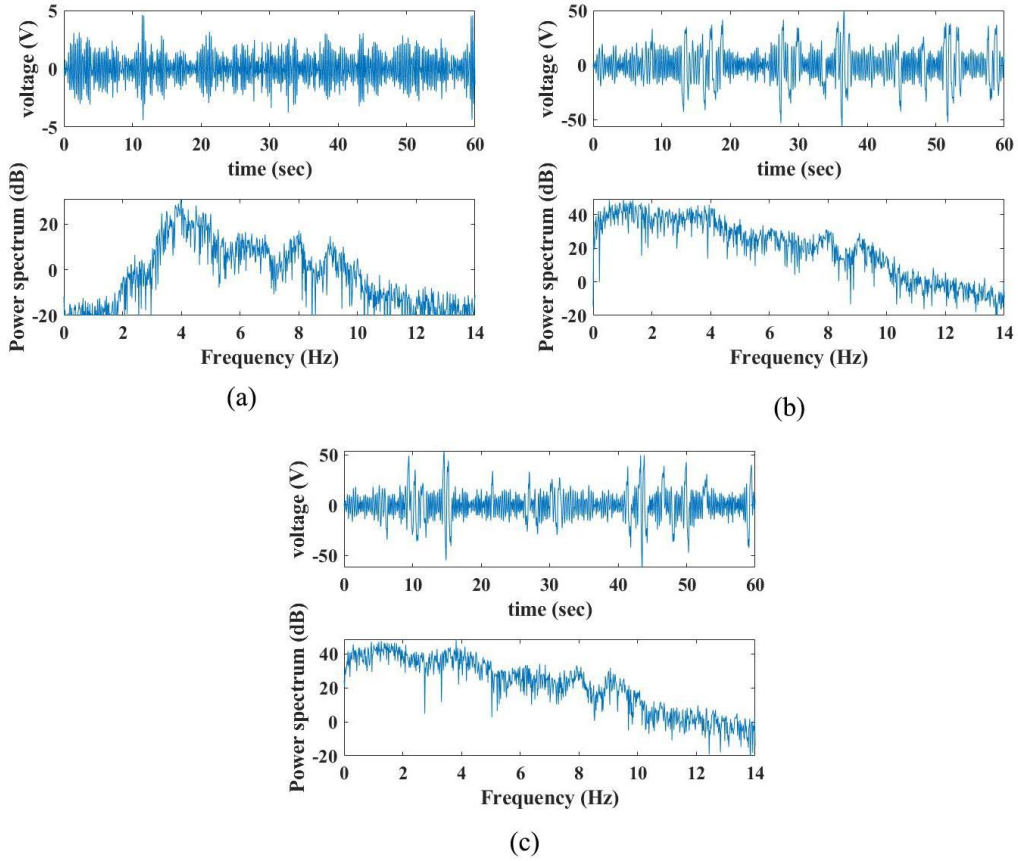

Figure 5.5 The time response and power spectrum of the open-circuit voltage of TEH1 under the colored noise excitation: (a) the low-level excitation; (b) the medium-level excitation; (c) the high-level excitation.

The three potential wells of TEH2 are shallower than those of TEH1. As discussed in the previous chapter, such a feature can benefit the harvesting performance. But in TEH2's case, shallower wells lead to a lower resonance frequency. If the middle well's resonance frequency is at the lower edge of the frequency range of the excitation, the system's vibration isolation character would have a negative effect on the harvesting performance. For example, by comparing the lower plot in Figure 5.4 (b) and Figure 5.6 (b), it can be seen that TEH2 moves between three potential wells not as often as TEH1.

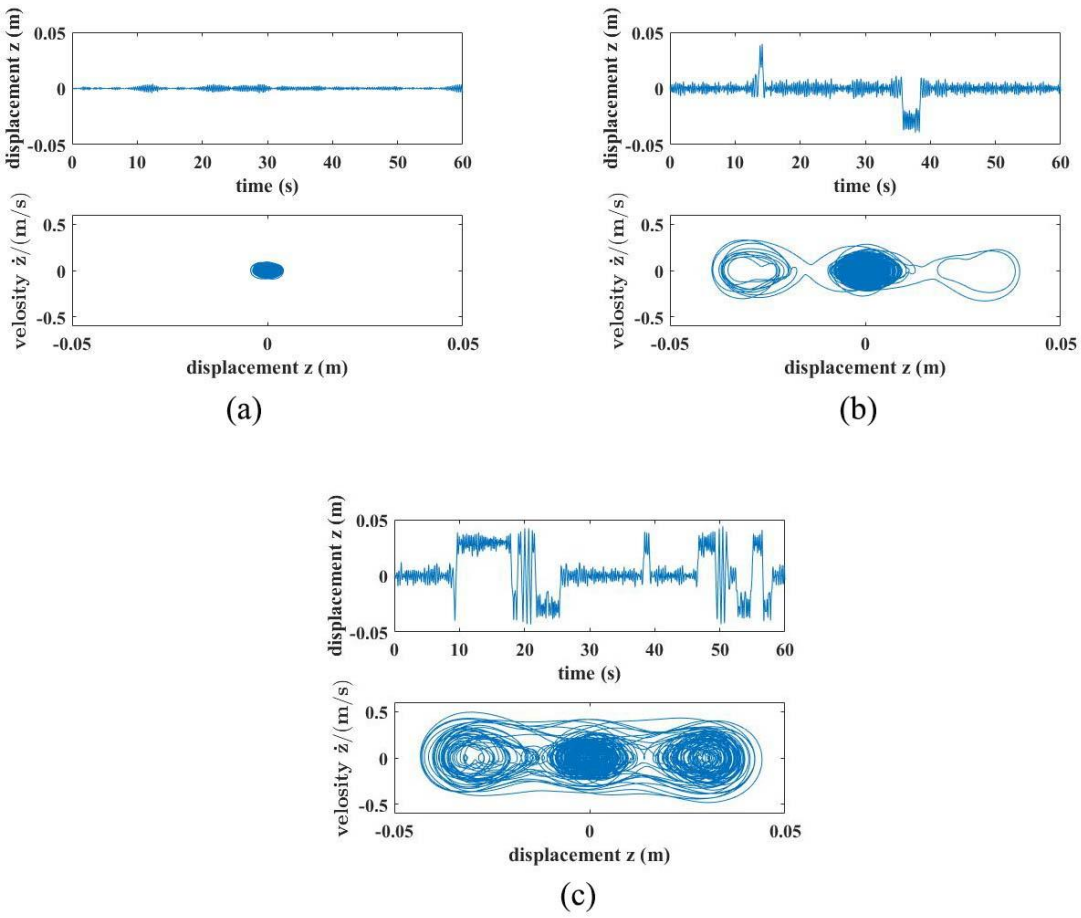

Figure 5.6 The time response (upper plot) and phase portrait (lower plot) of TEH2 under the colored noise excitation: (a) the low-level excitation; (b) the medium-level excitation; (c) the high-level excitation.

The open-circuit voltage response (upper plot) and the corresponding frequency spectrum (lower plot) of TEH2 under the three different levels of excitations are shown in Figure 5.7. as shown in Figure 5.7 (a) and (b), The dominant frequency of the low-level excitation and medium-level excitation can be found to be 3.5 Hz and 3.16 Hz, respectively. And the corresponding optimum resistances are 454 KΩ and 502 KΩ. As shown in Figure 5.7 (c), the dominant frequency of the voltage response under the high-level excitation is hardly identifiable, because TEH2 is already switched into the high orbit of the inter-well oscillation mode. Hence, the frequency analysis can be used to determine the optimum resistance when TEH2 operates in the intra-well oscillation and low orbit inter-

well oscillation mode. In comparison, the dominant frequency of TEH2 that operates at high orbit inter-well oscillation mode cannot be identified by the frequency analysis.

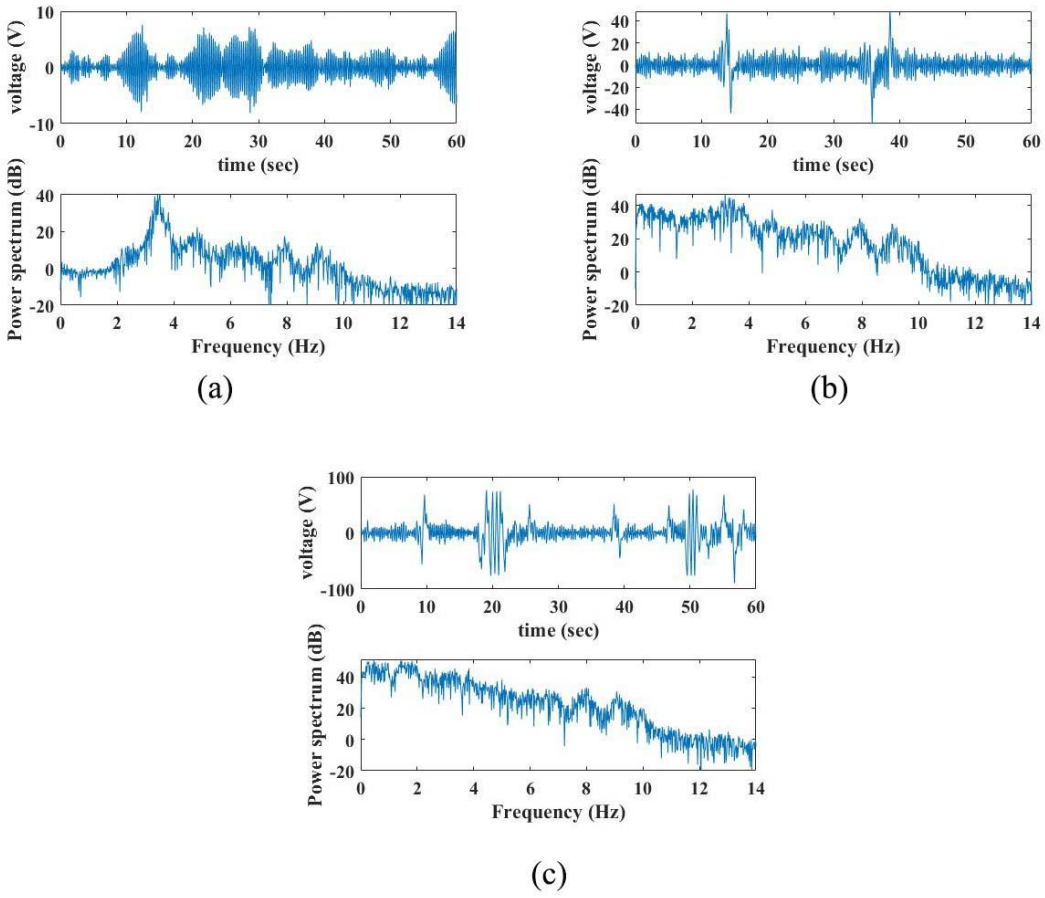

Figure 5.7 The time response and power spectrum of the open-circuit voltage of TEH2 under the colored noise excitation: (a) the low-level excitation; (b) the medium-level excitation; (c) the high-level excitation.

The potential wells of TEH3 or the weakTEH are shallowest among the three chosen tri-stable systems. As demonstrated in Figure 5.8 (a), (b) and (c), TEH3 operates in the intra-well oscillation mode under the three levels of excitation. It indicates that TEH3 is hard to be set into the inter-well oscillation mode. Because TEH3 has a quasi-zero stiffness over a large range as shown in Figure 5.2, such softening characteristics makes the beam less responsive to the base vibration. Accordingly, TEH3 is hard to be set into the inter-well oscillation mode.

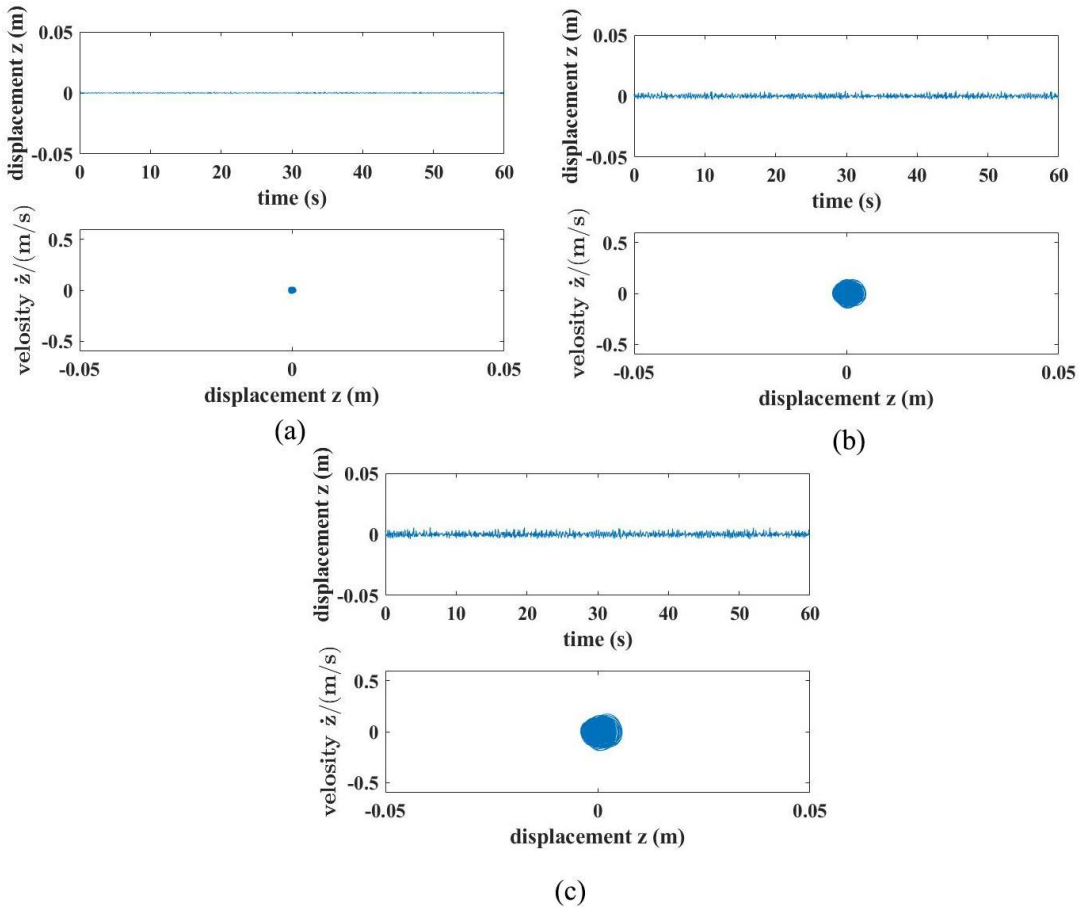

Figure 5.8 The time response (upper plot) and phase portrait (lower plot) of TEH3 under the colored noise excitation: (a) the low-level excitation; (b) the medium-level excitation; (c) the high-level excitation.

The open-circuit voltage response and the corresponding power spectrum of TEH3 under the three different levels of excitations are shown in Figure 5.9. Since the vibration is isolated by TEH3's softening characteristic, the relative displacement of the beam's tip is mainly the reduced base displacement. Then, the power spectrum of the response would exhibit all the base excitation's frequency components. Since the dominant frequency of the voltage response for TEH3 under the three levels of excitation is hardly distinguishable from the spectra, the calculation method fails to determine the optimum resistance in order to maximize the output power. Therefore, the numerical simulation analysis will be applied to estimate the optimum resistance for TEH3, in the next section.

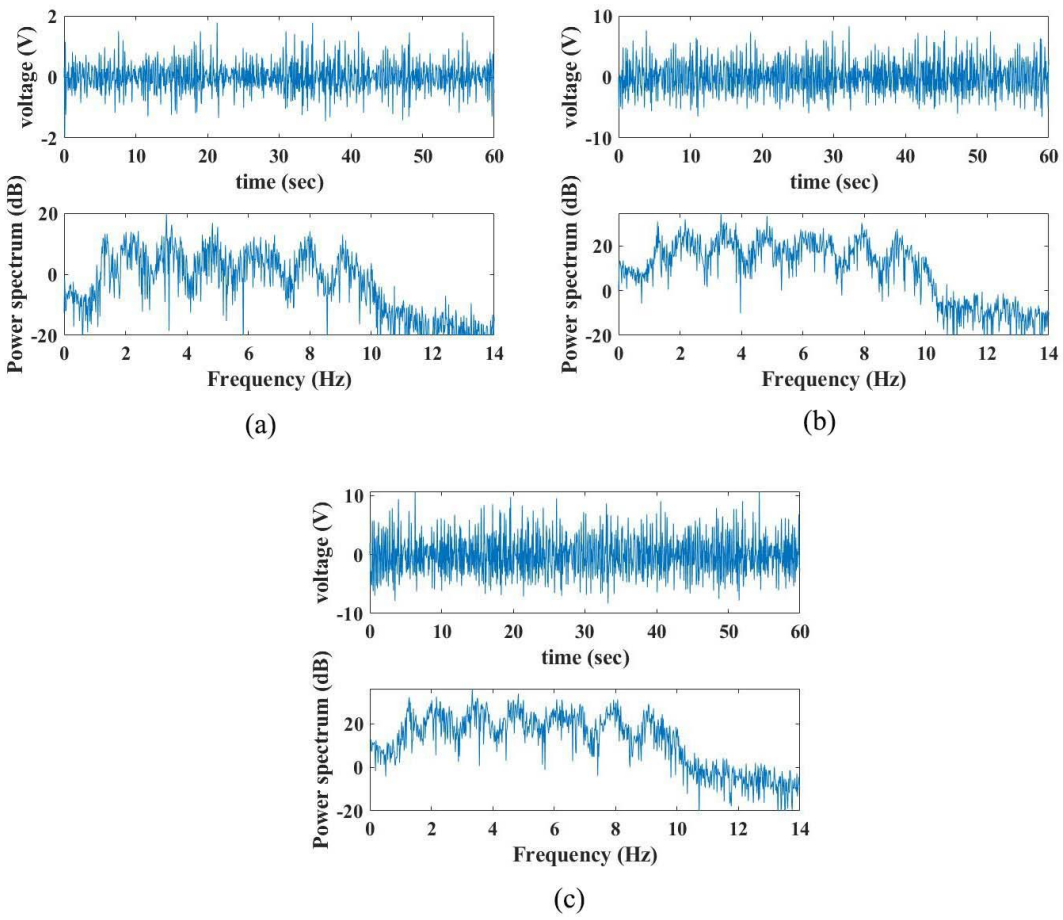

Figure 5.9 The time response and power spectrum of the open-circuit voltage of TEH3 under the colored noise excitation: (a) the low-level excitation; (b) the medium-level excitation; (c) the high-level excitation.

5.1.2 Numerical Simulation of TEHs with a Closed-Circuit

For the closed-circuit simulation, the load resistance varies from 10 KΩ to 1 MΩ in an increment of 50 KΩ. By solving Eq. (4.1) and Eq. (4.2) with zero initial conditions in the period of T=60 s using the MATLAB ODE45 solver, the relative displacement and the load voltage response can be obtained. Based on the RMS value of the voltage response over such a period, the corresponding output power can be calculated. To reduce the fluctuation of the output power, ten simulations have been conducted for each of the

resistance values. The error bar plot is used to reveal the variation of the responses. The top and bottom of the bar represent the maximum and minimum value of the output power in the ten simulations, respectively. The line curve of the error bar plot represents the average value of the ten simulations. Based on the average values, the optimum resistances for different excitation levels and their corresponding maximum output powers can be obtained. As shown in Figure 5.10 (a), the smooth curve represents that TEH1 operates in the intra-well oscillation. As shown in Figure 5.10 (b) and (c), the curves have some fluctuations, indicating that the system enters the inter-well oscillation mode. It can be obtained from Figure 5.10 (a), (b) and (c) that the optimum resistance values are 360 KΩ, 560 KΩ and 565 KΩ, respectively. Further, The optimum resistances and corresponding maximum output powers for TEH1 under the different excitations are listed in Table 5.1.

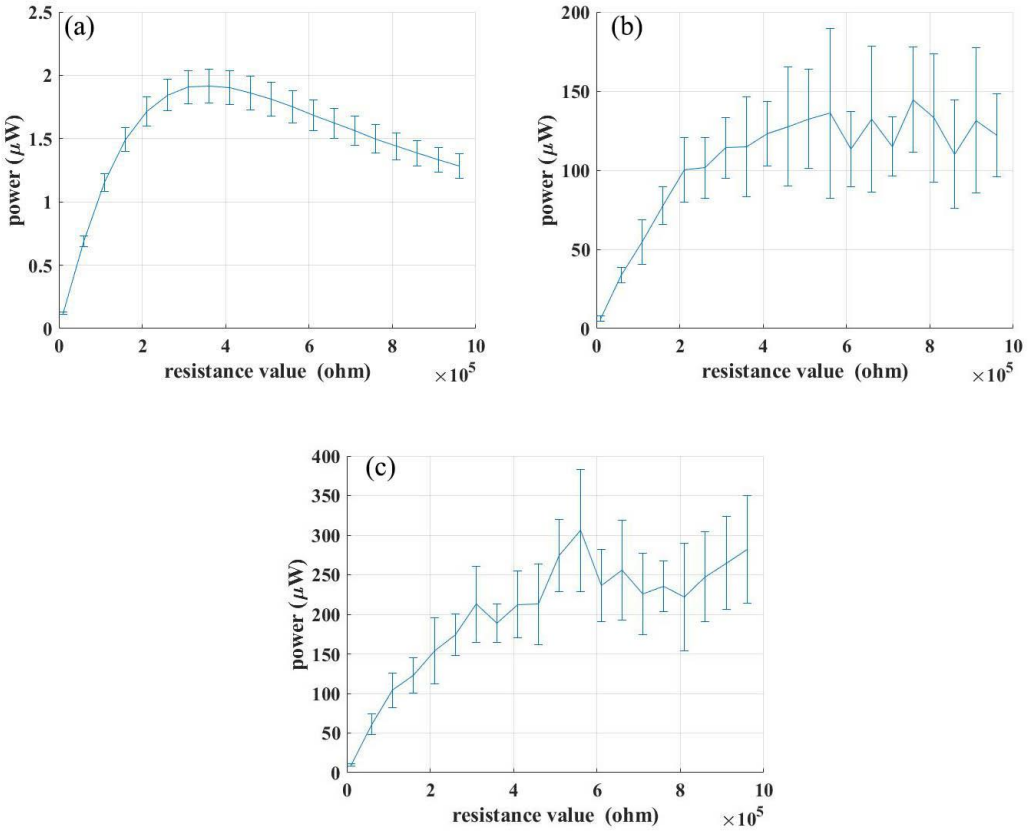

Figure 5.10 Simulation results of the relationship between the output power and load resistance of TEH1 under the colored noise excitation: (a) the low-level excitation; (b) the medium-level excitation; (c) the high-level excitation.

In addition, as illustrated in Figure 5.11 (a), (b) and (c), the optimum resistances for TEH2 are 460 KΩ, 500 KΩ and 560 KΩ, respectively.

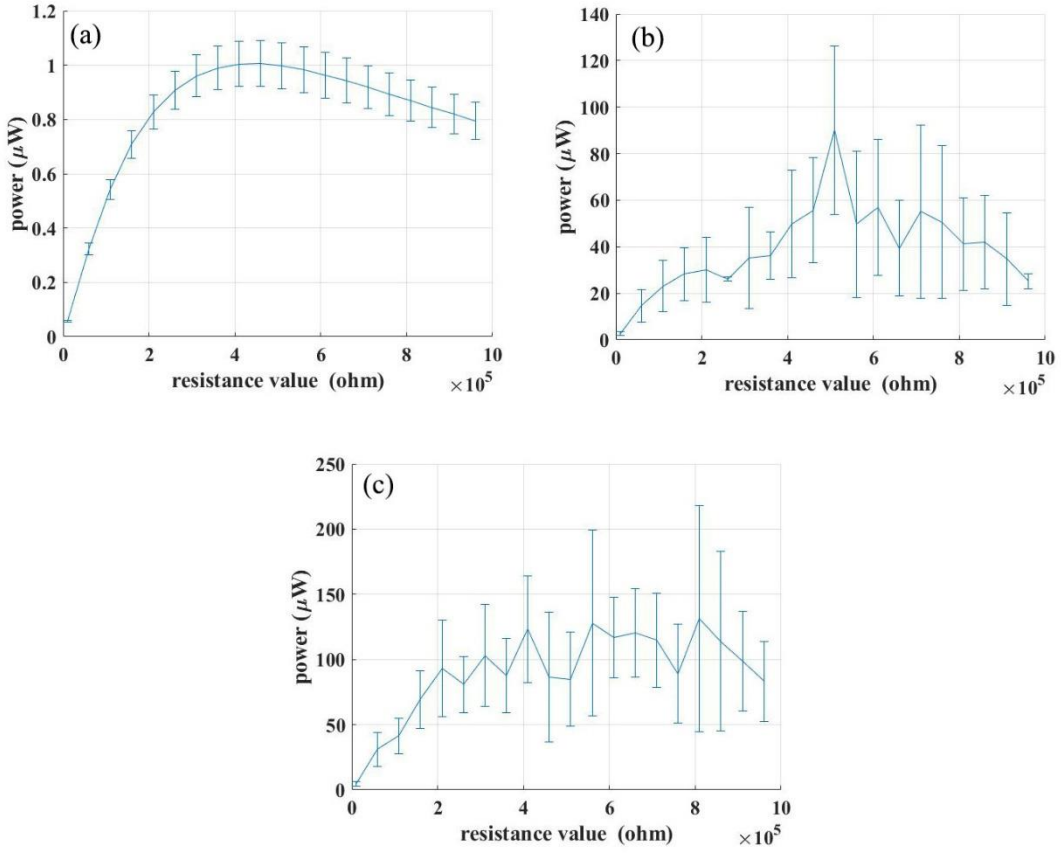

Figure 5.11 Simulation results of the relationship between the output power and load resistance of TEH2 under the colored noise excitation: (a) the low-level excitation; (b) the medium-level excitation; (c) the high-level excitation.

For TEH3, it can be observed from Figure 5.12 (a), (b) and (c) that the optimum resistances are 310 KΩ, 310 KΩ and 310 KΩ, respectively. The optimum resistances and corresponding maximum output powers under the different excitations for TEH2 and TEH3 are listed in Table 5.2 and Table 5.3, respectively.

It should be mentioned that the output power of TEH3 is relatively low comparing with TEH1 and TEH2 due to the vibration isolation character of the weak TEH. In fact, TEH3 can be considered to be a passive quasi-zero stiffness vibration isolator, and its vibration isolation characteristic can be explained as follow: The stiffness of TEH3 is almost zero around the middle region, which makes the natural frequency ω_n very low. When ω_n is

lower than $f/\sqrt{2}$, where f is the lowest exciting frequency, the vibration will be isolated. That could explain why TEH3 would only oscillate around the middle potential well under the three excitation levels [85].

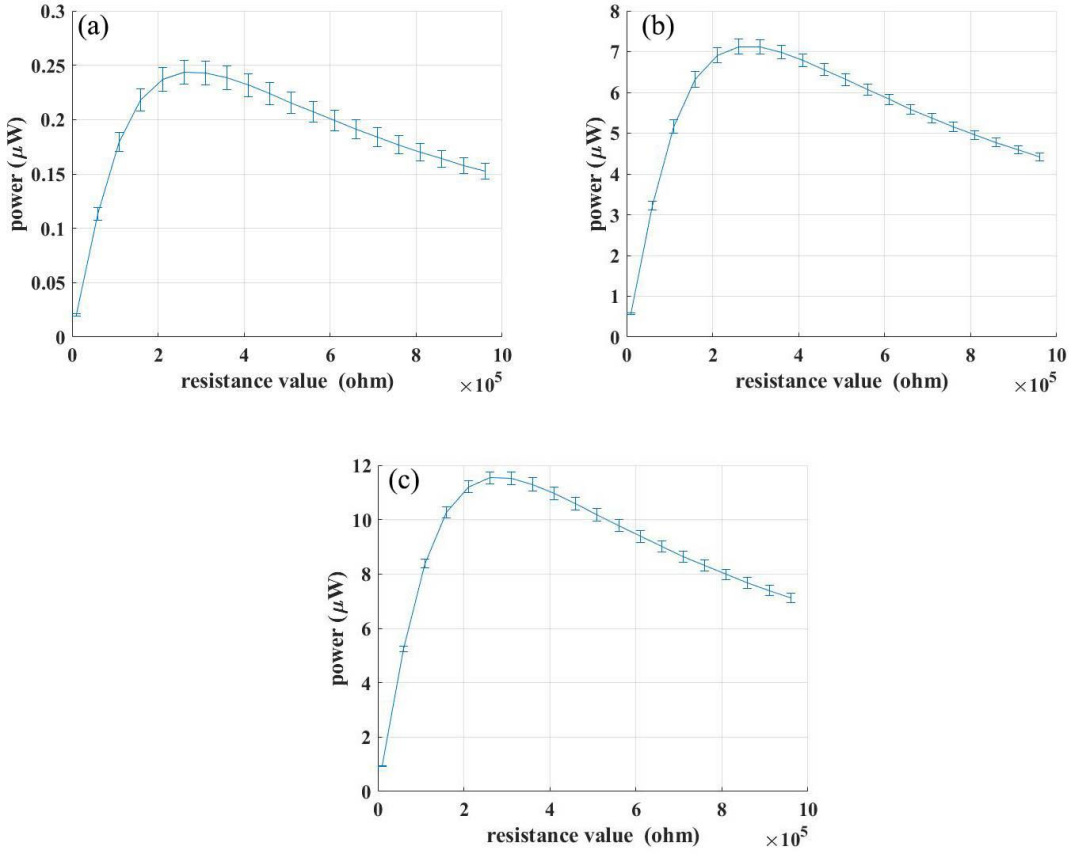

Figure 5.12 Simulation results of the relationship between the output power and load resistance of TEH3 under the colored noise excitation: (a) the low-level excitation; (b) the medium-level excitation; (c) the high-level excitation.

5.1.3 Experimental Validation

The experimental validation of the numerical simulation results is also conducted. The voltage signal is recorded for a time period of 60 seconds. The RMS value of the voltage signal is used to compute the output power. It should be noticed that as the experimental

results are fairly repeatable, the following presentation is based on a single measurement for each of the setups.

The experimental results of TEH1 under the low-level random excitation are shown in Figure 5.13. The optimum resistance value is 300 KΩ, which is close to the simulation result. Since the medium-level and high-level excitation may damage the piezoelectric transducer, the experiment under these two excitation levels is not attempted. The maximum values of the corresponding output power are listed in Table 5.1. The experimental results of TEH2 and TEH3 are shown in Figure 5.14 and Figure 5.15, respectively. The obtained optimum resistance values and corresponding maximum output powers are listed in Table 5.2 and Table 5.3, respectively.

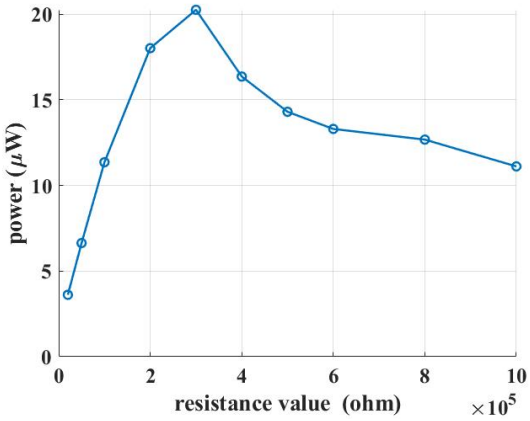

Figure 5.13 Experimental results of the relationship between the output power and the load resistance of TEH1 under the low-level random excitation.

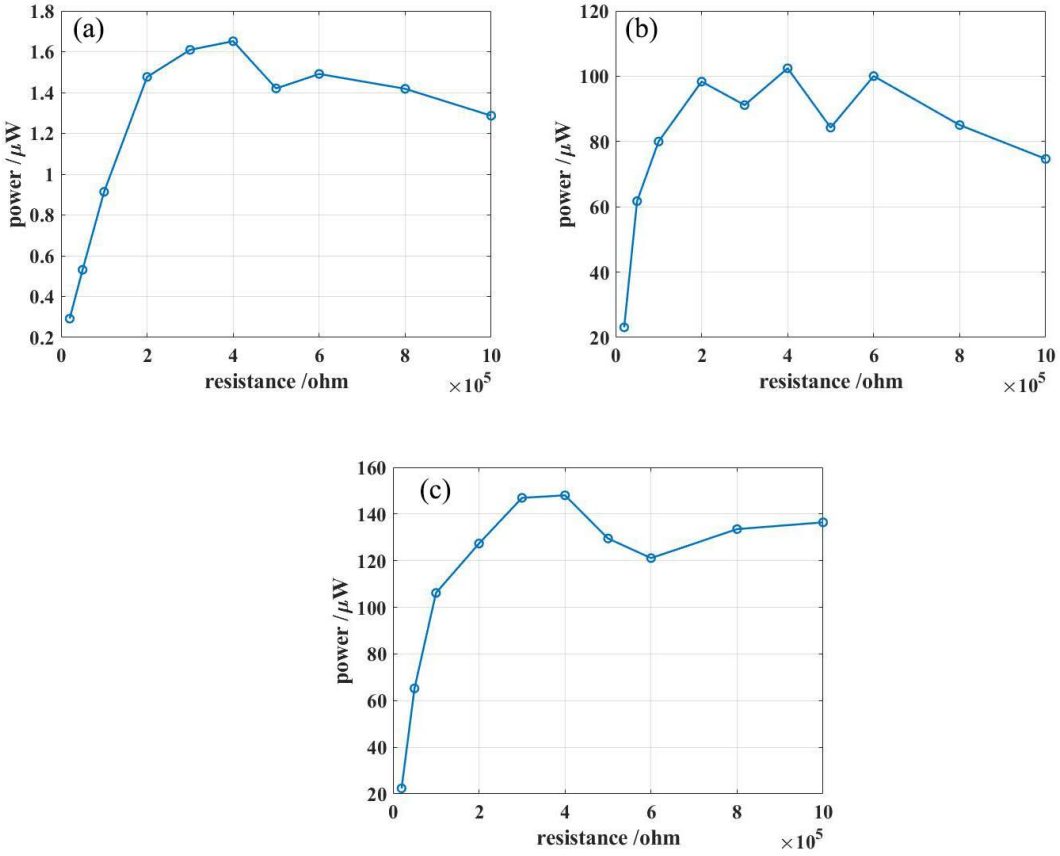

Figure 5.14 Experimental results of the relationship between the output power and the load resistance of TEH2 under the different random excitation levels: (a) the low-level excitation; (b) the medium-level excitation. (c) the high-level excitation.

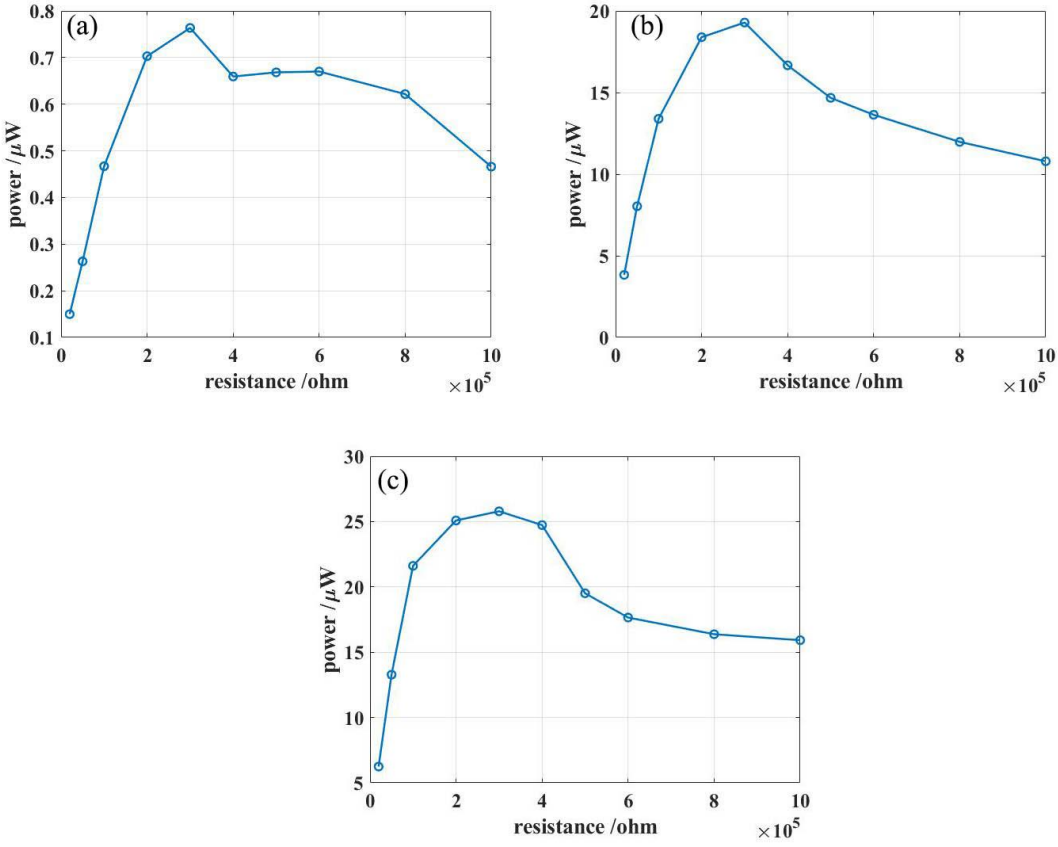

Figure 5.15 Experimental results of the relationship between the output power and the load resistance of TEH3 under the different random excitation levels: (a) the low-level excitation; (b) the medium-level excitation. (c) the high-level excitation.

5.1.4 Discussion of the Results

As shown in Table 5.1, under the low-level excitation or when the system operates in the intra-well oscillation mode, the simulation results and experimental results of the optimum resistance are at 360 KΩ and 300 KΩ, respectively. The optimum resistance value obtained from the simulation is slightly greater than that from the experiment. This can be explained as follow: since the oscillation of TEH1 is quite small under the low-level excitation, it can be seen as a linearized mono-stable system. And the optimum resistance

of the linear system is inversely proportional to its resonance frequency or the square root of the linear stiffness. Therefore, the discrepancy between the results of simulation and experiment may be attributed to the fact that the computed stiffness near the middle position is slightly lower than the actual value.

When TEH1 is subjected to the medium-level excitation, the system switches from the intra-well oscillation mode to the inter-well oscillation mode. The optimum resistance is increased to 560 KΩ. The main reason is that when the TEH1 oscillates between the two side wells, the low frequency components of the voltage response become more significant. It means that the system's internal impedance is larger when the system operates in the inter-well oscillation mode than that in the intra-well oscillation mode. When the excitation is increased to a high level, TEH1 maintains the high orbit inter-well oscillation. Therefore, the optimum resistance remains to be 560 KΩ.

As illustrated in Table 5.2, the increasing trend in the optimum resistance can be founded in the TEH2's simulation results (from 460 KΩ to 500 KΩ). Since under the medium-level excitation, TEH2 is on the verge of switching from the intra-well oscillation to the inter-well oscillation, it operates at the low orbit inter-well oscillation. Then the high-level excitation causes TEH2 to enter the high energy orbit inter-well oscillation. As a result, the optimum resistance is increased to 560 KΩ. However, the optimum resistances of TEH2 obtained from the experimental results vary little as the excitation level increases. Such a phenomenon can be attributed to the fact that the output voltage of the real piezoelectric energy harvester reaches its limit when the system operates in the high energy orbit. This issue has also been discussed in the previous chapter.

For TEH3, as illustrated in Table 5.3, the simulation results and experimental results of the optimum resistance are around 300 KΩ under the three excitation levels. Since THE3 operates in the intra-well oscillation mode under the three excitation levels, the optimum resistance value remains unchanged.

According to the simulation results and experimental results are shown in Table 5.1, Table 5.2 and Table 5.3, the maximum output power increases when the excitation level

increases. And the performance of the TEH can be greatly enhanced when the system operates in the inter-well oscillation. Since TEH1 has a larger separation distance between two side wells, it can generate more power among the three TEHs

Table 5.1 Optimum resistances and maximum output powers of TEH1 obtained by the simulation and experiment.

Method	**Low-level**		**Medium-level**		**High-level**	
	R_{opt} (KΩ)	P_{max} (μW)	R_{opt} (KΩ)	P_{max} (μW)	R_{opt} (KΩ)	P_{max} (μW)
Simulation	360	1.915	560	135.9	560	305.9
Experiment	300	20.25	—	—	—	—

Table 5.2 Optimum resistances and maximum output powers of TEH2 obtained by the simulation and experiment.

Method	**Low-level**		**Medium-level**		**High-level**	
	R_{opt} (KΩ)	P_{max} (μW)	R_{opt} (KΩ)	P_{max} (μW)	R_{opt} (KΩ)	P_{max} (μW)
Simulation	460	1.005	500	90	560	128
Experiment	400	1.652	400	102.4	400	148

Table 5.3 Optimum resistances and maximum output powers of TEH3 obtained by the simulation and experiment.

Method	**Low-level**		**Medium-level**		**High-level**	
	R_{opt} (KΩ)	P_{max} (μW)	R_{opt} (KΩ)	P_{max} (μW)	R_{opt} (KΩ)	P_{max} (μW)
Simulation	310	0.25	310	7.119	310	11.52
Experiment	300	0.7635	300	19.29	300	25.79

5.2 The Output Power verse the Excitation Level of the TEHs

This section focuses on the relationship between the output power and the excitation level for the three chosen TEHs. For this purpose, the load resistance is kept to be 1000 KΩ and the level of the colored noise excitation is varied.

5.2.1 Numerical Simulation

The random excitation signals used in the simulation are obtained from the experiment test by measuring the base displacement. The excitation level is measured by the integrals of PSD of the base acceleration and the following values are used in the simulation: S = 0.205 g, 0.487 g, 0.639 g, 0.822 g, 0.959 g, 1.153 g, 1.391 g, and 1.569 g. Eq. (4.1) and Eq. (4.2) are solved for the period of T=60 s with zero initial conditions using the MATLAB ODE45 solver. Based on the RMS values of the voltage response shown in Figure 5.16 (a), the output powers under the different excitation levels are obtained and shown in Figure 5.16 (b). The points A1, B1 and C and those on their left correspond to the excitation levels at which the systems operate in the intra-well oscillation. The points A2 and B2 correspond to the excitation levels at which the systems switch to the inter-well oscillation. The time responses and phase portraits of A1 and A2 are shown in Figure 5.17 (a) and (b) while the

time responses and phase portraits of B1 and B2 are demonstrated in Figure 5.18 (a) and (b), and the time response and phase portrait of C are shown in Figure 5.19.

As illustrated in Figure 5.16 (b), TEH1 is the most efficient in energy harvesting for different excitation levels, and it is much easier to enter the inter-well mode, in this case, under S=0.959 g. while TEH2 enters into the inter-well oscillation at S=1.391 g, and in the results of the vibration isolation character of THE3, it would keep operating in the inter-well oscillation mode, even when the excitation level is high.

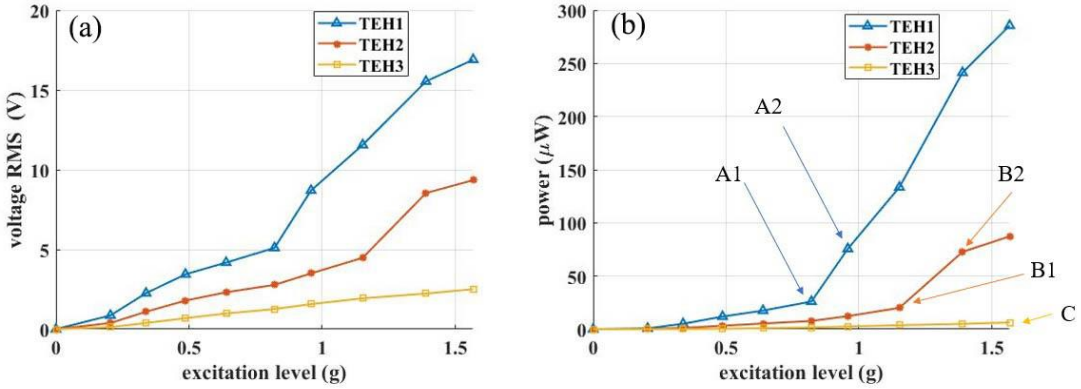

Figure 5.16 The simulation results of the three TEHs: (a) the voltage responses; (b) the output powers.

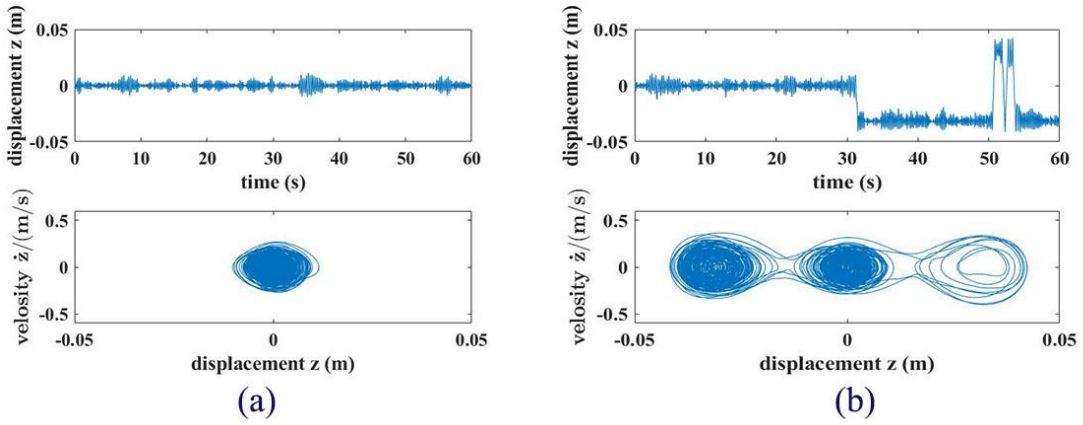

Figure 5.17 The simulation results of the time response (upper plot) and phase portrait (lower plot) of TEH1 under the specific level of the random excitation: (a) under the A1 excitation level; (b) under the A2 excitation level.

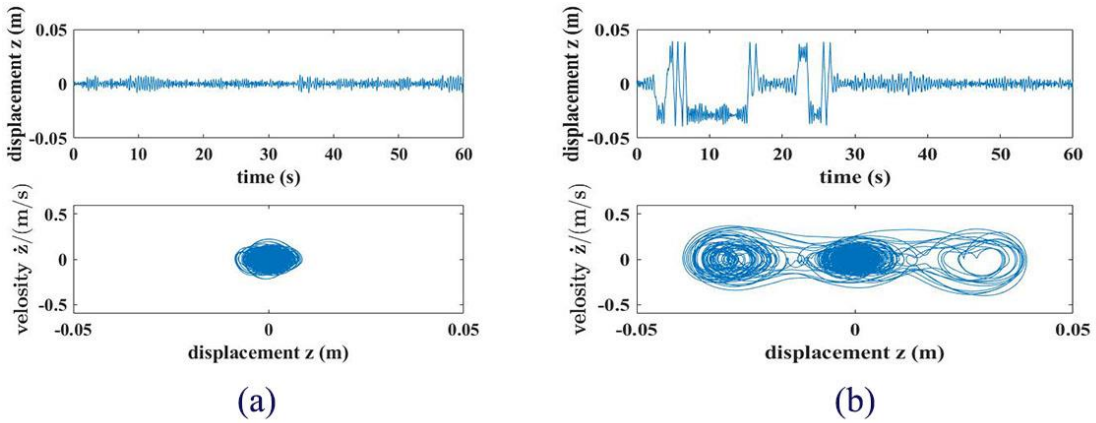

Figure 5.18 The simulation results of the time response (upper plot) and phase portrait (lower plot) of TEH2 under the specific level of the random excitation: (a) under the B1 excitation level; (b) under the B2 excitation level.

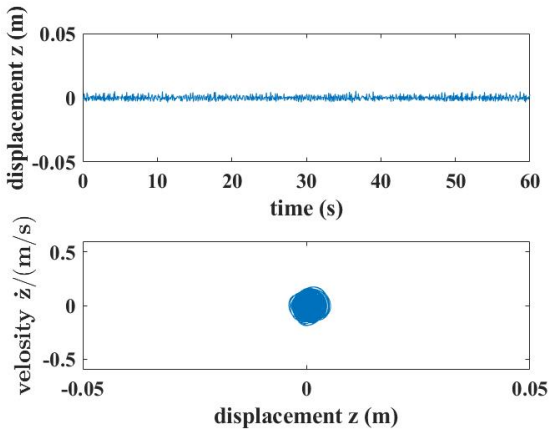

Figure 5.19 The simulation results of the time response (upper plot) and phase portrait (lower plot) of TEH3 under the C level of the random excitation.

5.2.2 Experimental Validation

In this section, The experimental validations of voltage responses and power outputs for TEHs under different excitation levels are conducted. The experimental results are shown in Figure 5.20. Since the experimental validation for TEH1 under the excitation level higher than 0.822 g is not attempted, the simulation result (blue dash line) represents the rest of the experimental results. Points A and B indicate that TEH1, and TEH2 switch from the intra-well oscillation mode to the inter-well oscillation mode, respectively. The time responses and phase portrait plots are shown in Figure 5.21 (a), and (b), respectively. Point C indicates that TEH3 operates in the intra-well oscillation at S=1.569 g. Its time responses and phase portrait plot are shown in Figure 5.21 (c).

For TEH1 and TEH2, the systems switch to the inter-well oscillation mode at S=0.822 g and 0.959 g, respectively. The values are slightly lower than the results obtained by the simulation, but the overall trend agrees with the simulation. And the same conclusions can be made: THE1 is the most efficient and easiest to transfer to the inter-well oscillation mode among the three systems.

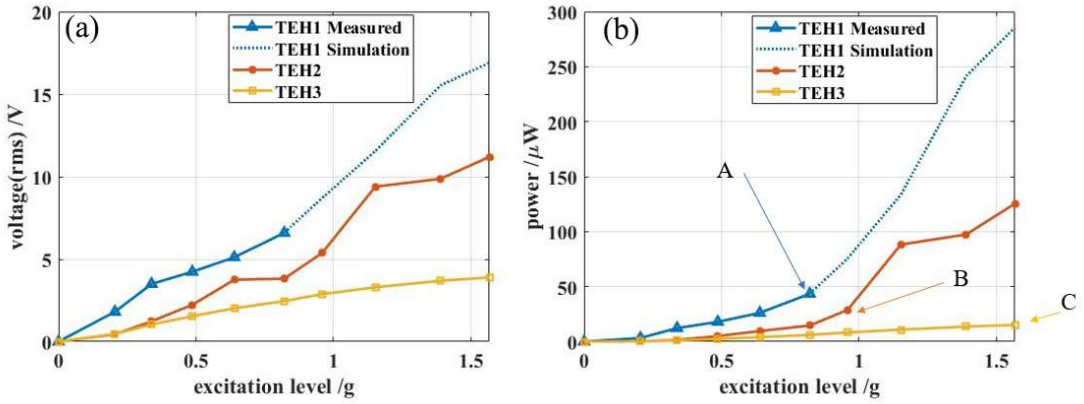

Figure 5.20 The experimental results of the three TEHs: (a) the voltage responses; (b) the power outputs.

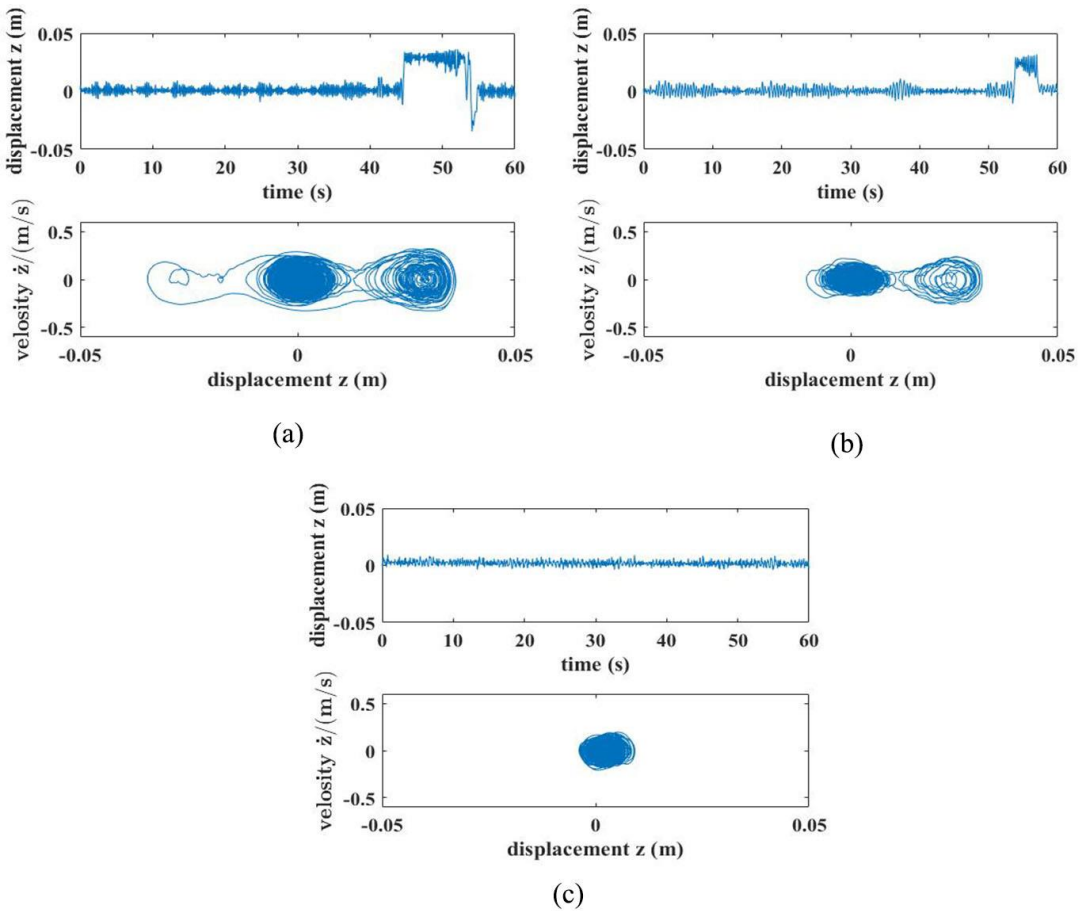

Figure 5.21 The experimental results of the time response (upper plot) and phase portrait (lower plot) of three systems under the specific level of the random excitation: (a) TEH1 under the A excitation level; (b) TEH2 under the B excitation level; (c) TEH3 under the C excitation level.

5.3 Conclusions

In this chapter, the three different TEHs has been investigated. Their optimum resistances have been determined and the comparison of their power output performances has also been conducted. The results show that the frequency analysis method cannot be used to determine the optimum resistance when the THE is engaged in the high orbit inter-well oscillation. Instead, the numerical simulation is employed. As the simulation results show, the optimum resistance increases when the THE enters into the inter-well motion.

Since the real system has a limited voltage output when it operates in the high energy orbit, this trend is not obvious in the experimental results. It has been proved that the optimum resistances are: 300 KΩ for TEH1; 400 KΩ for THE2; 300 KΩ for TEH3. By comparing the output performance of the three TEHs, it can be concluded that TEH1 is much easier to enter the inter-well oscillation under a low level of excitation, and it can generate more energy when the excitation level is high.

Chapter 6 Conclusions

In this study, a tunable multi-stable cantilevered piezoelectric energy harvester is developed. The apparatus consists of one large magnet that can be moved along a slot on the base and an assembly of three smaller magnets that is attached to the free end of a cantilever beam. By adjusting the configurations of the four magnets, the apparatus can exhibit the mono-stable, bi-stable and tri-stable behaviors, respectively. The biggest advantage of the developed apparatus is that it has a compact structure compared to the existing similar devices.

In Chapter 2, a full description of the proposed apparatus is presented. An analytical model for the restoring force due to the magnetic interaction is developed by using the magnetic dipole approach. After that, the numerical simulation is conducted to show how the stability states can be altered. Then, experimental validation is carried out. Finally, the genetic algorithm is used to optimize the analytical model based on the measured restoring forces. As a result, the optimized model is much more accurate than the original one. Based on the optimized model, the relationship between the stability states and the tuning parameters d and h is obtained from a great number of simulation tests. Accordingly, the stable state region has been generated.

In Chapter 3, the electromechanical model of the cantilevered piezoelectric energy harvester is developed. Then the model is approximated as a linear energy harvester (LEH). The optimum resistances of the LEH under harmonic excitation and colored noise excitation are investigated, respectively. Through the numerical simulation and experimental validation, the following conclusions can be derived. The optimum resistance value will decrease as the excitation frequency increases. For the colored noise excitation, the value of the optimum resistance depends on the resonance frequency of the system, which indicates that the analytical result based on the harmonic excitation still applies to the situation of the colored noise excitation. Besides, the maximum output power increases when the acceleration level of excitation increases.

In Chapter 4, the optimum resistances for the three different types of bi-stable energy harvester (BEH) named BEH1, BEH2, and BEH3 are investigated. And the comparison of their power output performances is also conducted. The results show that the frequency analysis method can be used to determine the optimum resistance for the BEHs. As the calculation results and the simulation results show, the optimum resistance will increase when the BEH enters the inter-well motion. Since the real system has a limited voltage output when it operates in high energy orbit, the increasing trend is not obvious in the experimental results. However, it still verifies that the ranges of the optimum resistance are: 300-400 KΩ for BEH1; 400-500 KΩ for BEH2; 500-600 KΩ for BEH3. By comparing the output performance of the three BEHs, it can be concluded that BEH 2 is much easier to enter the inter-well oscillation under a low level of excitation, and BEH 1 can generate more energy when the excitation level is high.

In Chapter 5, the three different types of tri-stable energy harvester (THE) named TEH1, TEH2, and TEH3 are considered. Their optimum resistances are determined, and a comparison of their power output performances is also conducted. The results show that the frequency analysis method cannot be used to determine the optimum resistance when the TEH is engaged in the high orbit inter-well oscillation. Instead, the numerical simulation is employed. As the simulation results show, the optimum resistance increases when the TEH enters into the inter-well motion. Since the real system has a limited voltage output when it operates in the high energy orbit, this trend is not obvious in the experimental results. The results reveal that the optimum resistances are: 300 KΩ for TEH1; 400 KΩ for THE2; 300 KΩ for TEH3. By comparing the output performances of the three TEHs, it can be concluded that TEH1 is much easier to enter the inter-well oscillation under a low level of excitation, and it can generate more energy when the excitation level is high.

Future research could be focused on the following aspects. The effect of the voltage limit phenomenon in electromechanical modelling should be investigated. For example, the electromechanical coupling coefficient θ can be represented by a function of the relative displacement. When the relative displacement exceeds a certain level, θ is

reduced. Besides, the biggest problem of the proposed apparatus is that the piezoelectric transducer cannot withstand large deformation. The most efficient energy harvester or TEH1 would be damaged when it operates in the inter-well oscillation mode under high level excitation. To overcome such a problem, the future work could concentrate on building a stiffer piezoelectric beam that can work under a large excitation. It could be accomplished by attaching a smaller size piezoelectric transducer to a stainless-steel substrate. Furthermore, the vibration isolation character of TEH3 is worth to explore. A passive vibration isolator could be developed based on TEH3's configuration.

Reference

[1] H. Landaluce, L. Arjona, A. Perallos, F. Falcone, I. Angulo, and F. Muralter, "A Review of IoT Sensing Applications and Challenges Using RFID and Wireless Sensor Networks," *Sensors (Basel),* vol. 20, no. 9, Apr 28 2020, doi: 10.3390/s20092495.

[2] H. G. Lee and N. Chang, "Powering the IoT: Storage-less and converter-less energy harvesting," in *The 20th Asia and South Pacific Design Automation Conference*, 19-22 Jan. 2015 2015, pp. 124-129, doi: 10.1109/ASPDAC.2015.7058992.

[3] K. K. Win, X. Wu, S. Dasgupta, W. J. Wen, R. Kumar, and S. K. Panda, "Efficient solar energy harvester for wireless sensor nodes," in *2010 IEEE International Conference on Communication Systems*, 17-19 Nov. 2010 2010, pp. 289-294, doi: 10.1109/ICCS.2010.5686355.

[4] M. Vasiliev and K. Alameh, "Recent developments in solar energy-harvesting technologies for building integration and distributed energy generation," *Energies,* vol. 12, no. 6, p. 1080, 2019.

[5] A. L. Cottrill, A. T. Liu, Y. Kunai, V. B. Koman, A. Kaplan, S. G. Mahajan, P. Liu, A. R. Toland, and M. S. Strano, "Ultra-high thermal effusivity materials for resonant ambient thermal energy harvesting," *Nature communications,* vol. 9, no. 1, pp. 1-11, 2018.

[6] S. Wu, T. Li , Z. Tong, J. Chao, T. Zhai, J. Xu, T. Yan , M. Wu , Z. Xu, and H. Bao, "High-Performance Thermally Conductive Phase Change Composites by Large-Size Oriented Graphite Sheets for Scalable Thermal Energy Harvesting," *Advanced Materials,* vol. 31, no. 49, p. 1905099, 2019.

[7] C. Rivera, J. J. Pantoja, and F. Roman, "Antenna array assessment for RF energy harvesting," in *2017 IEEE International Symposium on Antennas and Propagation & USNC/URSI National Radio Science Meeting*, 2017: IEEE, pp. 1097-1098.

[8] J. Milanezi, R. S. Ferreira, J. P. C. da Costa, G. del Galdo, R. K. Miranda, W. Felber, and E. P. de Freitas, "Radiofrequency energy harvesting system based on a rectenna array in urban environments," in *2017 International Conference on Signals and Systems (ICSigSys)*, 2017: IEEE, pp. 151-157.

[9] B. Maamer, A. Boughamoura, A. M. R. Fath El-Bab, L. A. Francis, and F. Tounsi, "A review on design improvements and techniques for mechanical energy harvesting using piezoelectric and electromagnetic schemes," *Energy Conversion and Management,* vol. 199, 2019, doi: 10.1016/j.enconman.2019.111973.

[10] B. Andò, S. Baglio, A. R. Bulsara, V. Marletta, and A. Pistorio, "Investigation of a Nonlinear Energy Harvester," *IEEE Transactions on Instrumentation and Measurement,* vol. 66, no. 5, pp. 1067-1075, 2017, doi:

10.1109/TIM.2017.2663178.

[11] S. D. Jewkes J., Stillerman R. , *Self-Winding Wrist-Watch. In: The Sources of Invention*. London: Palgrave Macmillan, 1969.

[12] S.-D. Kwon, J. Park, and K. Law, "Electromagnetic energy harvester with repulsively stacked multilayer magnets for low frequency vibrations," *Smart materials and structures,* vol. 22, no. 5, p. 055007, 2013.

[13] C. B. Williams and R. B. Yates, "Analysis of a micro-electric generator for microsystems," *Sensors and Actuators A: Physical,* vol. 52, no. 1, pp. 8-11, 1996/03/01/ 1996, doi: https://doi.org/10.1016/0924-4247(96)80118-X.

[14] Y. Pan, T. Lin, F. Qian, C. Liu, J. Yu, J. Zuo, and L. Zuo, "Modeling and field-test of a compact electromagnetic energy harvester for railroad transportation," *Applied Energy,* vol. 247, pp. 309-321, 2019.

[15] A. Munaz, B.-C. Lee, and G.-S. Chung, "A study of an electromagnetic energy harvester using multi-pole magnet," *Sensors and Actuators A: Physical,* vol. 201, pp. 134-140, 2013.

[16] M. A. Halim, H. Cho, and J. Y. Park, "Design and experiment of a human-limb driven, frequency up-converted electromagnetic energy harvester," *Energy Conversion and Management,* vol. 106, pp. 393-404, 2015.

[17] Y. Zhang, T. Wang, A. Luo, Y. Hu, X. Li, and F. Wang, "Micro electrostatic energy harvester with both broad bandwidth and high normalized power density," *Applied energy,* vol. 212, pp. 362-371, 2018.

[18] H. Koga, H. Mitsuya, H. Honma, H. Fujita, H. Toshiyoshi, and G. Hashiguchi, "Development of a cantilever-type electrostatic energy harvester and its charging characteristics on a highway viaduct," *Micromachines,* vol. 8, no. 10, p. 293, 2017.

[19] D. Nguyen, E. Halvorsen, G. Jensen, and A. Vogl, "Fabrication and characterization of a wideband MEMS energy harvester utilizing nonlinear springs," *Journal of Micromechanics and Microengineering,* vol. 20, no. 12, p. 125009, 2010.

[20] D.-H. Choi, C.-H. Han, H.-D. Kim, and J.-B. Yoon, "Liquid-based electrostatic energy harvester with high sensitivity to human physical motion," *Smart materials and structures,* vol. 20, no. 12, p. 125012, 2011.

[21] C. H. Nguyen, D. S. Nguyen, and E. Halvorsen, "Experimental validation of damping model for a MEMS bistable electrostatic energy harvester," in *Journal of Physics: Conference Series*, 2014, vol. 557, no. 1: IOP Publishing, p. 012114.

[22] Z. Xiao, T. q. Yang, Y. Dong, and X. c. Wang, "Energy harvester array using piezoelectric circular diaphragm for broadband vibration," *Applied Physics Letters,* vol. 104, no. 22, p. 223904, 2014.

[23] X.-r. Chen, T.-q. Yang, W. Wang, and X. Yao, "Vibration energy harvesting with a clamped piezoelectric circular diaphragm," *Ceramics International,* vol. 38, pp. S271-S274, 2012.

[24] J. Palosaari, M. Leinonen, J. Hannu, J. Juuti, and H. Jantunen, "Energy harvesting with a cymbal type piezoelectric transducer from low frequency compression," *Journal of electroceramics,* vol. 28, no. 4, pp. 214-219, 2012.

[25] R. Esmaeeli, H. Aliniagerdroudbari, S. R. Hashemi, M. Alhadri, W. Zakri, C. Batur, and S. Farhad, "Design, modeling, and analysis of a high performance piezoelectric energy harvester for intelligent tires," *International Journal of Energy Research,* vol. 43, no. 10, pp. 5199-5212, 2019.

[26] S. Mishra, L. Unnikrishnan, S. K. Nayak, and S. Mohanty, "Advances in Piezoelectric Polymer Composites for Energy Harvesting Applications: A Systematic Review," *Macromolecular Materials and Engineering,* vol. 304, no. 1, 2019, doi: 10.1002/mame.201800463.

[27] A. Keshmiri, X. Deng, and N. Wu, "New energy harvester with embedded piezoelectric stacks," *Composites Part B: Engineering,* vol. 163, pp. 303-313, 2019.

[28] B. Yang, C. Lee, W. L. Kee, and S.-P. Lim, "Hybrid energy harvester based on piezoelectric and electromagnetic mechanisms," *Journal of Micro/Nanolithography, MEMS, and MOEMS,* vol. 9, no. 2, p. 023002, 2010.

[29] P. Li, S. Gao, S. Niu, H. Liu, and H. Cai, "An analysis of the coupling effect for a hybrid piezoelectric and electromagnetic energy harvester," *Smart materials and structures,* vol. 23, no. 6, p. 065016, 2014.

[30] L.-m. Cao, Z.-x. Li, C. Guo, P.-p. Li, X.-q. Meng, and T.-m. Wang, "Design and test of the MEMS coupled piezoelectric–electromagnetic energy harvester," *International Journal of Precision Engineering and Manufacturing,* vol. 20, no. 4, pp. 673-686, 2019.

[31] Y. Eun, D.-S. Kwon, M.-O. Kim, I. Yoo, J. Sim, H.-J. Ko, K.-H. Cho, and J. Kim, "A flexible hybrid strain energy harvester using piezoelectric and electrostatic conversion," *Smart Materials and Structures,* vol. 23, no. 4, p. 045040, 2014.

[32] S. Lajimi, F. Mousavi, and M. Friswell, "Design, analysis, and feedback control of a nonlinear micro-piezoelectric–electrostatic energy harvester," *NONLINEAR DYNAMICS,* 2020.

[33] N. E. DuToit and B. L. Wardle, "Experimental verification of models for microfabricated piezoelectric vibration energy harvesters," *AIAA journal,* vol. 45, no. 5, pp. 1126-1137, 2007.

[34] H. A. Sodano, G. Park, and D. Inman, "Estimation of electric charge output for piezoelectric energy harvesting," *Strain,* vol. 40, no. 2, pp. 49-58, 2004.

[35] Y. Jeon, R. Sood, J.-H. Jeong, and S.-G. Kim, "MEMS power generator with transverse mode thin film PZT," *Sensors and Actuators A: Physical,* vol. 122, no. 1, pp. 16-22, 2005.

[36] A. Erturk and D. J. Inman, "A Distributed Parameter Electromechanical Model for Cantilevered Piezoelectric Energy Harvesters," *Journal of Vibration and Acoustics,*

vol. 130, no. 4, 2008, doi: 10.1115/1.2890402.

[37] A. Erturk and D. J. Inman, "On Mechanical Modeling of Cantilevered Piezoelectric Vibration Energy Harvesters," *Journal of Intelligent Material Systems and Structures,* vol. 19, no. 11, pp. 1311-1325, 2008, doi: 10.1177/1045389x07085639.

[38] C. V. Karadag and N. Topaloglu, "A self-sufficient and frequency tunable piezoelectric vibration energy harvester," *Journal of Vibration and Acoustics,* vol. 139, no. 1, 2017.

[39] S.-J. Jang, I.-H. Kim, H.-J. Jung, and Y.-P. Lee, "A tunable rotational energy harvester for low frequency vibration," *Applied Physics Letters,* vol. 99, no. 13, p. 134102, 2011.

[40] E. S. Leland and P. K. Wright, "Resonance tuning of piezoelectric vibration energy scavenging generators using compressive axial preload," *Smart Materials and Structures,* vol. 15, no. 5, pp. 1413-1420, 2006/09/08 2006, doi: 10.1088/0964-1726/15/5/030.

[41] M. Ferrari, D. Alghisi, M. Baù, and V. Ferrari, "Nonlinear Multi-Frequency Converter Array for Vibration Energy Harvesting in Autonomous Sensors," *Procedia Engineering,* vol. 47, pp. 410-413, 2012, doi: 10.1016/j.proeng.2012.09.171.

[42] D. Zhao, M. Gan, C. Zhang, J. Wei, S. Liu, and T. Wang, "Analysis of broadband characteristics of two degree of freedom bistable piezoelectric energy harvester," *Materials Research Express,* vol. 5, no. 8, p. 085704, 2018.

[43] J. Twiefel and H. Westermann, "Survey on broadband techniques for vibration energy harvesting," *Journal of Intelligent Material Systems and Structures,* vol. 24, no. 11, pp. 1291-1302, 2013, doi: 10.1177/1045389x13476149.

[44] Z. Yang, S. Zhou, J. Zu, and D. Inman, "High-Performance Piezoelectric Energy Harvesters and Their Applications," *Joule,* vol. 2, no. 4, pp. 642-697, 2018, doi: 10.1016/j.joule.2018.03.011.

[45] S. P. Pellegrini, N. Tolou, M. Schenk, and J. L. Herder, "Bistable vibration energy harvesters: A review," *Journal of Intelligent Material Systems and Structures,* vol. 24, no. 11, pp. 1303-1312, 2012, doi: 10.1177/1045389x12444940.

[46] S. C. Stanton, C. C. McGehee, and B. P. Mann, "Reversible hysteresis for broadband magnetopiezoelastic energy harvesting," *Applied Physics Letters,* vol. 95, no. 17, 2009, doi: 10.1063/1.3253710.

[47] K. Fan, Q. Tan, Y. Zhang, S. Liu, M. Cai, and Y. Zhu, "A monostable piezoelectric energy harvester for broadband low-level excitations," *Applied Physics Letters,* vol. 112, no. 12, 2018, doi: 10.1063/1.5022599.

[48] S. C. Stanton, C. C. McGehee, and B. P. Mann, "Reversible hysteresis for broadband magnetopiezoelastic energy harvesting," *Applied Physics Letters,* vol. 95, no. 17, p. 174103, 2009.

[49] F. Cottone, H. Vocca, and L. Gammaitoni, "Nonlinear energy harvesting," *Phys Rev Lett,* vol. 102, no. 8, p. 080601, Feb 27 2009, doi: 10.1103/PhysRevLett.102.080601.

[50] L. Tang, Y. Yang, and C.-K. Soh, "Improving functionality of vibration energy harvesters using magnets," *Journal of Intelligent Material Systems and Structures,* vol. 23, no. 13, pp. 1433-1449, 2012, doi: 10.1177/1045389x12443016.

[51] M. F. Daqaq, "Transduction of a bistable inductive generator driven by white and exponentially correlated Gaussian noise," *Journal of Sound and Vibration,* vol. 330, no. 11, pp. 2554-2564, 2011, doi: 10.1016/j.jsv.2010.12.005.

[52] J.-T. Lin and B. Alphenaar, "Enhancement of Energy Harvested from a Random Vibration Source by Magnetic Coupling of a Piezoelectric Cantilever," *Journal of Intelligent Material Systems and Structures,* vol. 21, no. 13, pp. 1337-1341, 2009, doi: 10.1177/1045389x09355662.

[53] S. Zhao and A. Erturk, "On the stochastic excitation of monostable and bistable electroelastic power generators: Relative advantages and tradeoffs in a physical system," *Applied Physics Letters,* vol. 102, no. 10, p. 103902, 2013, doi: 10.1063/1.4795296.

[54] J. Jung, P. Kim, J.-I. Lee, and J. Seok, "Nonlinear dynamic and energetic characteristics of piezoelectric energy harvester with two rotatable external magnets," *International Journal of Mechanical Sciences,* vol. 92, pp. 206-222, 2015, doi: 10.1016/j.ijmecsci.2014.12.015.

[55] S. Zhou, J. Cao, A. Erturk, and J. Lin, "Enhanced broadband piezoelectric energy harvesting using rotatable magnets," *Applied Physics Letters,* vol. 102, no. 17, p. 173901, 2013, doi: 10.1063/1.4803445.

[56] J. Cao, S. Zhou, W. Wang, and J. Lin, "Influence of potential well depth on nonlinear tristable energy harvesting," *Applied Physics Letters,* vol. 106, no. 17, p. 173903, 2015, doi: 10.1063/1.4919532.

[57] L. Haitao, Q. Weiyang, L. Chunbo, D. Wangzheng, and Z. Zhiyong, "Dynamics and coherence resonance of tri-stable energy harvesting system," *Smart Materials and Structures,* vol. 25, no. 1, p. 015001, 2016, doi: 10.1088/0964-1726/25/1/015001.

[58] Y. Leng, D. Tan, J. Liu, Y. Zhang, and S. Fan, "Magnetic force analysis and performance of a tri-stable piezoelectric energy harvester under random excitation," *Journal of Sound and Vibration,* vol. 406, pp. 146-160, 2017, doi: 10.1016/j.jsv.2017.06.020.

[59] S. Roundy, P. K. Wright, and J. Rabaey, "A study of low level vibrations as a power source for wireless sensor nodes," *Computer communications,* vol. 26, no. 11, pp. 1131-1144, 2003.

[60] N. E. Dutoit, B. L. Wardle, and S.-G. Kim, "Design considerations for MEMS-scale piezoelectric mechanical vibration energy harvesters," *Integrated ferroelectrics,*

vol. 71, no. 1, pp. 121-160, 2005.

[61] H.-y. Wang, X.-b. Shan, and T. Xie, "An energy harvester combining a piezoelectric cantilever and a single degree of freedom elastic system," *Journal of Zhejiang University SCIENCE A,* vol. 13, no. 7, pp. 526-537, 2012.

[62] S. Rafique and P. Bonello, "Experimental validation of a distributed parameter piezoelectric bimorph cantilever energy harvester," *Smart materials and structures,* vol. 19, no. 9, p. 094008, 2010.

[63] A. Aladwani, O. Aldraihem, and A. Baz, "A distributed parameter cantilevered piezoelectric energy harvester with a dynamic magnifier," *Mechanics of Advanced Materials and Structures,* vol. 21, no. 7, pp. 566-578, 2014.

[64] B. Wang, Z. Li, and Z. Yang, "A distributed-parameter electromechanical coupling model for a piezoelectric energy harvester with variable curvature," *Smart Materials and Structures,* vol. 29, no. 11, p. 115015, 2020.

[65] A. Erturk and D. J. Inman, *Piezoelectric energy harvesting*. John Wiley & Sons, 2011.

[66] L. Zhao, L. Tang, and Y. Yang, "Comparison of modeling methods and parametric study for a piezoelectric wind energy harvester," *Smart Materials and Structures,* vol. 22, no. 12, 2013, doi: 10.1088/0964-1726/22/12/125003.

[67] K. W. Yung, P. B. Landecker, and D. D. Villani, "An analytic solution for the force between two magnetic dipoles," *Physical Separation in Science and Engineering,* vol. 9, no. 1, pp. 39-52, 1998.

[68] D. Tan, Y. G. Leng, and Y. J. Gao, "Magnetic force of piezoelectric cantilever energy harvesters with external magnetic field," *The European Physical Journal Special Topics,* vol. 224, no. 14-15, pp. 2839-2853, 2015, doi: 10.1140/epjst/e2015-02592-6.

[69] S. Zhou, J. Cao, D. J. Inman, J. Lin, S. Liu, and Z. Wang, "Broadband tristable energy harvester: Modeling and experiment verification," *Applied Energy,* vol. 133, pp. 33-39, 2014, doi: 10.1016/j.apenergy.2014.07.077.

[70] J.-T. Lin, B. Lee, and B. Alphenaar, "The magnetic coupling of a piezoelectric cantilever for enhanced energy harvesting efficiency," *Smart Materials and Structures,* vol. 19, no. 4, p. 045012, 2010, doi: 10.1088/0964-1726/19/4/045012.

[71] K. Worden, "Data processing and experiment design for the restoring force surface method, part II: choice of excitation signal," *Mechanical Systems and Signal Processing,* vol. 4, no. 4, pp. 321-344, 1990.

[72] E. Fukada, "Piezoelectricity as a fundamental property of wood," *Wood Science and Technology,* vol. 2, no. 4, pp. 299-307, 1968/12/01 1968, doi: 10.1007/BF00350276.

[73] S. Priya, H.-C. Song, Y. Zhou, R. Varghese, A. Chopra, S.-G. Kim, I. Kanno, L. Wu, D. S. Ha, J. Ryu, and R. G. Polcawich, "A review on piezoelectric energy harvesting: materials, methods, and circuits," *Energy Harvesting and Systems,* vol. 4, no. 1, pp.

3-39, 2019.

[74] H. A. Sodano, G. Park, and D. Inman, "Estimation of electric charge output for piezoelectric energy harvesting," *Strain,* vol. 40, no. 2, pp. 49-58, 2004.

[75] A. Erturk and D. J. Inman, *Piezoelectric energy harvesting*. John Wiley & Sons, 2011.

[76] "IEEE Standard on Piezoelectricity," *ANSI/IEEE Std 176-1987,* pp. 0_1-, 1988 1988, doi: 10.1109/IEEESTD.1988.79638.

[77] N. W. Hagood, W. H. Chung, and A. Von Flotow, "Modelling of Piezoelectric Actuator Dynamics for Active Structural Control," *Journal of Intelligent Material Systems and Structures,* vol. 1, no. 3, pp. 327-354, 2016, doi: 10.1177/1045389x9000100305.

[78] D. J. Inman, *Engineering vibration*. Prentice-Hall Inc, 2001.

[79] K. H. Mak, S. McWilliam, A. A. Popov, and C. H. J. Fox, "Performance of a cantilever piezoelectric energy harvester impacting a bump stop," *Journal of Sound and Vibration,* vol. 330, no. 25, pp. 6184-6202, 2011, doi: 10.1016/j.jsv.2011.07.008.

[80] W. Wang, J. Cao, C. R. Bowen, S. Zhou, and J. Lin, "Optimum resistance analysis and experimental verification of nonlinear piezoelectric energy harvesting from human motions," *Energy,* vol. 118, pp. 221-230, 2017, doi: 10.1016/j.energy.2016.12.035.

[81] J. Cooper, "Extending the logarithmic decrement method to analyse two degree of freedom transient responses," *Mechanical Systems and Signal Processing,* vol. 10, no. 4, pp. 497-500, 1996/07/01/ 1996, doi: https://doi.org/10.1006/mssp.1996.0034

[82] V. T. Rathod, "A Review of Electric Impedance Matching Techniques for Piezoelectric Sensors, Actuators and Transducers," *Electronics,* vol. 8, no. 2, p. 169, 2019, doi: 10.3390/electronics8020169.

[83] P. Li, S. Gao, H. Cai, and Y. Cui, "Design, fabrication and performances of MEMS piezoelectric energy harvester," *International Journal of Applied Electromagnetics and Mechanics,* vol. 47, no. 1, pp. 125-139, 2015.

[84] M. S. Nguyen, Y.-J. Yoon, O. Kwon, and P. Kim, "Lowering the potential barrier of a bistable energy harvester with mechanically rectified motion of an auxiliary magnet oscillator," *Applied Physics Letters,* vol. 111, no. 25, p. 253905, 2017, doi: 10.1063/1.4994111.

[85] N. Zhou and K. Liu, "A tunable high-static–low-dynamic stiffness vibration isolator," *Journal of Sound and Vibration,* vol. 329, no. 9, pp. 1254-1273, 2010, doi: 10.1016/j.jsv.2009.11.001.